NASA TECHNICAL
REPORT

THEORETICAL AND EXPERIMENTAL STUDY OF THE INTERACTION OF FREE-SURFACE WAVES ON LIQUID METALS WITH TRANSVERSE MAGNETIC FIELDS (ONE-DIMENSIONAL UNSTEADY WAVES)

by Vernon J. Rossow

Ames Research Center
Moffett Field, Calif.

THEORETICAL AND EXPERIMENTAL STUDY OF THE INTERACTION

OF FREE-SURFACE WAVES ON LIQUID METALS

WITH TRANSVERSE MAGNETIC FIELDS

(ONE-DIMENSIONAL UNSTEADY WAVES)

By Vernon J. Rossow

Ames Research Center
Moffett Field, Calif.

NATIONAL AERONAUTICS AND SPACE ADMINISTRATION

TECHNICAL REPORT R-161

THEORETICAL AND EXPERIMENTAL STUDY OF THE INTERACTION

OF FREE-SURFACE WAVES ON LIQUID METALS

WITH TRANSVERSE MAGNETIC FIELDS

(ONE-DIMENSIONAL UNSTEADY WAVES)

By Vernon J. Rossow

SUMMARY

The free-surface analogy that exists between pressure waves in an ionized gas and waves on the surface of a liquid metal is studied experimentally and theoretically by considering in detail the interaction of one-dimensional waves in a channel with a transverse magnetic field. Photographic sequences are presented of the surface shapes found experimentally with mercury and the eutectic alloy of sodium and potassium (NaK). These results are compared with the corresponding surface profiles predicted theoretically by the one-dimensional mathematical method of characteristics for unsteady flows. It is concluded that the analogy is a useful tool for studying certain aspects of magnetohydrodynamic flow fields. The tests carried out in the investigation also provide information on the interaction of one-dimensional waves with a transverse magnetic field.

INTRODUCTION

Difficulties associated with magnetogasdynamic experiments and analyses cause one to look for an analogy or simplification that will aid in understanding the various fluid motions that are observed. In the search for such a device, it may be noted that a decade or so ago the studies of ordinary gas-dynamic flow fields often made use of what is known as the free-surface analogy. This analogy is one wherein gravity waves on the surface of water of shallow depth represent pressure waves in the gas. A large number of investigations (refs. 1 - 11) were carried out to ascertain the applicability of the analogy and to study a particular flow phenomenon. Material found in the partial list of references cited (refs. 1 - 11) illustrates the amount of information that can be obtained and the ease with which a flow field can be diagnosed when the free-surface analogy is employed.

In recognition of the possible application to magnetofluid dynamics, several papers (refs. 12 - 16) have been written recently that extend the free-surface analogy to include that type of magnetogasdynamic phenomenon characterized by a low magnetic Reynolds number ($R_m \ll 1$). Noteworthy is a paper by Fraenkel

(ref. 12) in which he derives in a systematic fashion the differential equations for the surface wave motion with electric and magnetic fields and then analyzes several flow fields. Alpher (refs. 13 and 14) develops the equations he requires and also presents some experimental results obtained with mercury. A theoretical analysis is given by Lundquist (ref. 17), and somewhat later by Shirokov (ref. 18), for a second category of free-surface phenomena in which the liquid metal is a nearly perfect electrical conductor (i.e., $R_m = \infty$). At this limit, the waves propagate at the characteristic velocity $a_{\sigma=\infty} = \sqrt{(B^2/\rho\mu) + gh}$ rather than simply $\sqrt{gh}$.

Analogies that use liquid metals, but that are not of the free-surface variety, have been used in several other studies of magnetogasdynamic phenomena. Included are the results of a series of interesting and informative tests with sodium carried out by Colgate (refs. 19 and 20) in order to study the stability of nuclear fusion devices. Other experiments with liquid metals, references 21 - 29, illustrate the ingenious use of liquid metals to study various magnetohydrodynamic problems.

This paper presents a detailed and systematic study of the interaction of one-dimensional free-surface waves with transverse magnetic fields. The purpose of this investigation is to gain a basic understanding of these flow fields. Motivation arises from the need to obtain background information in order to interpret magnetogasdynamic test results. Details of the theories used and results achieved are given in the sections to follow, and consist of the five general subjects: (1) After the models to be considered are described, the relations to be used to solve the one-dimensional unsteady flow fields are developed from the equations that represent the motion of liquid metals in the free-surface, small-depth approximation. Theoretical results for an example of each of the models to be studied are then presented. (2) Equations are developed for idealized magnetogasdynamic models that are comparable to the free-surface configurations under consideration. A specific solution for each is then compared in order to gain an insight into the nature of the analogy between the two systems. (3) The influence of various boundary conditions on the electric field and current configurations is analyzed. (4) An analysis is made of the distortions brought about on the surface of the liquid metal by the changing magnetic field that results when a magnet is energized. (5) Photographic sequences are presented of the experimental liquid metal (Hg or NaK)[1] surface shapes. In companion figures, a comparison is made of some of these results with the theoretically predicted profiles.

FLOW MODELS AND RANGE OF VARIABLES TO BE STUDIED

To fulfill the objectives outlined in the previous section, the models chosen for consideration are kept as simple in concept as possible so that the number of flow variables are minimized and so that the waves are nearly

---

[1]The eutectic mixture of sodium (22 percent) and potassium (78 percent) is generally referred to as NaK. Properties of this liquid metal are given in reference 30. It is useful in these tests because it has a specific gravity of 0.86 and has an electrical conductivity three times that of mercury.

one-dimensional. The particular flow models, some anticipated results, and a brief description of the experimental model are discussed in the following paragraphs.

The first flow model to be considered is that of a one-dimensional compression wave impinging upon a magnetic field. The magnetic field is assumed to be sharply defined, so a uniform state exists on both sides of the wave until it approaches and passes into the magnetic field region. There, the fluid moving relative to the magnetic field experiences a damping force tending to retard its motion. Because of this body force, a portion of the wave is reflected from the magnetic field and a part passes through. The relative magnitudes of the reflected and transmitted waves depend on the magnetic field strength, B, electrical conductivity of the liquid metal, σ, and the inertia of the fluid in the wave. Figure 1 illustrates the physical model for producing this type of flow. The wave is initiated by suddenly, at some time t = 0, moving the piston to the right at some uniform speed u_p. Such a flow field can be considered as a simulation of the shock tube studies of one-dimensional ionizing shock waves interacting with magnetic fields (refs. 31 - 34).

A second flow situation to be studied is that of an expansion wave centered in the magnetic field. Since the magnetic field again exerts a damping force on the motion, it can be expected that the fluid will seep through the magnetic field much more slowly than a corresponding expansion wave in a channel with no magnetic field. The physical model is the same as shown in figure 1 except that the piston is initially at rest in the center of the magnetic field and then is suddenly withdrawn to the left. Such a model represents the breaking of a dam in hydraulics, or the bursting of a diaphragm in a shock tube. Flow problems of this type are usually referred to as a "centered expansion" because, at the start, all of the expansion waves are located or centered at the interface of the piston and liquid metal. As time progresses, the individual waves spread out or expand and thereby resolve the initial discontinuity into a smoothly curved surface that once again depends on the strength of the magnetic interaction. If the magnetic field strength were indefinitely strong, the initial discontinuity would not change as the piston is withdrawn.

A third type of flow to be considered is the interaction of a fluid at rest with a moving magnetic field. As the magnetic field moves past the liquid metal, a body force generated by the moving field acts like a leaky broom (or piston) that sweeps or pushes the liquid metal along the channel. Only for very strong interactions will the magnetic field sweep all of the fluid from the channel it has passed. The physical model for producing this type of flow is shown in figure 2.

The last type of flow to be studied is the motion imparted to the fluid by a changing magnetic field. The physical results of this type of flow are more complex and will be described in a later section. The physical apparatus is, however, shown schematically in figures 3(a) and (b).

In each of the foregoing flow situations the boundary conditions on the electric fields and currents must be such that the theoretical and experimental models are matched as closely as possible. Ideally, an external return circuit should be provided for each transverse electric-current filament so that the

direction of the body forces is along the channel axis. Metal wires required for these circuits would obstruct the view of the profile of the liquid metal surface, however. Therefore, an alternative scheme that approaches the ideal employs a copper plate on the bottom of the channel in contact with the liquid metal. Possible effects of various current paths are investigated in a section following the mathematical method of characteristics for one-dimensional unsteady fluid motion which has been developed for these flow models.

Each of these models will be studied theoretically and tested experimentally under a variety of conditions with both the liquid metals Hg and NaK. (Use of these two materials yields a wide range of the magnetic parameters.) Numerical values for some of the parameters involved in these tests are given approximately as (see appendix for definition of symbols)

$$R_m = \sigma \mu a_0 d \approx 0.03$$

$$R_e = \frac{\rho a_0 d}{\eta} \approx 1000 - 5000$$

$$P_m = \frac{\sigma B_0^2 d}{\rho a_0} \approx \begin{cases} 1.5 \text{ for mercury} \\ \text{,0 for NaK} \end{cases}$$

$$Ha = \sqrt{\frac{\sigma}{\eta}} B_0 d \approx 350$$

$$h_0 = \text{depth of fluid} \approx 1 \text{ cm or } 0.4 \text{ in.}$$

$$B_0 \approx 5000 \text{ gauss}$$

$$a_0 = \text{speed of free-surface wave} = \sqrt{gh_0}$$

$$\approx 30 \text{ cm/sec or } 1 \text{ ft/sec}$$

$$Fr = \text{Froude no.} = \frac{u}{\sqrt{gh_0}} \approx 0.2 \text{ to } 2.0$$

THEORETICAL ANALYSIS

In this section, equations are developed to predict the fluid motion of the one-dimensional flow fields discussed in the previous section. Since the analysis to follow is based on the free-surface wave theory, the approximations made for it apply here also. The idealizations discussed in references 1 to 11 may be summarized as follows:

1. Viscous and surface tension forces are negligible in comparison with inertia and pressure forces.

2. Density of liquid is a constant.

3. Pressure on free surface of liquid is a constant and bottom of container is flat.

4

4. Pressure distribution is hydrostatic; that is, vertical accelerations and velocities are small with respect to horizontal components.

5. Ratio of mean depth to wavelength must be small.

If the free-surface wave theory is to be extended to liquid metals in electric and magnet , fields, the following additional restrictions are imposed:

6. Properties (density, conductivity, etc.) are changed an insignificant amount by joule heating.

7. Current density is independent of fluid depth.

8. Fluid has uniform electrical properties throughout flow field.

9. Electric currents are horizontal only.

10. Induced electric field and electric current density vectors are alined.

11. Magnetic field has only a vertical component that is uniform throughout depth of the fluid.

12. Hall, displacement, etc., currents are negligible.

13. Magnetic Reynolds number = $\sigma \mu a_o d \ll 1$; that is, induced or secondary magnetic fields are small in comparison with imposed field.

Assumptions 1, 4, and 5 are violated at the front of a strong wave (or bore) because the wave front is quite short in comparison with the depth of the fluid. In the idealized case, the wave front is a discontinuous step from one level to another. In practice, however, viscosity and surface tension forces round off the corners to form a wave of finite but small length. Since discussions of the effect of the shape of the wave front and the role played by viscosity and surface tension are presented elsewhere (see, e.g., refs. 1 through 11), a detailed account of the difficulties associated with these wave fronts will not be given here. It is simply noted that the analogy and the equations for the free surface are not valid in the immediate vicinity of such a wave front. Flow disturbances that arise when assumption 10 is violated are treated theoretically and observed experimentally in sections to follow.

Computations for the cases that follow were generally carried out by means of electronic computers so that it was possible to make many more comparisons than would have been possible by hand-operated machines.

Development of Equations Used in Numerical Solution of Flow Fields

Basic equations for liquid metal with a free surface.- In view of the excellent treatment given by Fraenkel (ref. 12) to the derivation of the equations that govern the motion of free-surface waves on a liquid metal in electric and magnetic fields, a detailed rederivation will not be given here. Instead, the

equations of motion for the fluid are presented together with the series expansions used for the various parameters to obtain the free-surface equations. Then, without going into the details of the intervening algebra, the final equations for the free surface are given. Conservation equations for the fluid and for the electromagnetic fields are, in vector notation (see appendix for definition of symbols),

$$\frac{\partial \rho}{\partial t} + \vec{\nabla} \cdot \rho\vec{U} = 0 \qquad \text{(Conservation of mass)}$$

$$\rho \frac{D\vec{U}}{Dt} + \vec{\nabla}p = \vec{J} \times \vec{B} - \rho\vec{G} \qquad \text{(Conservation of momentum)}$$

$$\rho \frac{D}{Dt}\left(e + \frac{U^2}{2}\right) + \rho \frac{D(p/\rho)}{Dt} = \vec{J} \cdot \vec{E} + \frac{\partial p}{\partial t} \qquad \text{(Conservation of energy)}$$

$$\vec{\nabla} \cdot \vec{B} = 0$$

$$\vec{\nabla} \cdot \epsilon\vec{E} = 0$$

$$\vec{\nabla} \times \vec{E} = -\frac{\partial \vec{B}}{\partial t}$$

$$\vec{\nabla} \times \vec{B} = \mu\vec{J} + \mu\epsilon \frac{\partial \vec{E}}{\partial t}$$

$$\vec{J} = \sigma(\vec{E} + \vec{U} \times \vec{B}) \qquad \text{(Ohm's law)}$$

The equation for the surface of the liquid metal is

$$\frac{\partial h}{\partial t} + u \frac{\partial h}{\partial x} + v \frac{\partial h}{\partial y} = w \qquad \text{at} \quad z = h(x,y,t)$$

The power series relations that are inserted into the foregoing equations to develop an ordered system of equations are made dimensionless by means of the following quantities: λ = wave length, h_O = characteristic depth of liquid, K = curvature of surface $\approx h_O/\lambda^2$, $\sqrt{gh_O} = a_O$ = speed of propagation of a small disturbance, B_O = reference magnetic field strength in z direction, and $\delta = h_O{}^2/\lambda^2$ with R_m = magnetic Reynolds number = $O(\delta)$. Hence, the coordinate axes and time are written as $X = x/\lambda$, $Y = y/\lambda$, $Z = z/h_O$, and $\tau = t\sqrt{gh_O}/\lambda$. Power series expressions for the various flow quantities are then

$$u = \sqrt{gh_o}\,(u_o + u_1\delta + u_2\delta^2 + \ldots)$$

$$v = \sqrt{gh_o}\,(v_o + v_1\delta + v_2\delta^2 + \ldots)$$

$$w = (\lambda\sqrt{gh_o}/h_o)(w_o + w_1\delta + w_2\delta^2 + \ldots)$$

$$p = \rho g h_o(p_o + p_1\delta + p_2\delta^2 + \ldots)$$

$$B_x = R_m B_o(B_{xo} + B_{x1}\delta + B_{x2}\delta^2 + \ldots)$$

$$B_y = R_m B_o(B_{yo} + B_{y1}\delta + B_{y2}\delta^2 + \ldots)$$

$$B_z = B_{zo} + R_m(B_{z1} + B_{z2}\delta + \ldots)$$

$$E_x = \sqrt{gh_o}\,B_o(E_{xo} + E_{x1}\delta + E_{x2}\delta^2 + \ldots)$$

$$E_y = \sqrt{gh_o}\,B_o(E_{yo} + E_{y1}\delta + E_{y2}\delta^2 + \ldots)$$

$$E_z = \sqrt{gh_o}\,R_m B_o(E_{zo} + E_{z1}\delta + E_{z2}\delta^2 + \ldots)$$

It is to be noted that the values of E_{xo} and E_{yo} depend on the specific boundary conditions imposed on the electric field. They can generally be made small or large as desired.

Insertion of these series expressions into the differential equations leads to a sequence of differential equations for the various terms in the power series. The set of differential equations that result from the zero order system in δ are used here to analyze the free-surface problems to be considered. Figures 1 and 2 indicate the orientation of the coordinate axes, magnet, and channel. The origin of the coordinate axes is fixed relative to the channel which is, in turn, fixed relative to the laboratory frame of reference. Equations that govern the motion of the free surface are then, after the various terms are returned to dimensional notation,

$$\frac{\partial h}{\partial t} + \frac{\partial hu}{\partial x} + \frac{\partial hv}{\partial y} = 0 \qquad \left\{\begin{matrix}\text{Conservation}\\ \text{of mass}\end{matrix}\right\} \tag{1}$$

$$\frac{\partial u}{\partial t} + u\frac{\partial u}{\partial x} + v\frac{\partial u}{\partial y} + g\frac{\partial h}{\partial x} = \frac{\sigma B_z}{\rho}(E_y - uB_z) \tag{2a}$$

$$\left.\begin{matrix}\\ \\ \end{matrix}\right\}\;\begin{matrix}\left\{\begin{matrix}\text{Conservation}\\ \text{of momentum}\end{matrix}\right\}\end{matrix}$$

$$\frac{\partial v}{\partial t} + u\frac{\partial v}{\partial x} + v\frac{\partial v}{\partial y} + g\frac{\partial h}{\partial y} = -\frac{\sigma B_z}{\rho}(E_x + vB_z) \tag{2b}$$

$$\frac{\partial B_z}{\partial t} = \frac{\partial E_x}{\partial y} - \frac{\partial E_y}{\partial x} \tag{3}$$

$$J_x = \sigma(E_x + vB_z) \tag{4a}$$

$$J_y = \sigma(E_y - uB_z) \tag{4b}$$

$$p = \rho g h \qquad \text{(Eq. of state)} \tag{5}$$

$$\rho\left[\frac{\partial}{\partial t}\left(e + \frac{u^2 + v^2}{2}\right) + u\frac{\partial}{\partial x}\left(e + \frac{u^2 + v^2}{2}\right) + v\frac{\partial}{\partial y}\left(e + \frac{u^2 + v^2}{2}\right)\right] + g\rho\left(\frac{\partial hu}{\partial x} + \frac{\partial hv}{\partial y}\right)$$

$$= J_x E_x + J_y E_y \qquad \text{(Conservation of energy)} \tag{6a}$$

or, by use of the equations for the conservation of mass and momentum, it is possible to write the energy balance as,

$$\frac{\partial e}{\partial t} + u\frac{\partial e}{\partial x} + v\frac{\partial e}{\partial y} = \frac{J^2}{\sigma\rho} \tag{6b}$$

where (see also appendix) u and v are the velocity components in the x and y directions, e, ρ, and h are the internal energy, density, and depth, respectively, of the liquid metal. The quantities E and J are the electric field intensity and current density, B_z is the vertical component of the magnetic induction, and σ is the electrical conductivity of the liquid metal. The electromagnetic equation relating the current and magnetic field, $\mu\vec{J} = \vec{\nabla} \times \vec{B}$, is not needed in this small magnetic Reynolds number approximation.

Equations for method of characteristics.- Since the problems to be considered are nearly a function of one space dimension (say x) and time, t, equations (1) through (6) simplify enough so that a solution for a given set of boundary conditions can be obtained by the so-called method of characteristics (see, e.g., Courant and Friedrichs, ref. 35). When the technique described in reference 35 is applied to equations (1) and (2) with v = 0, the two partial differential equations are reduced to ordinary differential equations that apply along the characteristic paths and are used as difference equations in finding a numerical solution to a given flow field. These equations, known as the characteristic equations, are

$$d(u \pm 2\sqrt{gh}) = \frac{\sigma B_z}{\rho}(E_y - uB_z)dt \qquad \text{along} \quad \frac{dx}{dt} = u \pm \sqrt{gh} \tag{7}$$

where the speed of propagation of a small wave is found to be $\sqrt{gh}$. In equation (7), and in the characteristic equations to follow, the $\pm$ notation is used to indicate that the upper signs apply along the forward (+x) facing and the lower signs along the backward (-x) facing characteristic directions. In the numerical work, it is found convenient to normalize the various terms with quantities that typify the problem being studied. The free-surface wave speed, $a_0 = \sqrt{gh_0}$, the

initial undisturbed depth of the liquid metal, h_O, the magnetic field strength at the center of the magnet, B_O, and the half-width of the channel, d, are used throughout the remainder of this paper to reduce the various quantities to dimensionless form. The characteristic equations then become, by equation (7),

$$d \left(\frac{u}{a_O} + 2\sqrt{\frac{h}{h_O}} \right) = \frac{\sigma B_O^2 d}{\rho a_O} \frac{B_z}{B_O} \left(\frac{E_y}{a_O B_O} - \frac{u}{a_O} \frac{B_z}{B_O} \right) d \left(\frac{ta_O}{d} \right) \qquad \text{along} \quad \frac{d(x/d)}{d(ta_O/d)} = \frac{u}{a_O} + \sqrt{\frac{h}{h_O}}$$

or

$$dP = d(U + 2A) = P_{mo} \, \mathbb{B} \left(\mathbb{E}_y - U \, \mathbb{B} \right) d\tau \qquad \text{along} \quad \frac{dX}{d\tau} = U + A \qquad (8a)$$

$$dQ = d(U - 2A) = P_{mo} \, \mathbb{B} \left(\mathbb{E}_y - U \, \mathbb{B} \right) d\tau \qquad \text{along} \quad \frac{dX}{d\tau} = U - A \qquad (8b)$$

where $U = u/a_O$, $A = \sqrt{h/h_O}$, $H = h/h_O$, $\mathbb{E}_y = E_y/a_O B_O$, $X = x/d$, $\mathbb{B} = B_z/B_O$, and $\tau = ta_O/d$. See appendix also.

Relations for flow variables across a strong wave front.- Since equations (7) and (8) apply only to waves that are weak, that is, of vanishingly small amplitude, another set of equations must be used for waves of finite strength or amplitude. As pointed out earlier, assumptions 1, 4, and 5 are violated at the front of such a wave because viscous and surface tension forces dictate the shape of the surface there. An analytic expression for the profile of the fluid surface through the wave would be difficult to derive. However, equations for the net change in the flow quantities from one side of the wave to the other can be found quite simply from expressions in common use for water waves (see, e.g., pp. 314ff of ref. 1). These so-called jump conditions across the wave will be used at the wave front only and the characteristic equations (8) for small waves throughout the rest of the flow field. Since changes in the flow parameters across the wave at a given instant of time are not affected by electromagnetic forces, the equations for water waves apply without modification. Hence, from reference 1, expressions that relate flow quantities on both sides of a strong wave are

$$U_p^2 = \frac{u_p^2}{gh_O} = \frac{1}{2H_W} (H_W + 1)(H_W - 1)^2 \qquad (9a)$$

$$U_W = \frac{U_p H_W}{H_W - 1} \qquad (9b)$$

$$A_W = \sqrt{H_W} \qquad (9c)$$

$$P_W = U_p + 2A_W \qquad (9d)$$

where $U_p = u_p/a_O$ is the dimensionless velocity of the piston pushing the fluid, $U_W = u_W/a_O$ is the dimensionless velocity of the wave (see fig. 4), and P_W is

9

the characteristic quantity just behind the wave crest. The velocity ahead of the wave is assumed to be zero. Tabulated values for these parameters are presented below as a function of the fluid depth ratio across the wave, $H_W = h_W/h_O$.

H_W	U_p	U_W	A_W	P_W
1.0	0	1.0	1.0	2.0
1.1	.09770	1.07471	1.04881	2.19532
1.2	.19149	1.14891	1.09544	2.38238
1.3	.28216	1.22270	1.14018	2.56251
1.4	.37033	1.29615	1.18322	2.73676
1.5	.45643	1.36929	1.22475	2.90592
1.6	.54083	1.44222	1.26491	3.07066
1.7	.62379	1.51493	1.30384	3.23147
1.8	.70553	1.58745	1.34164	3.38882
1.9	.78623	1.65982	1.37840	3.54304
2.0	.86603	1.73205	1.41421	3.69445

Examples of numerical solutions.- Figure 5(a) presents the theoretical surface height and figure 5(b) the velocity of the fluid caused by a small wave in mercury as it impinges on the field of a magnet. The electric field E_y has been set equal to zero. In the solution shown, the strong wave relations were not used at the wave front because the wave considered in the calculations is not strong enough to cause a detectable error and the numerical work was simplified by such an approximation. In all the calculations pertaining to the experiments, however, the strong wave relations are used because those waves are not small. Also shown in figure 5 is the variation with x/d assumed for the body force parameter, $P_m = \sigma B_z d/\rho a_O$, in the computations. Surface profiles at the various instants of time depict the attenuation of the incident wave as it moves through the magnetic field and the fluid reflected from the diffuse boundary of the magnetic field.

A theoretical prediction of the flow that results when the piston is withdrawn from the liquid metal in a transverse magnetic field is illustrated in figure 6. A centered expansion in gas dynamics (or breaking of a dam in hydraulics) corresponds to the solution shown. A large difference is to be noted in the surface between the cases with and without a magnetic field applied. Most apparent is the lower level of the liquid at the piston when the magnetic field is applied. When the piston has receded a short distance in the magnetic case, the surface shape changes quite slowly as the fluid seeps through the magnetic field. The same variation of the body force parameter shown in figure 5 was assumed in these calculations.

A different interpretation must be given to the characteristic equations when the magnet moves past the fluid and channel as illustrated in figure 2. An addition of the electric field, $u_m B_z$, caused by this relative motion to equations (7) and (8) accomplishes the modifications necessary for the present purposes. The characteristic equations for the fluid set in motion by the moving magnet written in dimensionless notation are then

$$\left.\begin{array}{c} \mathrm{dP} \\ \mathrm{dQ} \end{array}\right\} = \mathrm{d}(\mathrm{U} \pm 2\mathrm{A}) = \mathrm{P_m} \, \mathbb{B} \left[\mathbf{E}_y - (\mathrm{U} - \mathrm{U_m}) \, \mathbb{B} \right] \mathrm{d}\tau \qquad \text{along} \quad \frac{\mathrm{dX}}{\mathrm{d}\tau} = \mathrm{U} \pm \mathrm{A} \qquad (10)$$

where $U_m = u_m / \sqrt{gh_0}$ with u_m = magnet velocity.

A solution that illustrates the fluid motion that results when a magnet moves past a fluid initially at rest as calculated by equation (10) is shown in figure 7. Once again, it is assumed that the electric field, $\mathbf{E}_y$, is zero and that the variation of P_m is the same as shown in figure 5. Positions of the leading edge of the magnet generating the force field are indicated at the various instants of time by lines at the top of the figure. It is noted in figure 7 that the magnetic field pushes fluid ahead of it in a way remindful of the sweeping action of a broom.

It remains in this section to present the characteristics equations to be used in the analysis of the nonsteady flow fields illustrated in figures 3(a) and 3(b) because the fluid motion is in the y and in the radial directions rather than along the x axis. Equations (1) and (2b) with u = 0 are used for the two-dimensional model, figure 3(a). When the method of reference 35 is applied to these equations, the characteristics equations are found to be

$$\mathrm{d}(v \pm 2a) = -\frac{\sigma B_z}{\rho} (E_x + vB_z)\mathrm{d}t \qquad \text{along} \; \frac{\mathrm{d}y}{\mathrm{d}t} = v \pm a \qquad (11)$$

Similarly, after equations (1) and (2) for the conservation of mass and momentum are written in cylindrical (r, φ, z) coordinates and after variations with respect to φ are set equal to zero, the characteristics equations for the axially symmetric model illustrated in figure 3(b) are found as

$$\mathrm{d}(u_r \pm 2a) = \mp \frac{au_r}{r} \mathrm{d}t + \frac{\sigma B_z}{\rho} (E_\varphi - u_r B_z)\mathrm{d}t \qquad \text{along} \; \frac{\mathrm{d}r}{\mathrm{d}t} = u_r \pm a \qquad (12)$$

where r is the radius and u_r is the radial velocity. In equations (11) and (12), E_x and E_φ depend, of course, on the rate of change of the magnetic field (see eq. (3)) with time, and on the nature of the boundary of the flow field. A theoretical estimation of the magnitudes of these quantities to be expected in an experiment is presented in a subsequent section entitled "Surface Shape as Magnet is Energized."

Appraisal of Analogy Between Free-Surface and Gas-Dynamic Models

In order to have some sort of an understanding of how well a gas-dynamic phenomenon is represented by the comparable free-surface situation, the differential equations for an idealized electrically conducting gas and a numerical comparison of results computed for particular cases by these equations are presented in this section. At the outset, it is obvious that the analogy will not duplicate the deviations from a perfect gas nor the chemical reactions that are common to

the flow of ionized gases. If the gas is assumed to be of an idealized sort that does not possess these variable properties,[2] some doubt still remains as to the extent to which the free-surface analogy applies.

For the present purposes, an idealized gas that has the following characteristics will be assumed.

1. Constant specific heats and electrical conductivity throughout its volume and during event.

2. Boundary conditions are the same as for liquid metal. Restrictions 1, and 8 through 13, that were imposed previously on the free-surface waves, apply here also. The gas-dynamic differential equations for this simplified gas, written for two space dimensions and time, are then,

$$\frac{\partial \rho}{\partial t} + \frac{\partial \rho u}{\partial x} + \frac{\partial \rho v}{\partial y} = 0 \qquad \left\{ \begin{matrix} \text{Conservation} \\ \text{of mass} \end{matrix} \right\} \qquad (13)$$

$$\frac{\partial u}{\partial t} + u \frac{\partial u}{\partial x} + v \frac{\partial u}{\partial y} + \frac{1}{\rho} \frac{\partial p}{\partial x} = \frac{\sigma B_z}{\rho} (E_y - u B_z) \qquad (14a)$$

$$\left. \begin{matrix} \\ \\ \end{matrix} \right\} \quad \left\{ \begin{matrix} \text{Conservation} \\ \text{of momentum} \end{matrix} \right\}$$

$$\frac{\partial v}{\partial t} + u \frac{\partial v}{\partial x} + v \frac{\partial v}{\partial y} + \frac{1}{\rho} \frac{\partial p}{\partial y} = - \frac{\sigma B_z}{\rho} (E_x + v B_z) \qquad (14b)$$

$$p = \rho R T \qquad \text{(Eq. of state)} \qquad (15)$$

$$\rho \left[\frac{\partial \left(e + \frac{u^2 + v^2}{2} \right)}{\partial t} + u \frac{\partial}{\partial x} \left(e + \frac{u^2 + v^2}{2} \right) + v \frac{\partial}{\partial y} \left(e + \frac{u^2 + v^2}{2} \right) \mp \frac{\frac{\partial p}{\rho}}{\partial t} + u \frac{\frac{\partial p}{\rho}}{\partial x} + v \frac{\frac{\partial p}{\rho}}{\partial y} \right]$$

$$= J_x E_x + J_y E_y + \frac{\partial p}{\partial t} \qquad \text{(Conservation of energy)} \qquad (16a)$$

or, by means of the momentum equation, the energy equation becomes

$$\rho \left(\frac{\partial e}{\partial t} + u \frac{\partial e}{\partial x} + v \frac{\partial e}{\partial y} \right) = \frac{J^2}{\sigma} + \frac{p}{\rho} \left(\frac{\partial \rho}{\partial t} + u \frac{\partial \rho}{\partial x} + v \frac{\partial \rho}{\partial y} \right) \qquad (16b)$$

Equations (13) through (15) are identical with equations (1), (2), and (5) if the surface height, h, corresponds to the density, ρ, and the temperature, T, of the gas. The pressure, p, is proportional to h^2. It is noted, however, that

---

[2]Perhaps by choosing the variety of gas, and/or temperature range of the experiment, it would be possible to match the free-surface and gas-dynamic cases very closely.

equations (6b) and (16b) for the internal energy of the liquid metal and the gas do not contain the same terms because the gas density is much more sensitive to joule heating and to pressure than is the liquid metal. This difference is pronounced clearly in the one-dimensional unsteady state form of the characteristic equations for the gas that can be derived from equations (13) to (16) (see, e.g., ref. 35). The speed of propagation of a small wave is now $a = \sqrt{dp/d\rho} = \sqrt{\gamma p/\rho}$, where $\gamma = C_p/C_v$.

$$d\left(u \pm \frac{2a}{\gamma - 1}\right) = \frac{\sigma B_z}{\rho}(E_y - uB_z)dt \pm \frac{aJ^2}{\sigma p}dt \qquad \text{along } \frac{dx}{dt} = u \pm a \qquad (17)$$

where $aJ^2/\sigma p = a(dS/R)$, with S as the entropy and R as the gas constant. If $\gamma = 2$, the left side of equations (7) and (17) are the same.[3] The first term to the right of the equal sign in each of these equations are also the same if the density for the gas is a constant as it is for the liquid metal. Since such is not the case, the integration of this term along the characteristic direction requires that ρ be a variable in equation (17). The second term on the right of equation (17) expresses energy added to the gas by joule heating, J^2/σ, due to the flow of electrical currents, and is an expression of the entropy of the various fluid elements involved in the integration along the characteristic paths. Numerical values for this term are found by following the path of each fluid element and determining the heat energy added to it since the inception of the event. Inasmuch as no corresponding term exists in the free-surface equations (eq. (7)), the size of this quantity will largely determine the difference between the gas and free-surface solutions. Since the joule heating is cumulative, the entropy term grows with time. Hence, the analogy should be best at the earlier stages of a given interaction and become worse as time progresses.

Comparison of the flow solution for a gas-dynamic model that is the same as the free-surface model analyzed in figure 5 with data shown there illustrates the applicability of the analogy (see figs. 8(a) and 8(b)). As before, E_y is assumed to be zero. Also, the dimensionless flow variables and sizes of the channels used in the two flow situations are assumed to be identical; that is, $(u_p/a_o)_{gas} = (u_p/a_o)_{free surface}$, etc.

Variations of the density, pressure, temperature, and velocity with distance along the channel at several instants of time are presented in figure 8 for both a gas-dynamic and free-surface small compression wave impinging on a magnetic field. As expected, the density and velocity for the two mediums correspond quite well during the early stages of the interaction but the difference grows with time. Despite the increasing quantitative spread between the two solutions, qualitative agreement exists at all times. Temperature and pressure in the gas are not represented quantitatively in any decent fashion by the free-surface solution for $\gamma = 1.4$ (or any γ other than 2), although a qualitative representation of a sort is observed.

---

[3]Such is the case for a completely ionized gas embedded in a magnetic field because it has two degrees of freedom and therefore a γ of 2.

Effect of Boundaries on Electric Field

All the foregoing calculations were made by assuming that the electric field E_y was zero. In practice, the boundaries of the flow field will modify the electric current lines in such a way that E_y will no longer be negligible and that sizable currents may flow in directions not anticipated by strictly one-dimensional considerations. To gain an understanding of the influence of the boundaries on the electric current system, theoretical consideration will be given here to certain idealized situations that approximate the experimental conditions. Several possible current paths for the two sets of boundary conditions used in the wave experiments are illustrated schematically in the upper part of figure 9. In the first case, figure 9(a), the liquid metal is bounded on both sides and on the bottom by clear plastic walls that are insulators. The electric currents must then flow in closed paths within the fluid. Since an electric field is induced within any fluid element that moves relative to the magnetic field B_z, the electric currents can close on themselves by passing through the viscous boundary layer that exists on the walls of the channel and by means of loops that extend upstream and downstream of the moving fluid (or of the magnetic field - whichever results in the shortest path) as shown in figures 9(a) and 9(c). In the second case, a copper plate is placed on the bottom of the channel (fig. 9(b)) to provide an additional path for the electric currents to flow. The various electric current paths are parallel so that some current will flow through each of them during an experiment. In a given situation, however, one circuit will probably carry more current than the rest. It is immediately apparent that very little electricity will flow through the viscous boundary layer (fig. 9(a)) because of its small depth and therefore high resistance. An estimate of this resistance is obtained from the work of Hartmann (ref. 36). He finds the displacement thickness of the boundary layer is approximately $1/(B_z \sqrt{\sigma/\eta})$, or less than 0.01 cm (1/350 in.) for the experiments reported here. Therefore, no further consideration will be given to electric currents that may flow in the viscous boundary layer because their influence on the flow is believed to be negligible.

In the three subsections to follow, an estimate will be made of E_y under three sets of boundary conditions on the electric field that arise from the situations illustrated in figures 9(a) and 9(b). In the first case, it is assumed that an external circuit is provided for the electric current filaments so that the electric field is nearly one-dimensional and special consideration need only be given to the resistance of the return circuit. In the second and third cases, all boundaries of the flow field are assumed to be insulators so that the electric current loops are forced to close within the fluid. Case two assumes that the fluid-magnetic interaction takes place in an area small compared with dimensions of the container enclosing the flow field. These results are extended in case three to the electric field that results from the interaction between two insulating walls. This latter situation corresponds closely to the channel problem when no external circuit is provided for the return of the electric currents. In each of these cases the depth of the fluid is taken to be constant throughout the flow field so that the problem may be treated as two-dimensional. Also, motion of the fluid element will be assumed to be steady with time and uniform throughout the moving element.

In what follows, it is necessary to define clearly the meaning of the various symbols used. The actual electric current density distribution in the flow field when a given fluid element moves through a magnetic field is represented by $\vec{J} = \sigma(\vec{E} + \vec{U} \times \vec{B})$. The quantity $\vec{U} \times \vec{B}$ is the local induced electric field brought about by the motion of the fluid element through the magnetic field. It is assumed that the motion of the fluid and the magnitude of the magnetic field is uniform throughout the element so that it is represented by the one-dimensional value denoted as $u_0 B_0$. Since no external electric field will be impressed on the flow field, the quantity $\vec{E}$ expresses that electric field required to cause the electric currents to conform with the boundaries of the liquid metal conductor and the return circuit (if one is provided). Hence, $\vec{E}$ depends on $u_0 B_0$ directly for its magnitude and on the shape of the moving fluid element and the flow field boundaries for its plan-view representation.

One-dimensional approximation for electric field.- When an adequate external circuit is provided for the electric currents to flow in their natural transverse (y) direction, the resultant body force on the moving fluid element is along the channel in the x direction. Laboratory conditions are such that a voltage difference is required to force the current filaments to flow over their return circuit. In a strictly one-dimensional sense, this resistance can be allowed for by a reduction in the magnitude of the induced field; that is, assume

$$J_y = \sigma(E_y - uB_z) \approx -C\sigma uB_z \qquad (18)$$

where C is a constant for a given experiment that depends on the boundary conditions imposed on the electric currents. It will always be less than one in magnitude, and will be referred to as the electric field constant. Equation (8) then becomes

$$\left.\begin{array}{c} dP \\ dQ \end{array}\right\} = d(U \pm 2A) = -CP_{mo}U\,B^2\,d\tau \qquad \text{along } \frac{dX}{d\tau} = U \pm A \qquad (19)$$

Such an idealization reduces the analysis to a consideration of only one space dimension and time, thereby making it possible to obtain numerical solutions for the various free-surface wave experiments. All computations of fluid motions presented in this paper were carried out by use of this method of approximation.

An estimate for an upper bound to the value of the electric field constant C for a channel with a copper bottom can be obtained by considering the resistance of that circuit. Within a given moving fluid element, the impressed potential is $2duB_z$ where 2d is the width of the channel. The resistance[4] of the circuit per unit length of the channel is then $R = (2d/\sigma h) + (2d/\sigma_{cu}h_{cu})$ where σ and h are the conductivity and depth of the liquid metal, and σ_{cu} and h_{cu} are the conductivity and thickness of the copper bottom. The electric current per unit length of the bar, I_y, is then given by

$$I_y = -\frac{2duB_z}{R} = -\sigma B_z uh \frac{1}{1 + \dfrac{\sigma}{\sigma_{cu}} \cdot \dfrac{h}{h_{cu}}}$$

---

[4]Contact resistance between the liquid metal and the copper adds to the resistance (lowers C) of that circuit. No estimate is made here of its magnitude.

Since this result must be equivalent to equation (18), the electric field constant is given approximately as

$$C = \cfrac{1}{1 + \cfrac{\sigma}{\sigma_{cu}} \cfrac{h}{h_{cu}}}$$

where $J_y = I_y/h$. If the copper plate is taken as 1/4 inch thick, the fluid depth as 1/2 inch, and the fluid as mercury, the constant is about 0.96, if the contact resistance between the mercury and copper plate is negligible in comparison with $2duB_z$. A comparable value for NaK is about 0.90. These values are indicative only and cannot be considered as firm figures for C.

Electric currents for element of finite size in unbounded medium.— A theoretical estimate of the electric field strength and current lines for a fluid element as it moves through a magnetic field (see fig. 10(a)) will now be found by the method of doublets. An equivalent system, shown in side view in figure 10(b), consists of a fluid at rest and a magnet moving past it. The electric current distributions of these two systems are identical if the magnet speed in figure 10(b) is the same as the fluid velocity in the block shown in figure 10(a). For either of these two systems, the induced electric field is represented by a two-dimensional or planar doublet with its axis alined with the induced electric field, $\vec{U} \times \vec{B}$, (y direction) and its strength equal to $\sigma u_0 B_0$. The conductivity is included because the final expressions then yield the actual electric currents that flow in the fluid when such motion exists. For convenience, the shape and motion of the fluid element to be considered are assumed to be uniform throughout a rectangular element (see fig. 11).

The complex potential for a doublet in an unbounded medium is

$$\Phi_u = \varphi_u + i\psi_u = -\sigma \frac{u_0 B_0}{2\pi} \frac{i}{\zeta - \zeta_0} \tag{20}$$

where $i = \sqrt{-1}$, $\zeta = x + iy$, and φ_u and ψ_u are the potential and stream functions for the electric field. The location of the doublet with respect to the origin ($\zeta = 0$) is given by $\zeta_0 = x_0 + iy_0$. When the summation is carried out by integration over an area 2L units wide and 2D units long (fig. 11), the field quantities for a rectangular block of emf in an unbounded medium are then found as

$$\varphi_u = \frac{\sigma u_0 B_0}{2\pi} \left[(y - L)\left(\cot^{-1} \frac{y - L}{x + D} - \cot^{-1} \frac{y - L}{x - D} \right) - (y + L)\left(\cot^{-1} \frac{y + L}{x + D} - \cot^{-1} \frac{y + L}{x - D} \right) \right.$$

$$\left. + \frac{x + D}{2} \ln \frac{(x + D)^2 + (y - L)^2}{(x + D)^2 + (y + L)^2} + \frac{x - D}{2} \ln \frac{(x - D)^2 + (y + L)^2}{(x - D)^2 + (y + L)^2} \right] \tag{21a}$$

16

$$\psi_u = -\frac{\sigma u_o B_o}{2\pi} \left[\frac{y-L}{2} \ln \frac{(x-D)^2 + (y-L)^2}{(x+D)^2 + (y-L)^2} - \frac{y+L}{2} \ln \frac{(x-D)^2 + (y+L)^2}{(x+D)^2 + (y+L)^2} \right.$$

$$\left. + (x-D)\left(\tan^{-1} \frac{y-L}{x-D} - \tan^{-1} \frac{y+L}{x-D} \right) + (x+D)\left(\tan^{-1} \frac{y+L}{x+D} - \tan^{-1} \frac{y-L}{x+D} \right) \right]$$

$$\text{(21b)}$$

$$J_x = \frac{\sigma u_o B_o}{2\pi} \ln \frac{[(x+D)^2 + (y-L)^2][(x-D)^2 + (y+L)^2]}{[(x+D)^2]+ (y+L)^2][(x-D)^2 + (y-L)^2]} \qquad \text{(21c)}$$

$$J_y = \frac{\sigma u_o B_o}{2\pi} \left(\tan^{-1} \frac{x+D}{y-L} - \tan^{-1} \frac{x-D}{y-L} - \tan^{-1} \frac{x+D}{y+L} + \tan^{-1} \frac{x-D}{y+L} \right) \qquad \text{(21d)}$$

Electric current lines (i.e., lines of constant ψ) for two sizes of the rectangle are shown in figure 12. The electric current density distribution for $L/D = 3$ is illustrated in figure 13. Theoretically, the quantity J_y should be equal to $\sigma u_o B_o$ for a truly one-dimensional model instead of a value of about $0.8\ \sigma u_o B_o$ found for figure 13.

Electric currents for element between two nonconducting walls.- Comparable information for the bounded medium is obtained by an integration of the expression for a doublet between two walls $2d$ units apart as shown in figure 14. The complex potential for a single doublet in a bounded medium is

$$\Phi_1 = \varphi_1 + i\psi_1 = \frac{\sigma u_o B_o}{2\pi} \frac{i}{d \sinh \frac{\zeta \pi}{2d} - i\zeta_o}$$

where $\zeta_o = x_o + iy_o$. When this equation is integrated with respect to x_o from $-D$ to $+D$, expressions for the potential and stream function φ_s and ψ_s, and for the components of the electric current density for a doublet layer or slab (fig. 14) bounded by two insulating walls are found to be

$$\varphi_s = \frac{\sigma u_o B_o}{2\pi} \left(\tan^{-1} \frac{\xi 1}{\xi 2} - \tan^{-1} \frac{\xi 1}{\xi 3} \right) \qquad \text{(22a)}$$

$$\psi_s = \frac{\sigma u_o B_o}{2\pi} \left[\ln \frac{(\xi 1)^2 + (\xi 3)^2}{(\xi 1)^2 + (\xi 2)^2} \right] \qquad \text{(22b)}$$

$$J_{x_s} = \frac{\sigma u_0 B_0}{4d} \left[\frac{\cos \frac{y\pi}{2d} \sin \frac{y\pi}{2d} - \cosh \frac{x\pi}{2d} \cosh \frac{D\pi}{2d} \cos \frac{y\pi}{2d} \sin \frac{Y_0\pi}{2d} + \sinh \frac{x\pi}{2d} \sinh \frac{D\pi}{2d} \sin \frac{y\pi}{2d} \cos \frac{Y_0\pi}{2d}}{(\xi 1)^2 + (\xi 2)^2} \right.$$

$$\left. - \frac{\cos \frac{y\pi}{2d} \sin \frac{y\pi}{2d} - \cosh \frac{x\pi}{2d} \cosh \frac{D\pi}{2d} \cos \frac{y\pi}{2d} \sin \frac{Y_0\pi}{2d} - \sinh \frac{x\pi}{2d} \sinh \frac{D\pi}{2d} \sin \frac{y\pi}{2d} \cos \frac{Y_0\pi}{2d}}{(\xi 1)^2 + (\xi 3)^2} \right]$$

$$(22c)$$

$$J_{y_s} = -\frac{\sigma u_0 B_0}{4d} \left[\frac{\cosh \frac{x\pi}{2d} \sinh \frac{x\pi}{2d} - \cosh \frac{x\pi}{2d} \sinh \frac{D\pi}{2d} \cos \frac{y\pi}{2d} \cos \frac{Y_0\pi}{2d} - \sinh \frac{x\pi}{2d} \cosh \frac{D\pi}{2d} \sin \frac{y\pi}{2d} \sin \frac{Y_0\pi}{2d}}{(\xi 1)^2 + (\xi 2)^2} \right.$$

$$\left. - \frac{\cosh \frac{x\pi}{2d} \sinh \frac{x\pi}{2d} + \cosh \frac{x\pi}{2d} \sinh \frac{D\pi}{2d} \cos \frac{y\pi}{2d} \cos \frac{Y_0\pi}{2d} - \sinh \frac{x\pi}{2d} \cosh \frac{D\pi}{2d} \sin \frac{y\pi}{2d} \sin \frac{Y_0\pi}{2d}}{(\xi 1)^2 + (\xi 3)^2} \right]$$

$$(22d)$$

where

$$\xi 1 = \cosh \frac{x\pi}{2d} \sin \frac{y\pi}{2d} - \cosh \frac{D\pi}{2d} \sin \frac{Y_0\pi}{2d}$$

$$\xi 2 = \sinh \frac{x\pi}{2d} \cos \frac{y\pi}{2d} - \sinh \frac{D\pi}{2d} \cos \frac{Y_0\pi}{2d}$$

$$\xi 3 = \sinh \frac{x\pi}{2d} \cos \frac{y\pi}{2d} + \sinh \frac{D\pi}{2d} \cos \frac{Y_0\pi}{2d}$$

Numerical integration of equations (22) with respect to Y_0 for the idealized emf distribution shown in figure 14 leads to the electric current lines and field intensity distributions shown in figures 15 and 16. As is to be expected, a comparison of figures 13 and 16 reveals that the presence of the insulating boundaries reduces considerably but not entirely the magnitude of the electric current density for a given input driving potential distribution.

In any real experiment, the magnetic field (or fluid velocity) is generally not accurately represented by a step function at the boundaries of the moving parts. An analysis of the magnetic field to be used here as measured for the 4- by 4-inch solid core magnet with a 1-1/2-inch air gap that was used in the tests will indicate the electric field to be expected when the magnet moves relative to a fluid of

uniform depth. If equations (22) are integrated for the distribution shown in figure 17(a), approximated by the step functions shown, the electric current lines and current density distributions are found as illustrated in figures 17(b), 17(c), and 17(d). The experimental magnetic field is nearly constant across the channel and is assumed therefore to be only a function of x. In figures 17, a remarkable reduction in the electric current density is observed when it is compared with the value that would be assumed in a one-dimensional analysis; that is, $J_y = \sigma u_0 B_z$. Longitudinal (x direction) currents are noted to be of the same magnitude as the transverse (y direction) currents, thereby indicating that the cross-channel forces are as large as the longitudinal forces. The directions of the forces that act on the medium in that quadrant of the force field are illustrated by the arrows shown in figure 17(b).

Surface Shape as Magnet is Energized

Numerical analysis of the nonsteady flow fields that arise when the magnet is energized is carried out by means of the characteristic equations presented previously as equations (11) and (12). Before these equations can be employed, relations must be developed for the electric fields E_x and E_φ and for the magnetic field B_z as a function of time. A qualitative description of the fluid motion to be anticipated in such an event will first be given in this section; then, the required expressions will be developed for the various fields.

When the magnet is energized, the liquid metal is drawn to the center of the magnet by the induced body forces (fig. 18(a)). When the switch is opened so that the magnetic field decays quickly, the fluid is thrown violently in an outward direction from the center of the magnet (fig. 18(b)). The body forces that cause this motion arise from a combination of the electric field induced by the changing magnetic field (see eq. (3)) and the instantaneous value of the magnetic field. At time zero (i.e., when the magnetic field is zero), the induced electric field is a maximum because the magnetic field is changing most rapidly; but the body force is zero because the magnetic field strength is zero. When the magnetic field is fully established, the electric field vanishes (because the magnetic field is no longer changing with time) and the induced body force is again zero. It is only during the intervening time that the electric and magnetic fields are both nonzero and an acceleration is imparted to the liquid metal. An estimate of the surface shape as it changes with time will be made for the case when the magnetic field builds up, but no effort will be made to predict the flow when the magnet is turned off.

If the magnet had a constant value of the inductance **L** and resistance R the magnetic field strength as a function of time would be given by

$$B_z(t) = B_0 \left(1 - e^{-Rt/\mathbf{L}} \right) \tag{23}$$

where B_0 is the final steady-state value of the magnetic field. The electric field and body force F_y distribution in the fluid are then given for two-dimensional boundaries by equations (3) and (2) as

19

$$E_x = \frac{yB_oR}{L} e^{-Rt/L} \tag{24a}$$

$$F_y = -\sigma B_z(E_x + vB_z)$$

$$= -\sigma B_o^2 \left(1 - e^{-Rt/L}\right)\left[\frac{yR}{L} e^{-Rt/L} + v\left(1 - e^{-Rt/L}\right)\right] \tag{24b}$$

and for axially symmetric boundaries by

$$E_\varphi = -\frac{B_oR}{2L} e^{-Rt/L} \tag{25a}$$

$$F_r = -\sigma B_o^2 \left(1 - e^{-Rt/L}\right)\left[\frac{Rr}{2L} e^{-Rt/L} + u_r\left(1 - e^{-Rt/L}\right)\right] \tag{25b}$$

where r is the radius from the origin to the fluid element and u_r is the radial velocity of the fluid. However, the solid iron-core magnet used in the experiments is energized by a motor-generator set connected through a control box designed to promote optimum operation of a carbon-arc lamp. Voltage supplied to the magnet was then not a constant but varied with the current and time. The inductance or rate of change of the magnetic field with time is then a function of the electric current through the magnet windings (or instantaneous value of the magnetic field), the rate of change of the current, and several other factors that depend on the circuitry of the control panel. Several curves that represent the current through the magnet coils as a function of time are shown in figure 19 as measured on an oscilloscope. A noticeable deviation from the idealized exponential variation is especially apparent in the run conducted at a maximum current of 14.4 amperes. These peculiar variations of the magnet can be represented by a power series in electric current for the inductance; that is,

$$L = L_o + L_1I + L_2I^2 + L_3I^3 + \ldots$$

In the analysis to follow, only the first two terms of the series are retained so that the time constant of the magnet is expressed as

$$\frac{L}{R} = \frac{L_o + L_1I}{R}$$

An idealized form of the differential equation for the current, I, through the windings is then

$$E_o = RI + (L_o + L_1I)\frac{dI}{dt} \tag{26}$$

where E_O is a constant voltage applied at the initial instant of time, $t = 0$. Since it is assumed that E_O is constant and the current I is zero when $t = 0$, an expression that relates the time required for the current in the windings to rise to a given value is found as

$$t = -\frac{L_O}{R} \ln \left(1 - \frac{RI}{E_O}\right) - \frac{L_1}{R^2} \left[RI + E_O \ln \left(1 - \frac{RI}{E_O}\right)\right] \tag{27}$$

The emf induced in the liquid metal by the changing magnetic field becomes, for the two-dimensional case,

$$E_x = y \frac{dB_z}{dt} = y \frac{dB_z}{dI} \frac{dI}{dt}$$

and for axially symmetric case,

$$E_\varphi = -\frac{r}{2} \frac{dB_z}{dt} = -\frac{r}{2} \frac{dB_z}{dI} \frac{dI}{dt}$$

After the current, I, at a given instant, t, has been determined from equation (27), the quantity dB_z/dI is found by numerically differentiating the curve measured for B_z versus I (see fig. 20). Equation (26) is then used to find the factor dI/dt. It is assumed that B_z is a function only of time and not of x or y over the area of interest. The foregoing maneuver is an attempt to match the theoretical analysis with the experimental conditions as closely as possible. The characteristic equations for the two-dimensional case can then be written as, from equation (11),

$$d(v \pm 2\sqrt{gh}) = -\frac{\sigma B_z}{\rho} \left(y \frac{dB_z}{dI} \frac{dI}{dt} + vB_z\right) dt \quad \text{along} \quad \frac{dy}{dt} = v \pm \sqrt{gh} \tag{28}$$

Similarly, the equations for the axially symmetric flow are from equation (12)

$$d(u_r \pm 2\sqrt{gh}) = \mp \sqrt{gh} \frac{u_r}{r} dt - \frac{\sigma B_z}{\rho} \left(\frac{r}{2} \frac{dB_z}{dI} \frac{dI}{dt} + u_r B_z\right) dt \quad \text{along} \quad \frac{dr}{dt} = u_r \pm \sqrt{gh} \tag{29}$$

An electric field constant is obviously not required for the axially symmetric problem because the electric current loops are circles in the horizontal plane that are enclosed within the liquid metal. Also, the same induced potential exists along the entire current path.

In the two-dimensional case, however, the electric current paths extend into the liquid metal out beyond the magnet where an induced emf is not acting to aid the current. An estimate of the magnitude by which the theoretical and purely two-dimensional current distribution is changed by these end conditions is obtained by

use of a doublet distribution to simulate the electric field. To simplify the computations, the magnetic field is approximated by a uniform field over a certain length along the channel and zero elsewhere as indicated by the cross-hatched area in figures 21(a) and (b). It is found that the y variation of the electric field is represented by equation (24a) within the accuracy of the computations (less than 0.1-percent error) over the region of interest. Current paths for several values of the ratio, L/D, are shown in figures 21(a) and 21(b) and for the magnet used in the experiments in figure 21(c).

EXPERIMENT

Apparatus

A description is given here of the elements used to obtain the test data. Basic to each of the experimental arrangements was the 4- by 4-inch solid iron core electromagnet that has a 1-1/2-inch air gap. It was energized by about 1800 turns of number 14 magnet wire that received power from the motor-generator set discussed in the previous section. The magnetic field strength of the magnet on a horizontal plane midway between the pole faces is shown as a function of the longitudinal coordinate, x, in figure 22(a). Contours of equal field strength are shown in figure 22(b). Since the channels used in the experiments are 2 inches wide, any variations in the magnetic field strength across the channel were not measurable. Throughout the investigation, the magnetic field is considered a function only of the longitudinal or x coordinate.

Three test channels were used in the experiments. Each was made of clear plastic (lucite) that would not react chemically with NaK at room temperatures. All three test cells were equipped with plumbing so that dry nitrogen could be forced through the channel to purge it of oxygen and water vapor before NaK or mercury was introduced into the test cell through another plumbing duct. These test cells are described briefly as follows.

Channel 1: A rectangular box with internal dimensions of 1-1/4 inches high, 2 inches wide, and 37 inches long. A piston was propelled by a reversible direct-current motor at speeds from about 1 in./sec to 10 in./sec over a distance of 20 inches along the channel. See figure 1; not drawn to scale.

Channel 2: Rectangular box with internal dimensions of 1-1/8 inches high, 2 inches wide, and 48 inches long. A barrier 14 inches from the right end served as a retainer so that the rolling magnet could approach and pass a sharp liquid metal boundary. The magnet was rolled past the channel by means of a reversible electric motor connected to a lead screw via a carriage that rode on the lead screw. Excessive vibrations required that the magnet be pushed by hand for some of the tests with mercury. See figure 2; not drawn to scale.

Channel 3: Cylindrical box with internal dimensions of 1-1/4 inches high and 2-1/2 inches diameter. See figure 3(b); not drawn to scale.

Copper bars 1/4 inch thick, 2 inches wide, and 36 inches long were placed inside Channels 1 and 2 for several of the experiments. A piece of copper 1/4-inch thick and 2-1/2-inches diameter was used in the bottom of test cell number 3. These copper plates were not fastened rigidly to the channels but they fit closely enough to the side walls and bottom that any motion required a notable force.

Procedure

Photographic sequences of the profile of the surface shape of the liquid metal were obtained with a 70-mm camera set to take 20 frames/second. A clock with a 1-foot-diameter face and calibrated in 0.01-second intervals was placed within the field of view so that the instant at which each exposure was made was recorded and could later be determined to ±0.002 second. Selected frames were enlarged to about full-scale size so that the fluid motion could be studied in detail and so that readings of the surface height could be made easily and with some accuracy; that is, about ±0.01 inch. A transparent diagonal (45°) gridwork was placed in the background so that the top edge of the liquid metal could be accurately determined as the point at which the line and its reflection form a sharp point. Horizontal gridwork served as reference lines for the vertical measurements. A 48-inch neon lamp placed directly behind the test channel supplied the light for the exposures. The center of the camera lens was about 10 feet from the liquid metal and 1 inch higher on a line perpendicular to the channel axis.

Temperature readings taken on a mercury thermometer placed within the test cell but not in contact with the liquid metal were assumed to be the true temperatures of the liquid metal. These measured values were then used to determine the density, ρ, and electrical conductivity, σ, of the liquid metals. Variations of σ and ρ with temperature were taken from reference 30.

EXPERIMENTAL RESULTS AND COMPARISON WITH THEORY

Photographic sequences of the surface shape of the liquid metals are presented in this section for the experiments conducted in the investigation together with theoretically determined profiles for the corresponding boundary conditions at several selected instants of time. Since several nearly identical runs were made of each test setup, a decision as to which of these to publish was made on the basis of the uniformity of the motion of the piston or magnet, and the absence of metallic oxide on the walls and surface of the liquid metal. Numerical values for the theoretical surface height of the liquid metal at the instant the various photographs were taken were obtained by the method of characteristics for one space dimension and time discussed previously. Theoretical curves are presented for four to six photographs spaced a regular intervals. Roman numerals on the frames of the corresponding photographs (see, e.g., fig. 24(a) — numerals and time are noted in inset placed beside magnet pole piece) indicate the pictures so chosen. Time of exposure from a somewhat arbitrary starting time is given in seconds. The dimensionless time, τ, is given only for the theoretical curves.

In the computations, the electric field constant C was varied until a best fit to the experimental data was achieved. Comparison of the numerical results for several values of C with the experimental curves showed that it was possible to determine C within about ±3 percent. The optimum value so chosen was then used throughout a given sequence of surface profiles. All other parameters used in the numerical work were taken directly from the experimental data. Experimental readings from the photographs for the surface height were taken as the points at which the diagonal gridwork in the background either disappeared or made a sharp bend as it is reflected in the liquid metal surface.

Compression Wave Impinging on a Magnetic Field

The experimental setup shown in figure 1 illustrates the equipment layout for this series of tests. Runs were made with mercury and with NaK at several different piston speeds both with and without a 1/4-inch copper plate in the bottom of the channel. Surface shape profiles observed in several selected runs are reproduced in figures 23, 24, 25, and 26 together with the profiles predicted by the one-dimensional unsteady method of characteristics.

The interaction shown in figure 23 for mercury in an insulated channel is so weak that a numerical counterpart is not presented. This result is suggested in figure 17(d) by the low (~0.03) value predicted for the ratio $J_y/\sigma u B_0$. In other words, a negligible fraction of the theoretical one-dimensional or short circuited electric current actually flows because of the presence of the insulating walls. It is to be noted, however, that the roughness of the surface of the mercury behind the wave is eliminated by the magnetic field so that it is operative at least as a turbulence suppressor. Conversion of the leading edge of the compression wave into a solitary wave (see ref. 5) also seems to be caused by the magnetic field.

Considerable attenuation of the wave in mercury occurs as it passes through the magnetic field if the 1/4-inch copper plate is placed in the bottom of the channel as shown in figure 24. In the theoretical analysis, a step function is assumed for the leading edge of the wave. The strong wave relations were used to evaluate the change in the flow variables from one side of the jump to the other. In practice, surface tension and viscosity of the fluid round off the corners. As expected, at other locations on the surface good agreement exists between the observed and theoretical surface heights throughout the duration of the event. The value of the electric field constant C which best fits the data is below the value of 0.96 estimated earlier probably because some voltage drop occurs at the interface of the mercury and copper.

Results shown for NaK in figures 25 and 26 provide a more severe test of the one-dimensional theory because of the stronger interaction. An improper start of the piston causes undesirable extraneous waves to be generated. Several of these are quite noticeable in figures 25(a) and 26(a) between the piston and strong wave front. Agreement between theory and experiment is satisfactory in figure 26(b) for the wave moving over a copper bottom. The anticipated differences between the theoretical and experimental curves shown in figure 25(b) bear out in a rough fashion the current path patterns and increased effectiveness to be expected at

the edges of the magnetic field as shown in figures 15(d) and 17. The greater slope of the surface at the edges of the magnetic field results from the larger current density there (see fig. 15(d)). Variations in the surface height across the channel were visually noted during these runs to consist of a depression in the center of the channel of, at most, about 1/8 inch in the region where the surface slope was the greatest. This results from a greater effectiveness of the magnetic field near the center than at the walls brought about by the fact that the transverse electric currents flow more easily there than near the walls. (See fig. 15(d).)

A comparison of the data presented here with the material in references 31 to 34 is not made because of the differences in the experimental arrangements and boundary conditions. Qualitatively, the test results are the same in that shock waves were driven against or through a magnetic field, and in some cases reflection and attenuation of the incident wave are observed.

Centered Expansion in a Magnetic Field

The experimental arrangement in use here is the same as that for the compression wave tests (fig. 1) but it differs from those tests in that the piston motion is reversed. For comparison purposes, a run with mercury (fig. 27) was conducted without a magnetic field acting on the centered expansion. Although a magnetic field was present when the run shown in figure 28 was made, the fluid motion is not measurably altered by it. This is again as would be anticipated from the low values of C predicted in figures 15 through 17. Computations shown in both figures 27(b) and 28(b) were carried out for $C = 0$. Differences there are attributable to the initial motion of the piston. In the theory, it is assumed that the piston begins moving at $t = 0$ at a uniform speed, u_p. Such is not the case in practice, however, because there is slack in the piston linkage. If the exact motion of the piston during this time were known and inserted into the computations, it is felt that the two results would agree quite closely, since the centered expansion seems to depend strongly on the early motion of the piston.

When a copper plate is placed in the bottom of the channel, the magnetic field is once again effective (see fig. 29). As with the insulated bottom case, the starting motion of the piston is not well represented in the theory. This initial difference is nearly erased by the damping effect of the magnetic field so that good quantitative agreement exists during the later stages of the event (see fig. 29(b)).

The influence of the magnetic field on NaK is so strong (figs. 30 and 31) that the fluid literally creeps along the channel as the piston recedes whether or not the channel has a copper bottom. Differences between the theoretical and experimental curves for the insulated bottom case indicate the reduced resistance experienced by the current loops when they are near the edge of a magnetic field rather than near its center as suggested in figure 15(d). Computations are presented in figure 30(b) for three values of C in order to bring out the difference between the theory and experiment, thereby indicating that the one-dimensional approximation is inadequate here.

Since the interaction of the NaK with the magnetic field is very strong when the channel has a copper bottom, the fluid in front of the moving piston squirts around, up and over the piston thereby coating the channel walls with oxide. Therefore, only one photograph of the fluid motion is presented (fig. 31(a)) and the surface is indicated by the white line drawn there. As nearly as could be determined, the data are approximated by the profiles shown in figure 31(b).

Magnet Moving Over Fluid Surface

Figure 2 illustrates the general setup and camera position for the moving magnet experiments. As the magnet moves over the channel, it is observed that the flow of the liquid metal through the magnetic field approaches the character of a uniform traveling wave. In other words, the liquid metal profiles are more stationary for these tests than for the piston experiments. Phenomena that were not apparent in the liquid metal profile shapes in the compression wave and centered expansion experiments are now noticeable. The first of these is the lateral motion of the liquid metal brought about by the forces indicated in figure 17(b). Liquid metal is drawn to the center of the channel by the body forces on entering the magnetic field so that a hump forms in the surface. The elevation of the top of the hump is about the same magnitude as the depression observed visually when the run shown in figure 25(a) was made (i.e., 1/8 in.). Profiles of NaK in a channel with insulating walls are shown in figure 32(a). A comparison with the one-dimensional theory in figure 32(b) indicates that it expresses the fluid motion adequately outside the magnetic field region where there are no lateral forces. The compression wave that develops ahead of the magnet eventually becomes a discontinuity and propagates as such. In the numerical work, however, this wave is always treated as a weak wave.

From figure 33(a) it is observed that no net motion is imparted to the liquid metal when a 1/4-inch copper plate is placed on the bottom of the channel. The fluid is simply drawn toward the channel center line as it enters the magnetic field and then thrown outward against the channel walls as it exits from the magnetic field. A motion in the x direction is not detectable. Since the copper plate is stationary relative to the channel and moving relative to the magnet, an emf is now induced within it. The liquid metal can then serve as a possible circuit for the electric field induced in the copper. When the NaK is also stationary, the emf induced by the moving magnet in both metals is the same and no lateral electric currents flow. If the NaK moves, the emf induced in it will be smaller than in the copper, thereby permitting lateral currents to flow that force the NaK to stop. Stable motion therefore exists when the copper plate and liquid metal are both fixed relative to each other and, in the present situation, fixed relative to the laboratory frame of reference. Longitudinal currents do not share the same restraints because they arise as a consequence of being part of the return current loops. Lateral motion of the NaK relative to the copper does not then influence the amount of emf applied to a particular fluid element. Then the longitudinal currents can and do cause surface shape changes that are noticeable. Surface profiles to be anticipated for the copper bottom case, if the fluid motion were one-dimensional and C the same as for the insulating bottom case, are shown in figure 33(b).

26

Interaction of the moving magnet with mercury (fig. 34) is much less spectacular but qualitatively the same as that for NaK. A mirrorlike surface, that is quite easy to maintain with mercury in a nitrogen atmosphere, makes it possible to observe wave patterns behind the moving magnet. Diagonal gridwork placed behind the channel and reflected in the mercury surface then brings out the surface height variations. Figure 35 presents results for several magnet speeds. Lateral forces are once again responsible for the liquid metal being first drawn toward the center of the channel and then thrown outward against the channel sides. As the magnet speed increases from below to above a Froude number $(u_m/\sqrt{gh_0})$ of 1, the disturbance wave pattern changes from alternating depressions (or vortex street type, fig. 36(a)) to a Mach wave type pattern (fig. 36(b)). Variations in the wave angle with increase in speed of the magnet are small (fig. 37). Most apparent[5] is an elongation of the center collision area of the waves, indicating an increase in the thickness of the waves. A second set of waves is noted in the highest speed run to emanate from under the magnet in the region where the incoming fluid collides as it is drawn to the center of the channel by the magnet.

The mechanism demonstrated in figures 32 and 35 suggests a device that would perhaps serve as a nozzle capable of converting an ionized high-density subsonic flow of gas into a low-density supersonic stream. Such a device would consist simply of a transverse magnetic field impressed across a channel with insulating walls. Flow deflections usually brought about by convergent-divergent walls are now carried out by body forces that result from current loops induced by relative motion of the magnet and stream. Variations in the downstream Mach number are made by changing the magnetic field strength. Such a magnetogasdynamic nozzle is operative at low and probably also at high magnetic Reynolds numbers. It also has the advantage that heat is added to rather than subtracted from the gas as it passes through the nozzle region.

Nonsteady Magnetic Field - NaK

When the magnet is energized, the liquid metal within the air gap is drawn into a hill at the center of the container as illustrated in figures 3(a) and 3(b). The magnitude of the disturbance depends on the magnetic parameter P_{mo} in such a way as to produce an easily measurable (about 1 cm) disturbance in NaK and a barely detectable one in mercury. Visually it is possible to see a slight (~0.01 in.) rise in the mercury at the center of the vessel. Also apparent is a frosted or dull appearance taken on by the mirrorlike surface during (about 1 sec) the time that the magnetic field builds up. A more intense (>5000 gauss) or a more rapidly changing field would of course produce a larger disturbance.

Figure 38 presents photographic sequences of the surface profiles of NaK in the two-dimensional channel shown in figure 3(a). The time history of the surface shapes is about the same whether the bottom is an insulator or copper plate. A small difference lies in the slight inward motion induced at the ends of the magnet when the channel has walls that are insulators. The different coloration on

---

[5]In these experiments, the magnet had to be rolled by hand to eliminate all possible vibrations that would cause extraneous waves.

the side walls for the two runs is due to a sizable amount of oxide on the walls shown in figure 38(a) and practically none for figure 38(b). The sharper curvature of the surface there and the hump in the NaK at the center of the magnet reflect this motion. A prediction of the surface shape can be made with the theory set up for nonsteady magnetic fields in two dimensions (see eq. (28)). A comparison of the surface height measured at the center of the magnetic field for the data shown in figure 38(b) and predicted by the two-dimensional theory is made in figure 39(a). The theoretical shape of the surface in a plane perpendicular to the channel axis is shown in figure 39(b) at several instants of time. No measurements were made of the surface shape in this plane because of the experimental difficulties involved. Differences between the two results illustrated in figure 39(a) are greater than the reading error in the experimental surface height. Considerable uncertainty exists, however, in the experimental values of the inductance L and resistance R of the magnetic circuits. Values that only approximate the true experimental conditions are used in the theory because the precise values for each test were not adequately measured at that time. Also, resistance heating of the magnet coils can cause the magnitude of R to vary over as much as 50 percent of its room temperature value. It is felt that these are the reasons more precise agreement between the theory and data was not achieved in any of the nonsteady magnetic field tests.

Maximum surface heights that occur during the time the magnet is energized as estimated by the two-dimensional theory are shown in figure 40 for a range of the parameters concerned. The time history of the current through the magnet windings that was assumed for these computations is presented in figure 41. Neither of the curves in figure 41 has the peculiar shape exhibited by the 14.4 ampere run (fig. 19), but the function represented by two terms for the induction is a fair approximation to the runs at lower maximum currents.

An extensive series of tests was made with the axially symmetric arrangement shown in figure 3(b). Runs were made at nominal maximum currents of 5, 10, and 15 amperes through the magnet coils with and without a copper plate in the bottom of the 2-1/2-inch-diameter test cell. Typical data for three values of the magnetic parameter, P_{mo}, are shown in figures 42 through 45 together with the theoretically predicted surface shapes. No measurable difference was observed between the copper and insulating bottom runs when all other test conditions for the two were the same. Quantitative agreement of the axially symmetric theory with the test data is once again hindered by a lack of information on the exact values of the parameters R, L_O, L_1, . . . for each of the tests. Qualitative agreement is very good. It is felt that if the experimental parameters were measured more accurately and these numerical values used as input for the theory, quite good quantitative agreement could be achieved. Since considerable time and effort would be required to do this and because the agreement is already fairly good, these further refinements were not made.

CONCLUDING REMARKS

Theoretical results presented in this paper demonstrate some of the characteristics of the analogy between waves on the surface of a liquid metal and pressure waves in an ionized gas. A comparison of theoretical results (fig. 8) for each medium under the same boundary conditions shows that density and velocity (in dimensionless form) of the gas are represented quite accurately by the surface height and velocity of the free surface of a liquid metal. As was true for water waves the analogy does not apply to strong waves. Since joule heating does not significantly affect the liquid metal, the analogy becomes less exact as the amount of electrical heating increases. Density and velocity are duplicated roughly for a gas that has a ratio of specific heats, γ, of about 2, and only in a qualitative way for other values of γ. It is to be remembered that the analogy represents only certain aspects of the flow of ionized gases. Probably foremost is its lack of duplication of the chemical reactions and the associated variations in the electrical properties of the gas.

Experiments carried out with mercury and NaK (figs. 23 - 45) make it possible to:

a. Ascertain the ability of the theory to predict the motion of the liquid metal in electric and magnetic fields.

b. Study wave motion in the presence of transverse magnetic fields with various boundary conditions on the electric currents.

c. Attain a substantial range of the magnetic parameters.

A perusal of the theoretical and experimental data presented here shows that:

1. The wave motion in the channels can be approximated by a one-dimensional theory, even though the electric field is three dimensional, if the largest portion of the electric current in the fluid is made nearly one-dimensional by providing a suitable external circuit by which the currents can close on themselves.

2. The use of the electric field constant C in the one-dimensional tests for treating the electric field (or resistance of the return circuit) simplifies the analysis greatly without a sacrifice of accuracy if the conditions in 1 are met.

3. When an external circuit is not provided for the return of the electric currents, they form paths that extend upstream and downstream of the moving elements and magnet in such a way that sizable lateral forces can result. The surface shape and flow field then no longer approach a one-dimensional character.

4. The lateral forces and the corresponding surface distortions that arise from the longitudinal portion of the electric current paths suggest a new device for a magnetogasdynamic nozzle. Such a nozzle would change a high-density low-speed stream into a low-density supersonic flow. This discovery would be difficult to make without the use of the free-surface analogy.

5. As expected, the free-surface waves do make it possible to visualize and study flow phenomena characterized by a low magnetic Reynolds number that are otherwise quite intractable.

Ames Research Center
    National Aeronautics and Space Administration
        Moffett Field, Calif., Aug. 24, 1962

APPENDIX

SYMBOLS

a   speed of propagation of a small wave

A $\dfrac{a}{a_O}$ or $\sqrt{\dfrac{h}{h_O}}$

B   magnetic field strength

$\mathbb{B}$ dimensionless magnetic field, $\dfrac{B_z}{B_O}$

C   electric field constant (See eq. (18).)

d   half width or radius of channel

D   half length of doublet distribution (See fig. 11.)

e   internal energy of fluid element

E   electric field intensity

$\mathbb{E}$ $\dfrac{E}{a_O B_O}$

F   force

g   acceleration of gravity

G   gravity force field

h   local depth of liquid metal

H $\dfrac{h}{h_O}$

Ha   Hartmann number, $\sqrt{\dfrac{\sigma}{\eta}}\, B_O d$

i $\sqrt{-1}$

J   electric current density

K   curvature of free surface

L   half width of doublet distribution (See fig. 11.)

$\mathbf{L}$ inductance of magnet

NaK	eutectic mixture of sodium (22 percent) and potassium (78 percent)
p	pressure
P	characteristic parameter, $U + 2\sqrt{H}$ or $U + \dfrac{2A}{\gamma - 1}$
P_m	magnetic parameter, $\dfrac{\sigma B_z^2 d}{\rho a_o}$
P_{mo}	$\dfrac{\sigma B_o^2 d}{\rho a_o}$, maximum value of magnetic parameter in flow field used as representative value
Q	characteristic parameter, $U - 2\sqrt{H}$ or $U - \dfrac{2A}{\gamma - 1}$
R	electrical resistance
R_m	magnetic Reynolds number, $\sigma \mu a_o d$
Re	viscous Reynolds number, $\dfrac{\rho a_o d}{\eta}$
t	time
T	temperature
u, v, w	velocity of fluid in x, y, and z directions, respectively
U	$\dfrac{u}{a_o}$
V	$\dfrac{v}{a_o}$
x, y, z	coordinate axes, x alined with channel axis and z vertical
X, Y, Z	$\dfrac{x}{d}$, $\dfrac{y}{d}$, $\dfrac{z}{d}$
γ	ratio of specific heats, $\dfrac{c_p}{c_v}$
ϵ	electric permittivity
η	viscosity of fluid
λ	length of wave on free surface

32

μ	magnetic permeability
δ	ratio of fluid depth to wavelength
ν	kinematic viscosity, $\dfrac{\eta}{\rho}$
ρ	density of fluid
σ	electrical conductivity
τ	$\dfrac{a_0 t}{d}$
φ	electric current potential function
Φ	complex potential function, $\varphi + i\psi$
ψ	electric current stream function
ζ	$x + iy$
$()_0$	reference quantity
$()_w$	values immediately behind strong wave
$()_s$	doublet layer or slab
$()_{0,1,2,\cdots}$	quantities ordered in δ used to derive free-surface equations
$()_m$	magnet
$()_p$	piston

REFERENCES

1. Stoker, J. J.: Water Waves - The Mathematical Theory with Applications. Interscience Publishers, Inc., 1957.

2. Ippen, A. T., and Harleman, D. R. F.: Studies on the Validity of the Hydraulic Analogy to Supersonic Flow. A. F. Tech. Rep. No. 5985, Parts I and II, May 1950.

3. Ippen, A. T., and Harleman, D. R. F.: Studies on the Validity of the Hydraulic Analogy to Supersonic Flow. A. F. Tech. Rep. No. 5985, pt. III, Oct. 1950.

4. Harleman, Donald R. F., and Crossley, Harry E., Jr.: Studies on the Validity of the Hydraulic Analogy to Supersonic Flow. A. F. Tech. Rep. No. 5985, pt. 4, Feb. 1952.

5. Lamb, Horace: Hydrodynamics. Dover Publications, 1945.

6. Shapiro, Ascher H.: Free Surface Water Table. Art. H, 1, Vol. IX, Princeton Series on High Speed Aerodynamics and Jet Propulsion, Princeton University Press, 1954.

7. Cowley, M. D.: The Hydraulic Analogy to Simple Shock Tube Flow. A.E.R.E. X/R 2764, U.K.A.E.A. Research Group, 1958.

8. Gilmore, F. R., Plesset, M. S., and Crossley, H. E., Jr.: The Analogy Between Hydraulic Jumps in Liquids and Shock Waves in Gases. Jour. Appl. Physics, vol. 21, Mar. 1950, pp. 243-249.

9. Matthews, Clarence W.: The Design, Operation, and Uses of the Water Channel as an Instrument for the Investigation of Compressible-Flow Phenomena. NACA TN 2008, 1950.

10. Orlin, W. J., Lindner, N. J., and Bitterly, J. G.: Application of the Analogy Between Water Flow With a Free Surface and Two-Dimensional Compressible Gas Flow. NACA Rep. 875, 1947.

11. Preiswerk, E.: Application of the Methods of Gas Dynamics to Water Flows With Free Surface. Part II. Flows With Momentum Discontinuities. Institut fur Aerodynamik Eidgenossische, Technische Hochschule, Zurich. NACA TM 935, 1940

12. Fraenkel, L. E.: A Shallow-Liquid Theory in Magnetohydrodynamics. OSR Tech. Note 59-563, June 1959.

13. Alpher, R. A., Hurwitz, H., Jr., Johnson, R. H., and White, D. R.: Some Studies of Free-Surface Mercury Magnetohydrodynamics. Reviews of Modern Physics, vol. 32, no. 4, Oct. 1960, pp. 758-769.

14. Alpher, R. A.: Experiments in Magneto-Fluid-Dynamics. Physics Today, vol. 13, no. 12, Dec. 1960, pp. 26-31.

15. Donaldson, Coleman duP.: The Magnetohydrodynamics of a Layer of Fluid Having a Free Surface. 1959 Heat Transfer and Fluid Mechanics Institute, University of California, Los Angeles, California, June 11-13, 1959, pp. 55-67.

16. Fraenkel, L. E.: On the Magnetohydrodynamics of Asymmetric Surface Waves in a Dish of Shallow Conducting Liquid. Quart. Jour. Mech. and Appl. Math., vol. XIV, pt. 2, May 1961, pp. 173-195.

17. Lundquist, Stig: Studies in Magneto-hydrodynamics. Arkiv for Fysik, Band 5, nr. 15, Aprl. 1952, pp. 297-347.

18. Shirokov, M. F.: Interaction Between Gravitational-Capillary and Magneto-hydrodynamic Waves. Soviet Physics JETP, vol. 6, no. 1, Jan. 1958, pp. 50-54.

19. Colgate, Stirling A.: Liquid Sodium Instability Experiment. Magnetohydrodynamics, Rolf K. M. Landshoff, ed., Stanford University Press, 1958, pp. 104-108.

20. Colgate, S. A., Furth, H. P., and Halliday, F. O.: Hydromagnetic Equilibrium Experiments with Liquid and Solid Sodium. Reviews of Modern Physics, vol. 32, no. 4, Oct. 1960, pp. 744-747.

21. Lehnert, Bo: On the Behaviour of an Electrically Conductive Liquid in a Magnetic Field. Archiv For Fysik, vol. 5, no. 5, Mar. 1952, pp. 69-90.

22. Lehnert, Bo: Magneto-hydrodynamic Waves in Liquid Sodium. Physical Review, vol. 94, no. 4, May 15, 1954, pp. 815-824.

23. Lehnert, B., and Sjogren, G.: Stability of a Hollow Mercury Jet. Reviews of Modern Physics, vol. 32, no. 4, Oct. 1960, pp. 813-814.

24. Lehnert, B.: An Instability of Laminar Flow of Mercury Caused by an External Magnetic Field. Proc. Roy. Soc. of London, ser. A, vol. 233, no. 1194, Dec. 29, 1955, pp. 299-302.

25. Stewartson, K.: Magneto-hydrodynamics of a Finite Rotating Disk. Quart. Jour. Mech. and Appl. Math., vol. X, pt. 2, May 1957, pp. 137-147.

26. Lundquist, S.: Experimental Investigations of Magneto-Hydrodynamic Waves. Physical Review, vol. 76, no. 12, Dec. 15, 1949, pp. 1805-1809.

27. Hide, R.: Waves in a Heavy, Viscous, Incompressible, Electrically Conducting Fluid of Variable Density, in the Presence of a Magnetic Field. Proc. Roy. Soc. of London, ser. A, vol. 233, no. 1194, Dec. 29, 1955, pp. 376-396.

28. Post, Richard F.: Experimental Research on High-Temperature Plasmas. Symposium of Plasma Dynamics, Francis H. Clauser, ed., Addison-Wesley Publishing Company, Inc., 1960, pp. 1-18.

29. Dattner, A., Lehnert, B., and Lundquist, S.: Liquid Conductor Model of Instabilities in a Pinched Discharge. Proceedings of the Second United Nations International Conference on the Peaceful Uses of Atomic Energy. Geneva, Switz., 1-13 Sept. 1958. Vol. 31. Theoretical and Experimental Aspects of Controlled Nuclear Fusion, pp. 325-327.

30. Lyon, Richard N., ed.: Liquid-Metals Handbook. Second ed., NAVEXOS P-733 (Rev.), June 1952.

31. deLeeuw, J. H.: The Interaction of a Plane Strong Shock Wave With a Steady Magnetic Field. UTIA Rep. No. 49, Univ. of Toronto Inst. of Aerophysics, March 1958.

32. Atkinson, William R., Holden, William R., and Fowler, Richard G.: Shock Waves Reflected by Magnetic Fields. Jour. Appl. Physics, vol. 30, no. 6, June 1959, pp. 801-802.

33. Patrick, R. M., and Brogan, T. R.: One-Dimensional Flow of an Ionized Gas Through a Magnetic Field. Jour. Fluid Mech., vol. 5, pt. 2, Feb. 1959, pp. 289-309.

34. Barach, John Paul: Interaction between a Magnetic Field and an Electrically Produced Shock Wave. The Physics of Fluids, vol. 4, no. 12, Dec. 1961, pp. 1474-1477.

35. Courant, R., and Friedrichs, K. O.: Supersonic Flow and Shock Waves. Interscience Publishers, Inc., 1948.

36. Hartmann, Jul.: Hg-Dynamics I - Theory of the Laminar Flow of an Electrically Conductive Liquid in a Homogeneous Magnetic Field. Kgl. Danske Videnskabernes Selskab, Mathematisk-Fysiske Meddelelser, vol. 15, no. 6, Copenhagen, 1937.
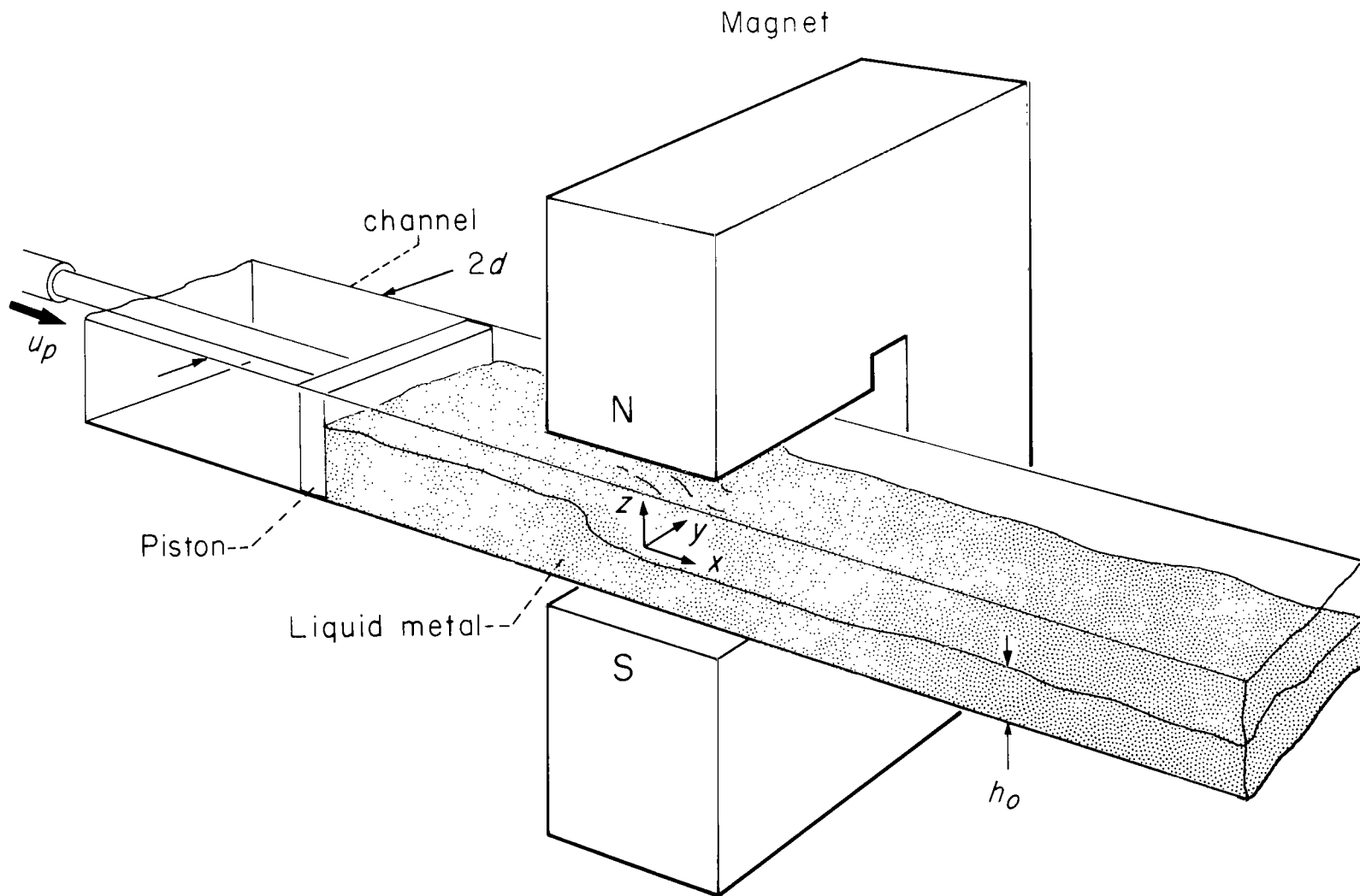
Figure 1.- Schematic diagram of arrangement used to study the interaction of one-dimensional waves with transverse magnetic fields
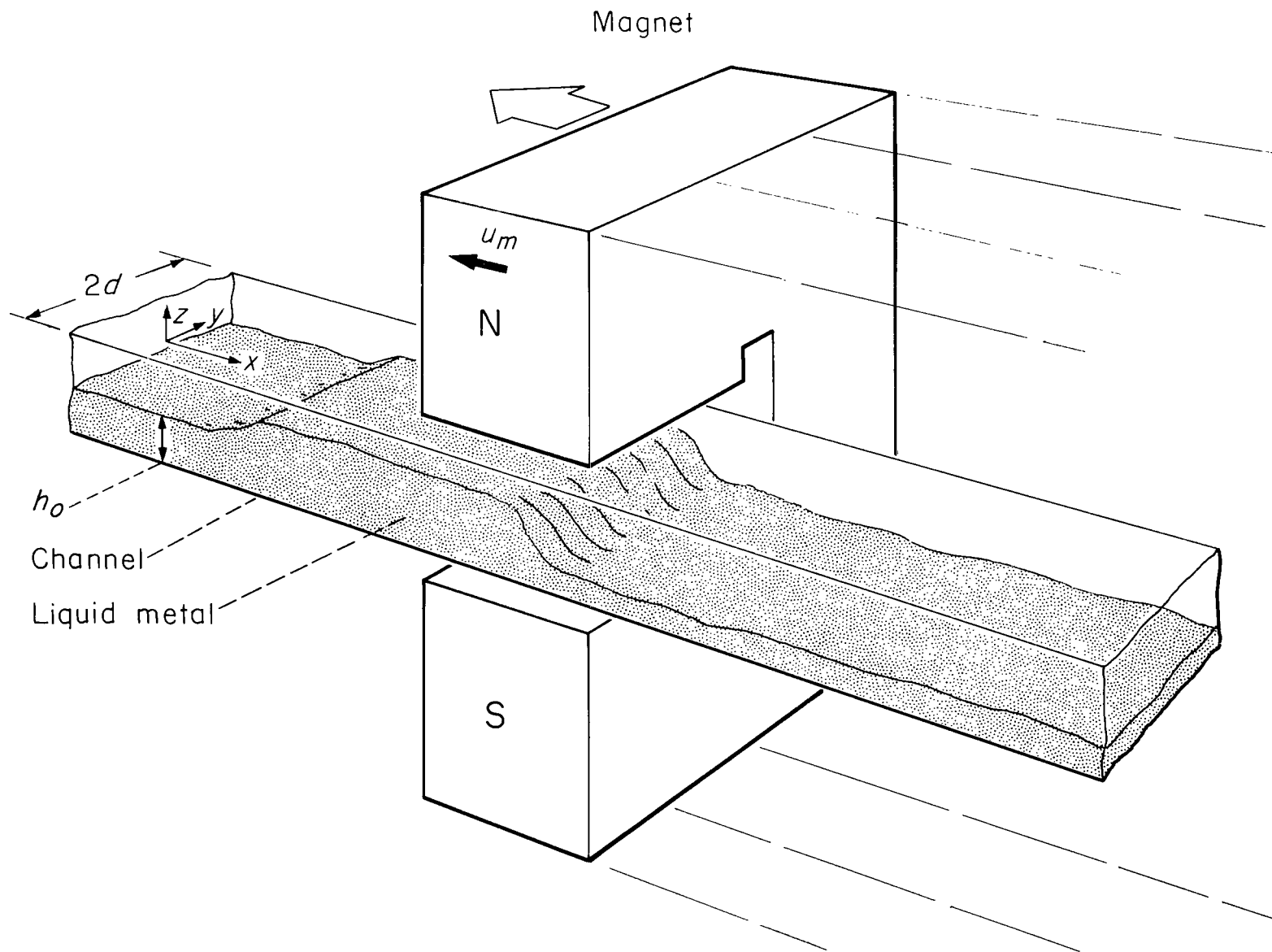
Figure 2.- Schematic diagram of moving-magnet configuration.
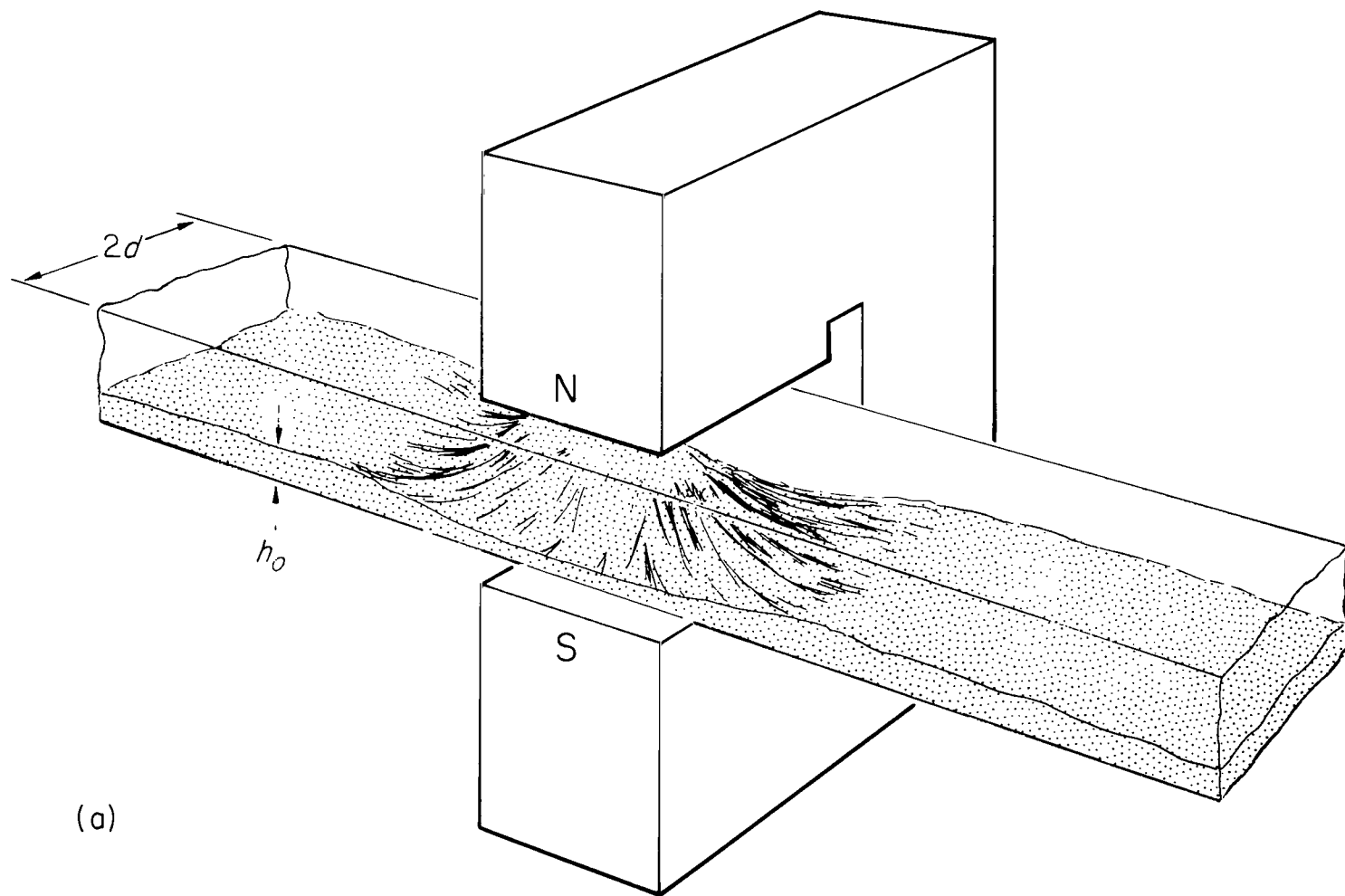
(a) Two-dimensional.

Figure 3.- Schematic diagram of nonsteady magnetic field model.

Test cell

(b)
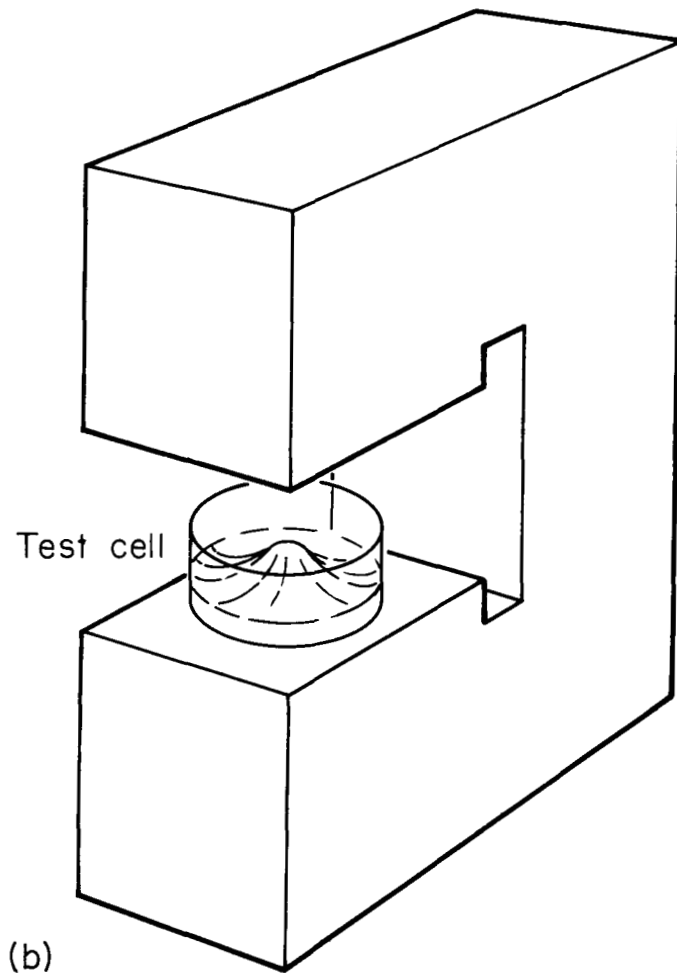
(b) Axially symmetric.

Figure 3.- Concluded.
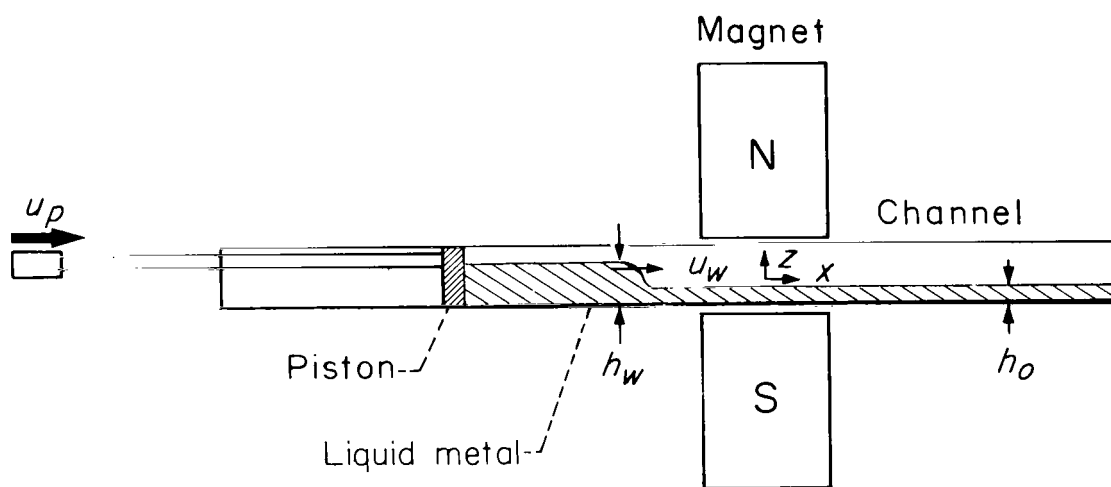
Figure 4.- Diagram illustrating notation used for waves of finite strength.
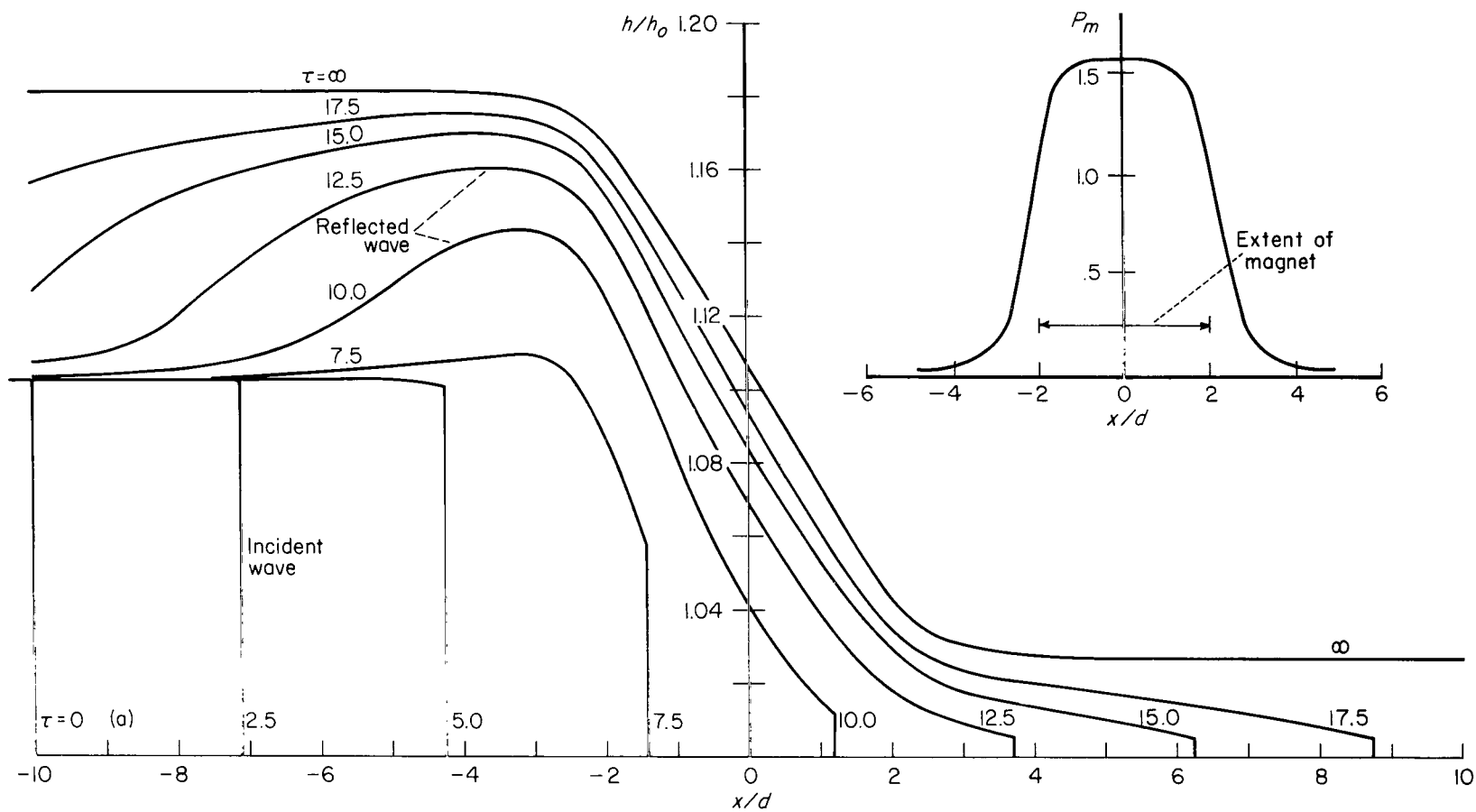
(a) Surface height.

Figure 5.- Interaction of a weak compression wave with transverse magnetic field; $P_{mo} = 1.55$, $U_p = 0.10$, $h_O = 0.37$ inch, $a_O = 1$ ft/sec.
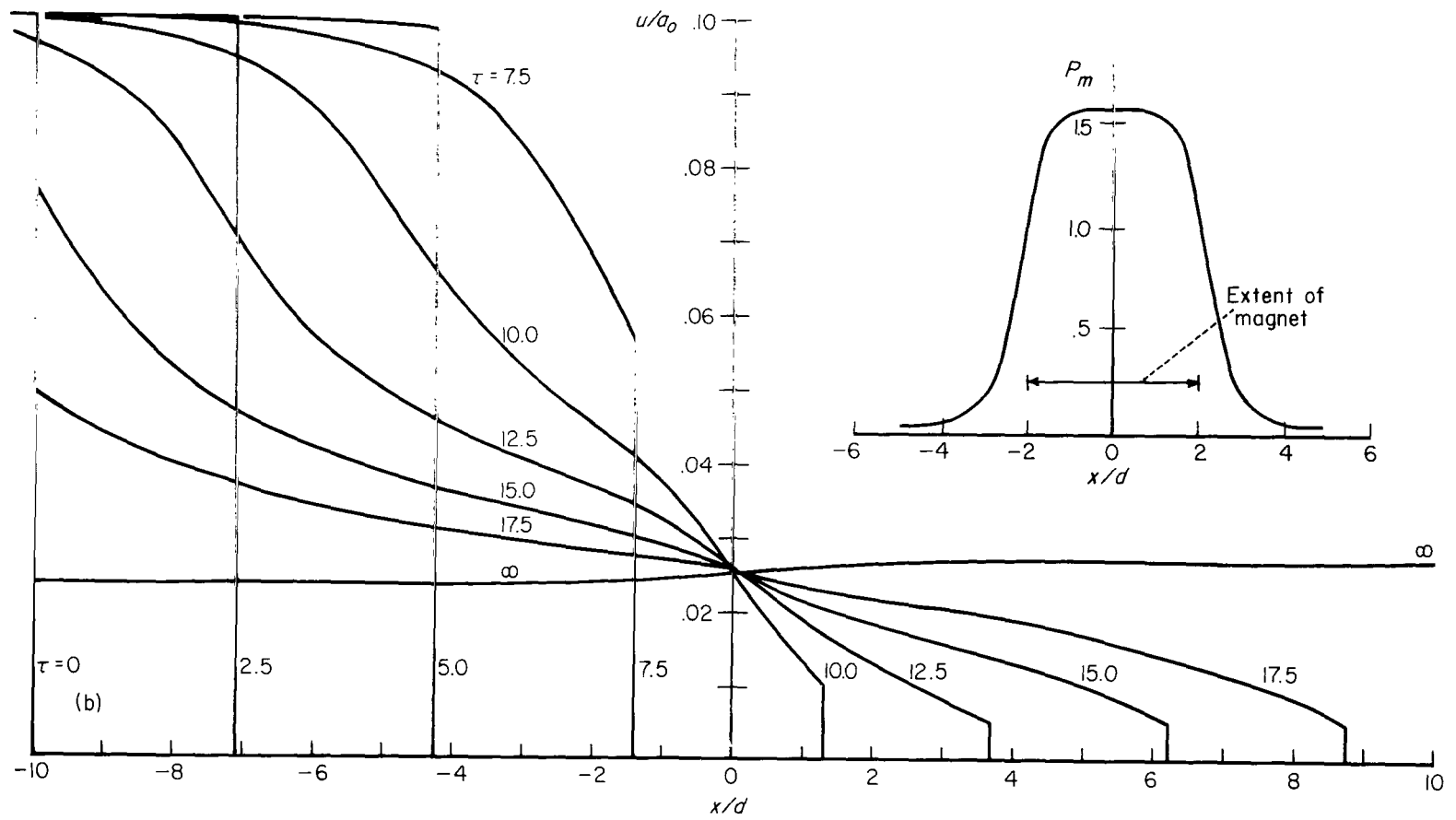
(b) Velocity of fluid.

Figure 5.- Concluded.
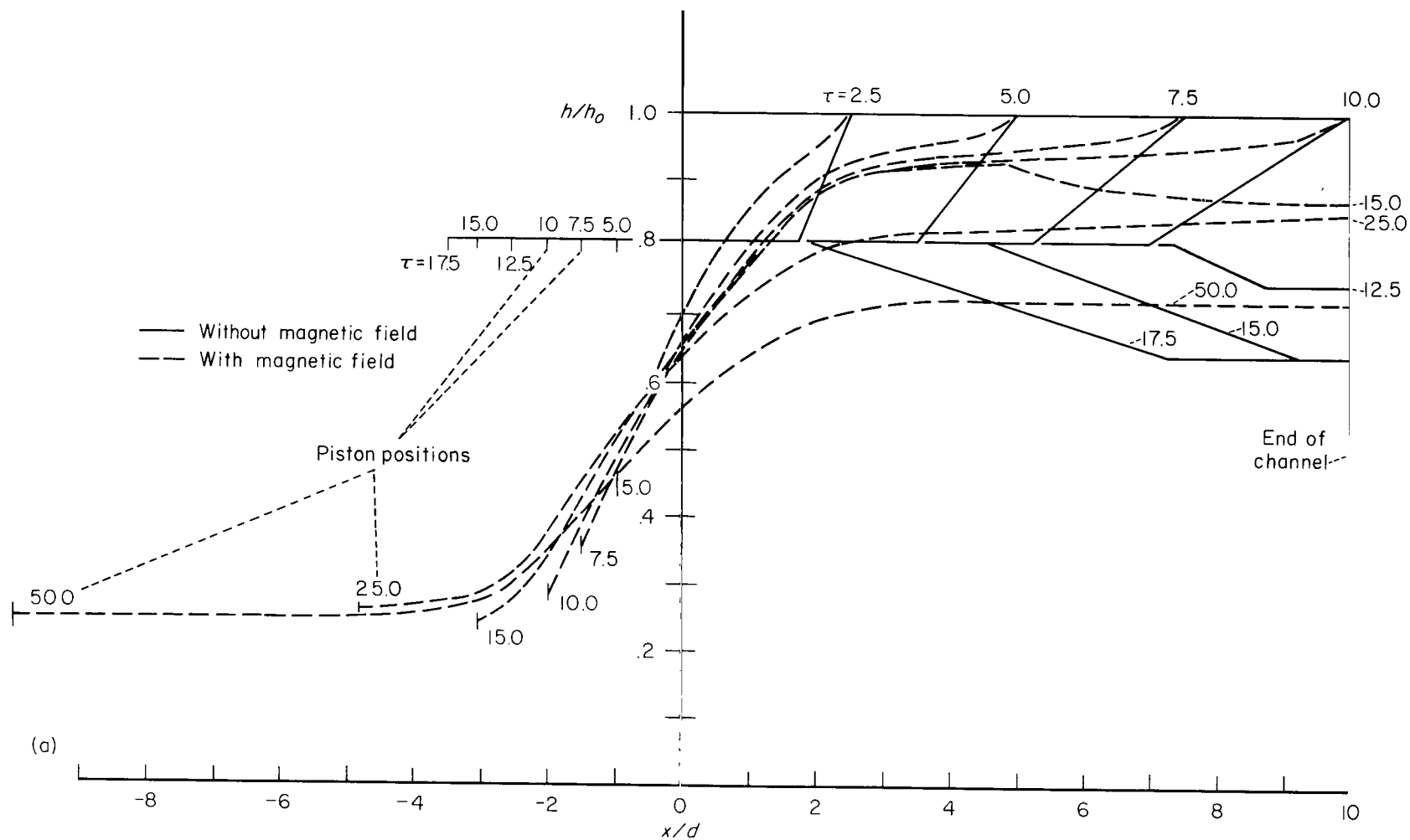
Figure 6.- Surface height of liquid metal as a centered expansion wave interacts with transverse magnetic field; $P_{mo} = 1.55$, $U_p = -0.20$, $h_o = 0.37$ inch, $a_o = 1$ ft/sec.
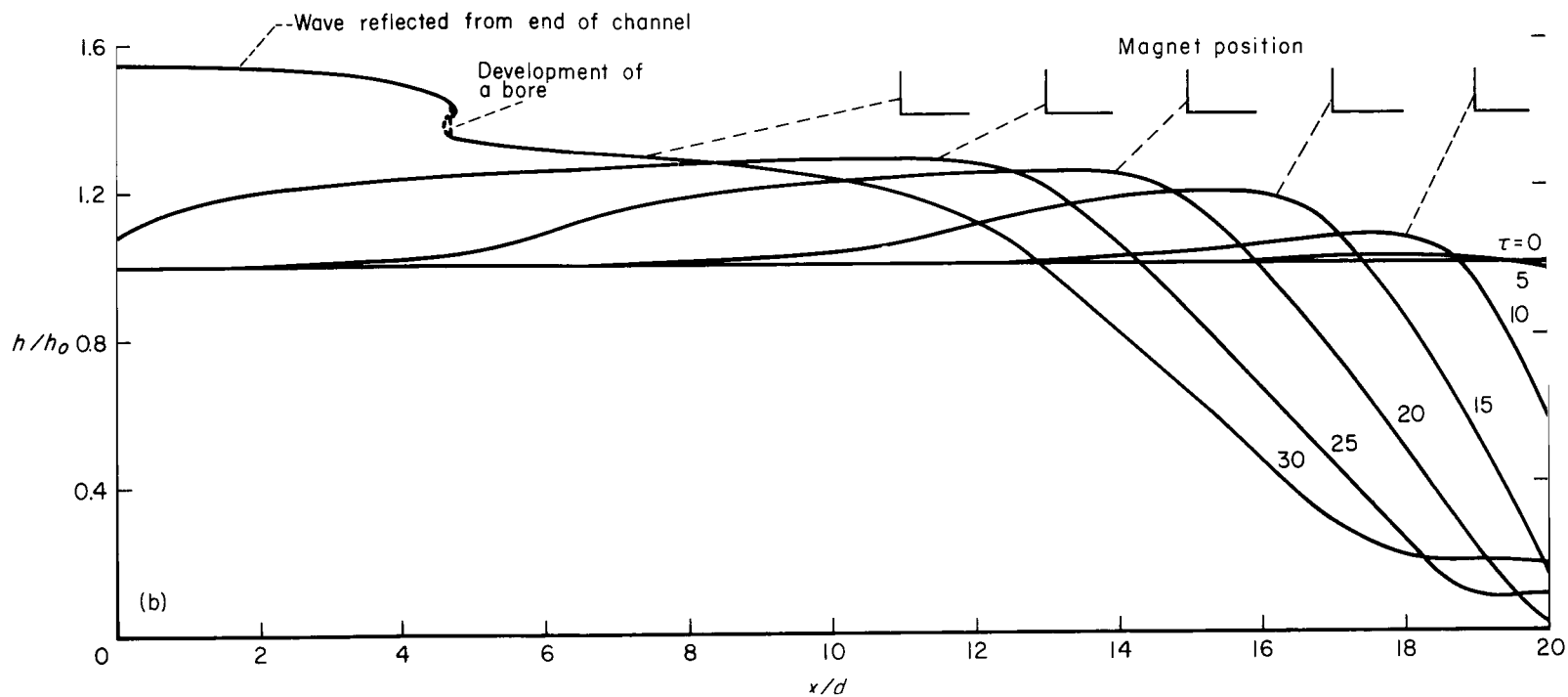
Figure 7.- Wave motion brought about in liquid metal by magnet moving past channel; $P_{mo} = 1.55$, $U_m = -0.40$, $h_O = 0.37$ inch, $a_O = 1$ ft/sec.
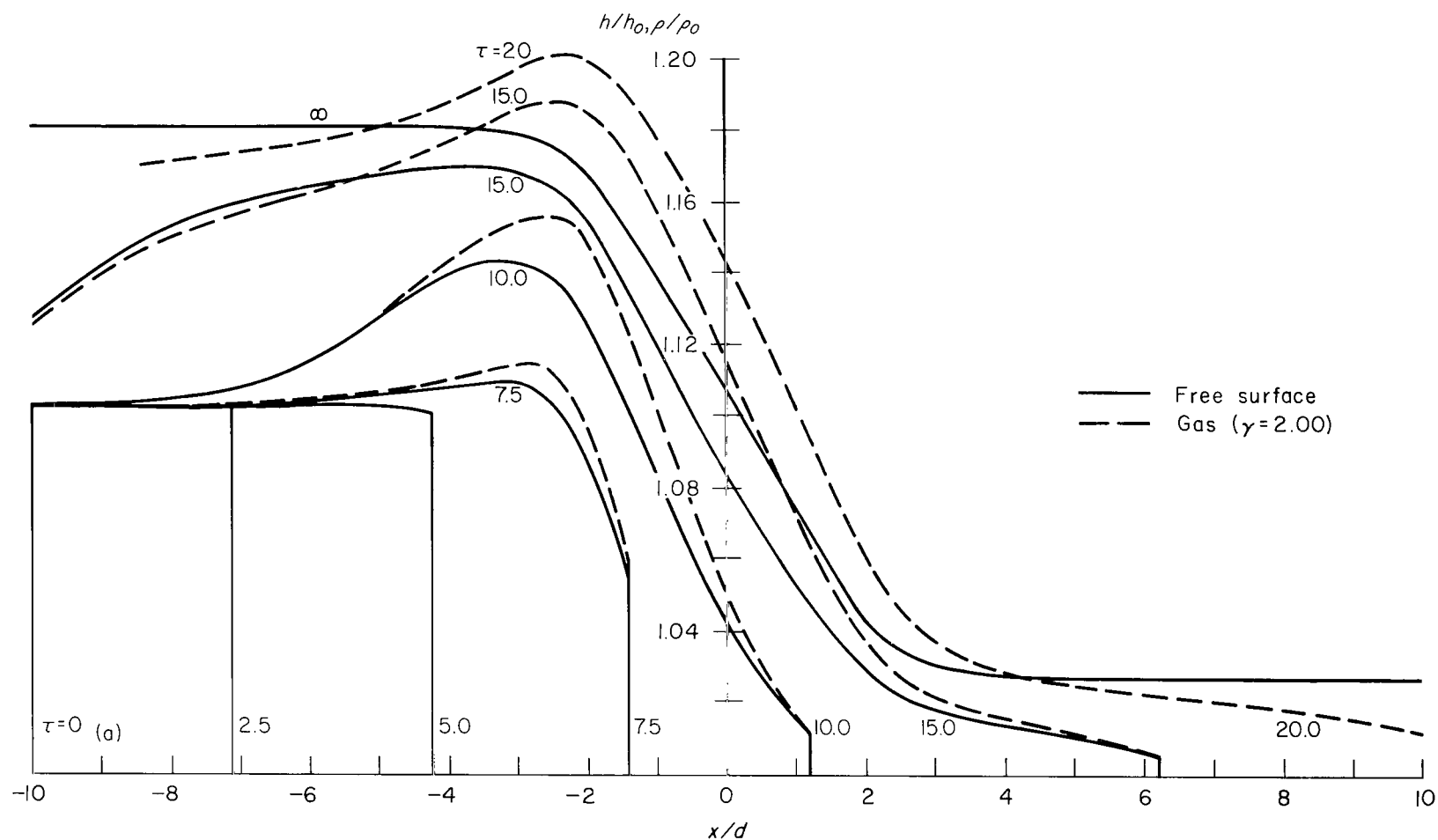
(a) Height of free surface and density of gas; $\gamma = 2$ $(\rho/\rho_0 = T/T_0 = \sqrt{p/p_0})$.

Figure 8.- Comparison of free-surface and gas-dynamic flow fields as computed by the method of characteristics; $P_m = 1.30$, $U_p = 0.1$.
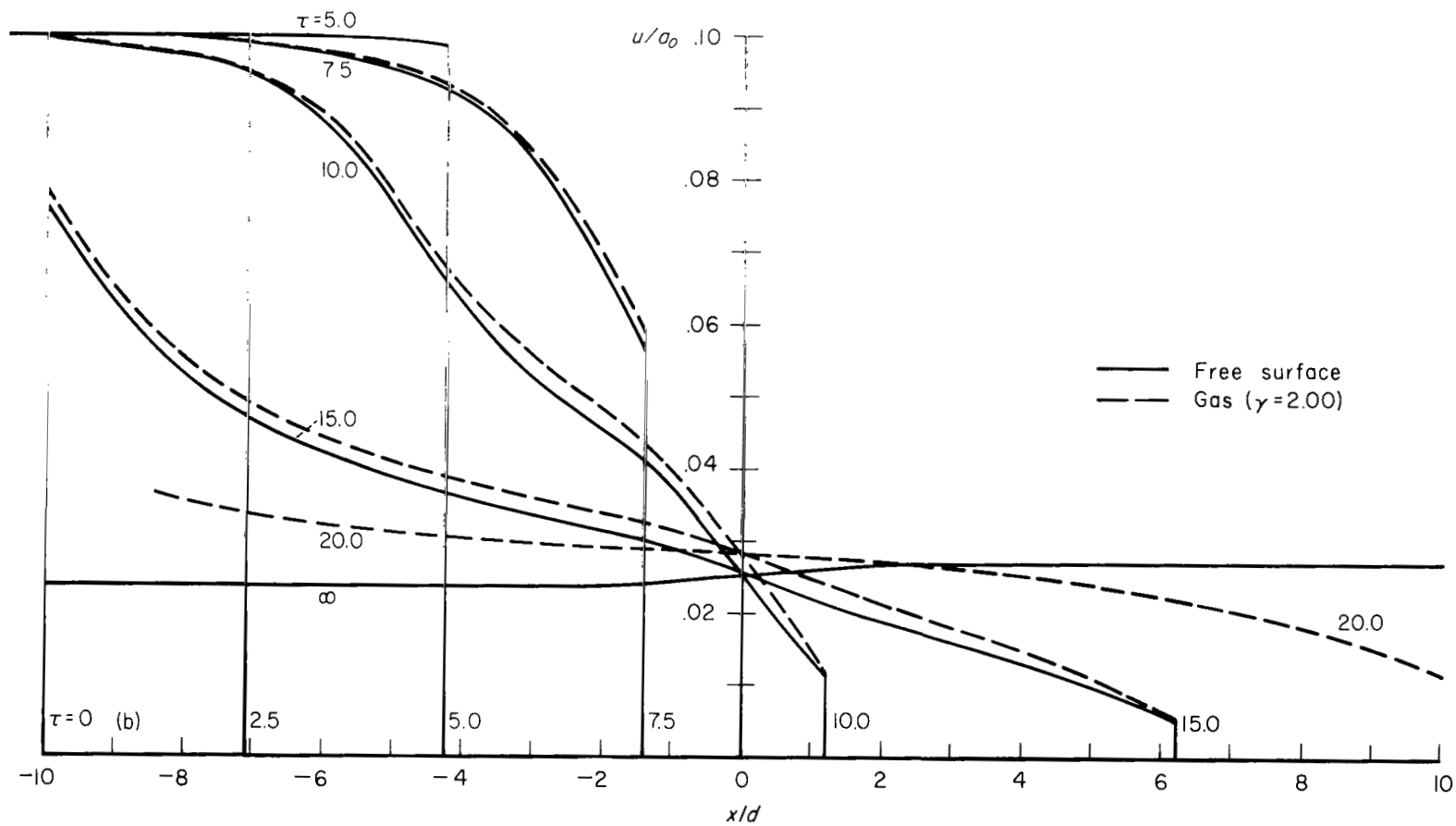
(b) Velocity of liquid metal and gas; $\gamma = 2$.

Figure 8.- Continued.
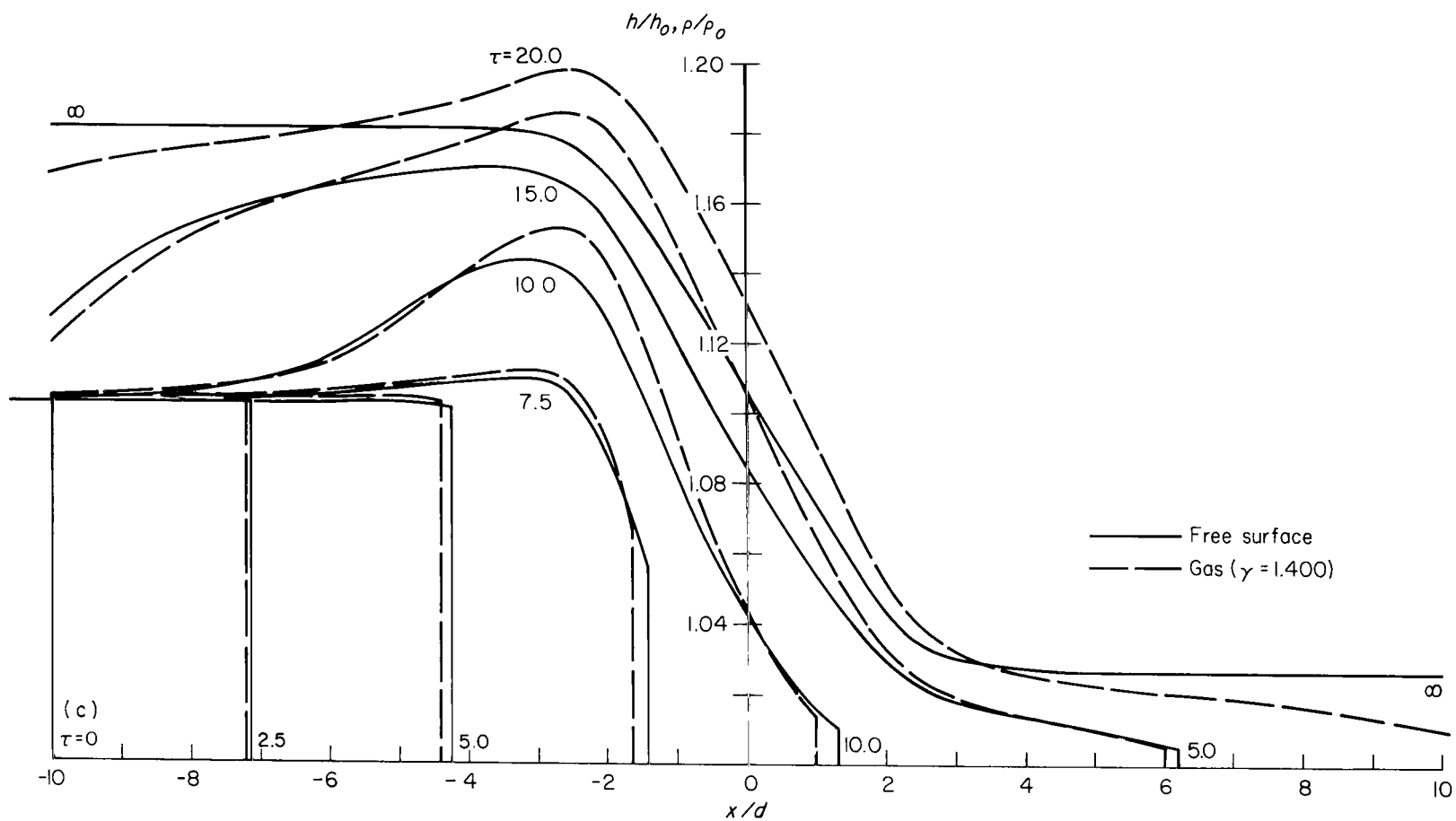
(c) Height of free surface and density of gas; $\gamma = 1.4$.

Figure 8.- Continued.
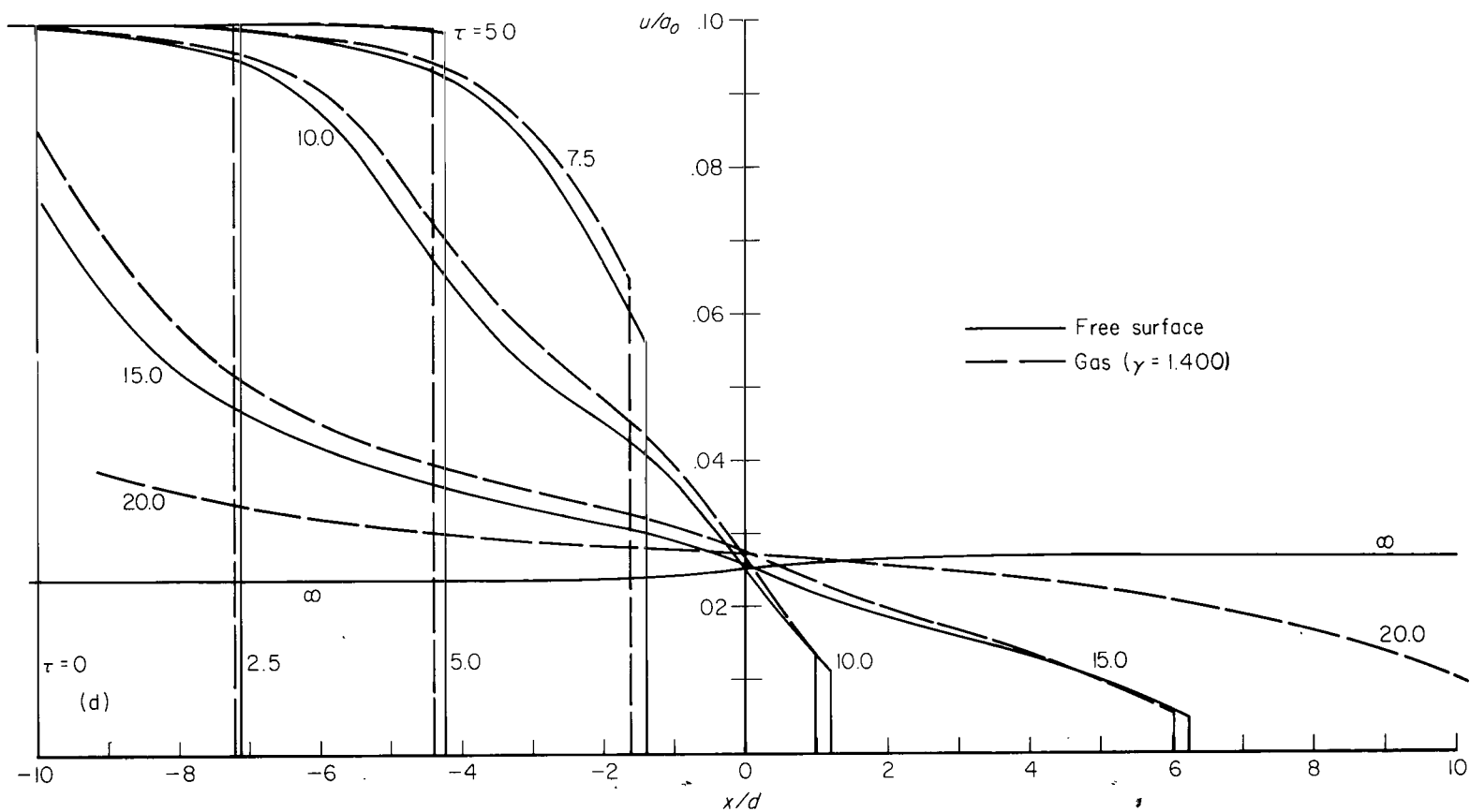
(d) Velocity of liquid metal and gas; $\gamma = 1.4$.

Figure 8.- Continued.

$h/h_0, p/p_0, T/T_0$

$\tau = \infty$

15.0

10.0

7.5

$\tau = 0$

Free surface
Gas pressure
Gas temperature $\Big\} \gamma = 1.40$

1.24

1.20

1.16

1.12

1.08

1.04

$\tau = 0$ (e)

5.0

10.0

∞

---15.0

20.0

-10   -8   -6   -4   -2   0   2   4   6   8   10

x/d
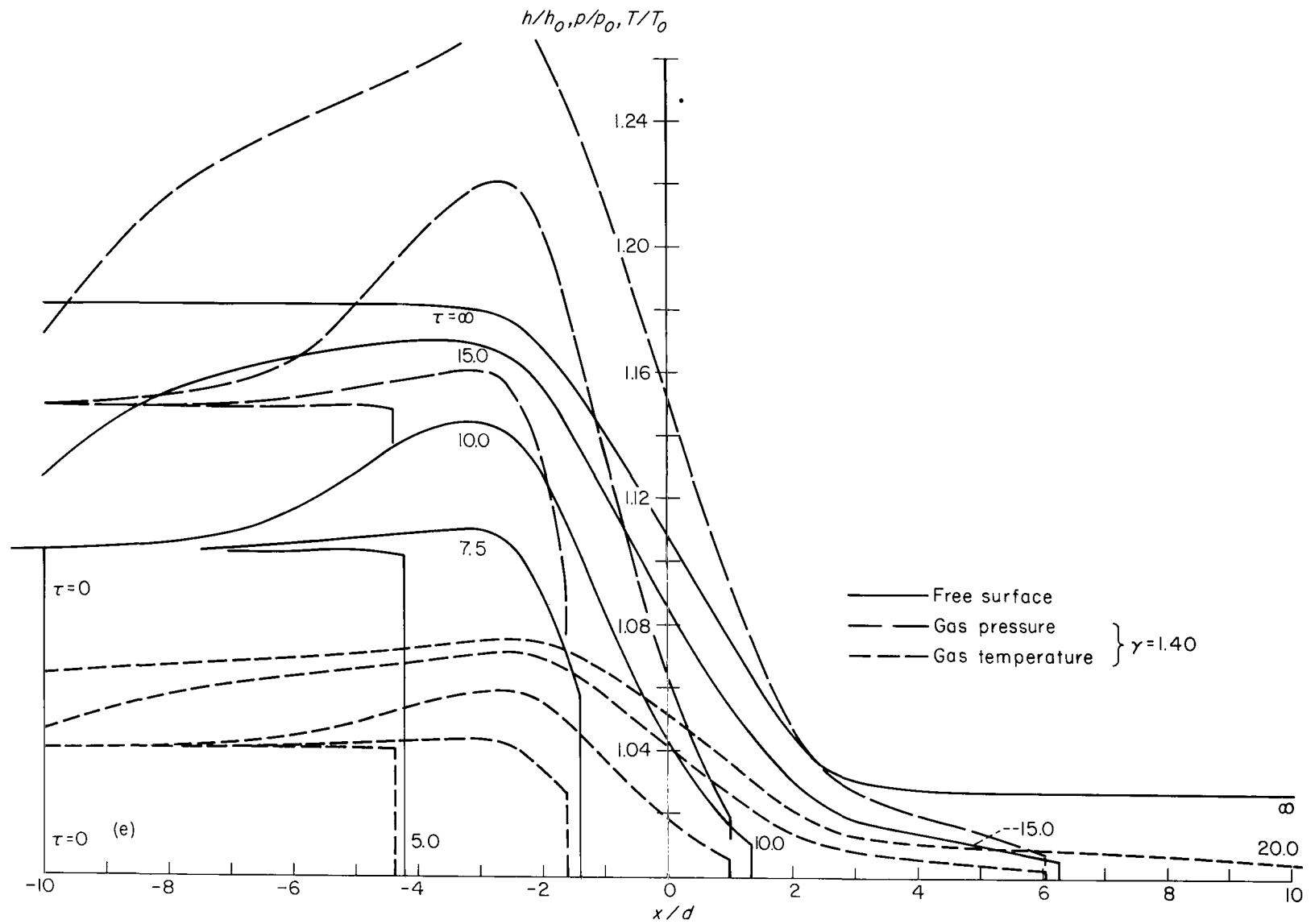
(e) Height of free surface and temperature and pressure of gas; $\gamma = 1.4.$

Figure 8.- Concluded.

Lucite Walls

Electric current loops

h

(a) δ = Boundary layer thickness $\approx h/Ha$

h_{cu}

(b)   Copper
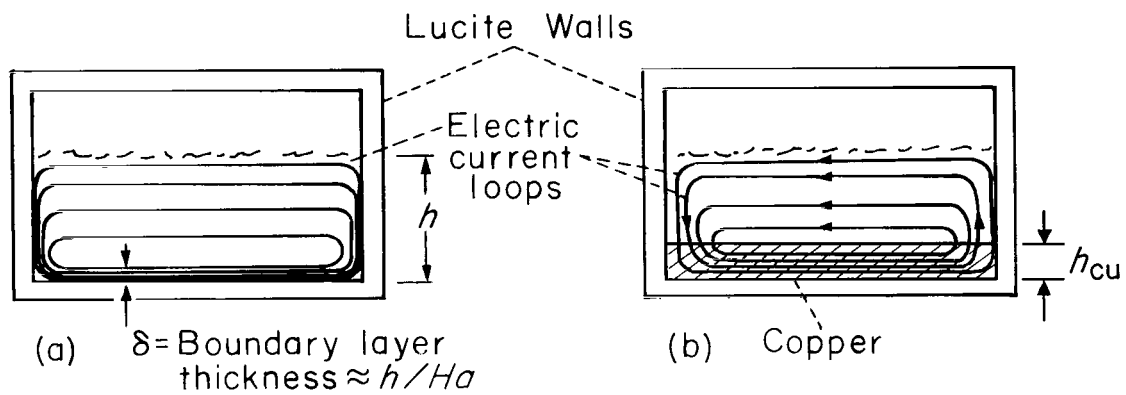
(a) Insulating walls.

(b) Conducting bottom.

Electric current loops

u_0

(c)

Moving fluid element
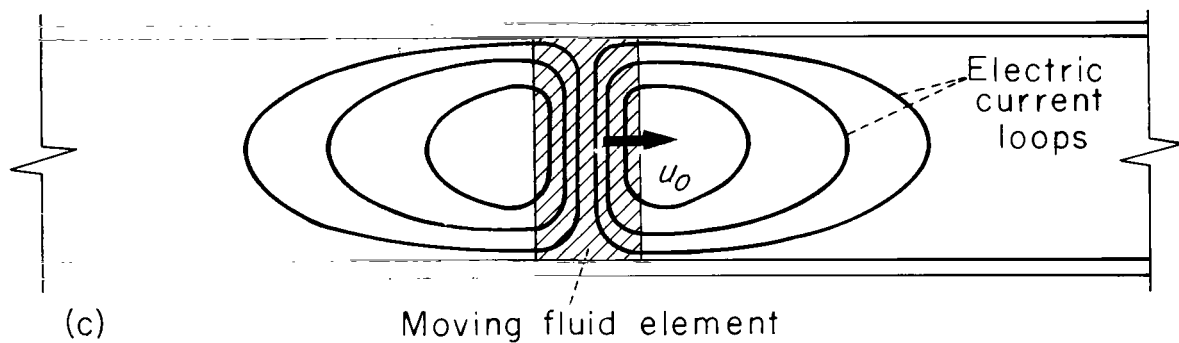
(c) Top view – insulating walls.

Figure 9.– Possible electric current paths for experiments.

Moving
fluid element⌐
($u = u_0 \approx$ const)

u_0

N

S

(a)
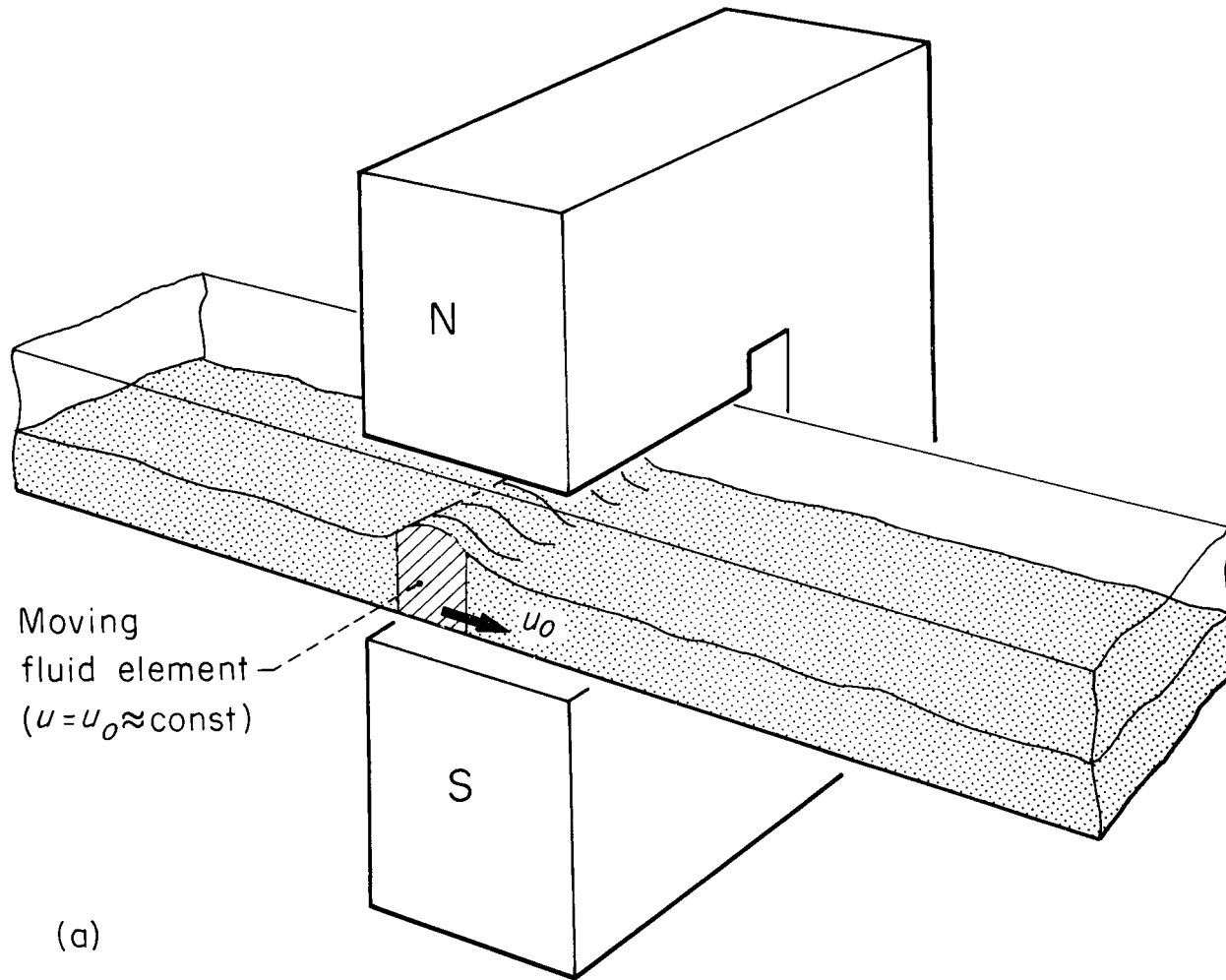
(a) Fluid moving through magnet air gap.

Figure 10.- Illustration of equivalent systems for induced electric field.

Region of
induced emf

u_0

(b)
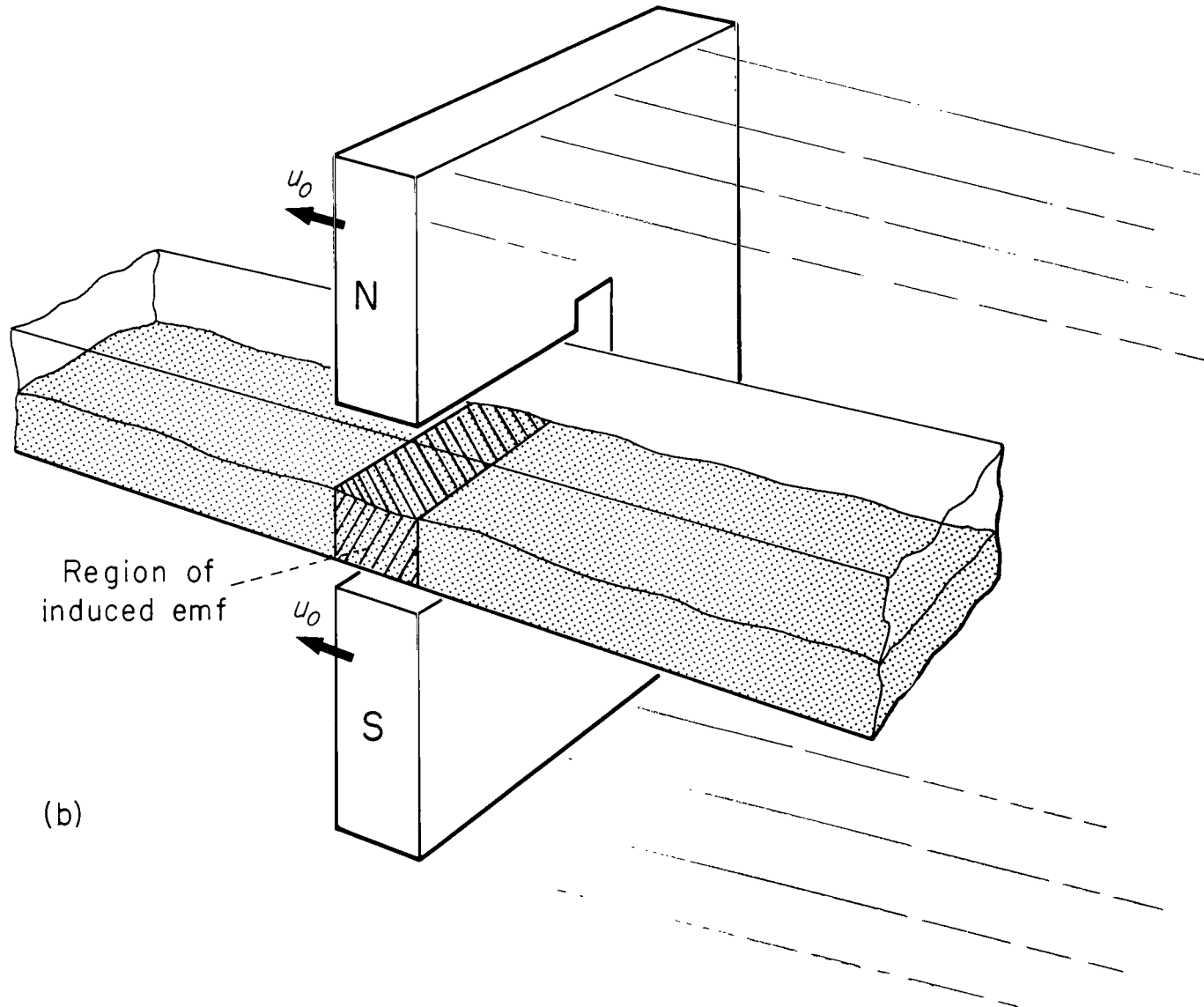
(b) Magnet moving past fluid.

Figure 10.- Concluded.
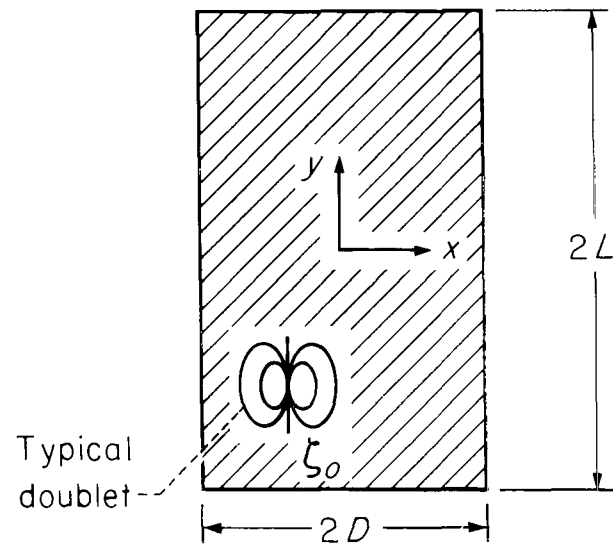
Figure 11.- Plan view of region of integration for rectangular block of emf in an unbounded medium.
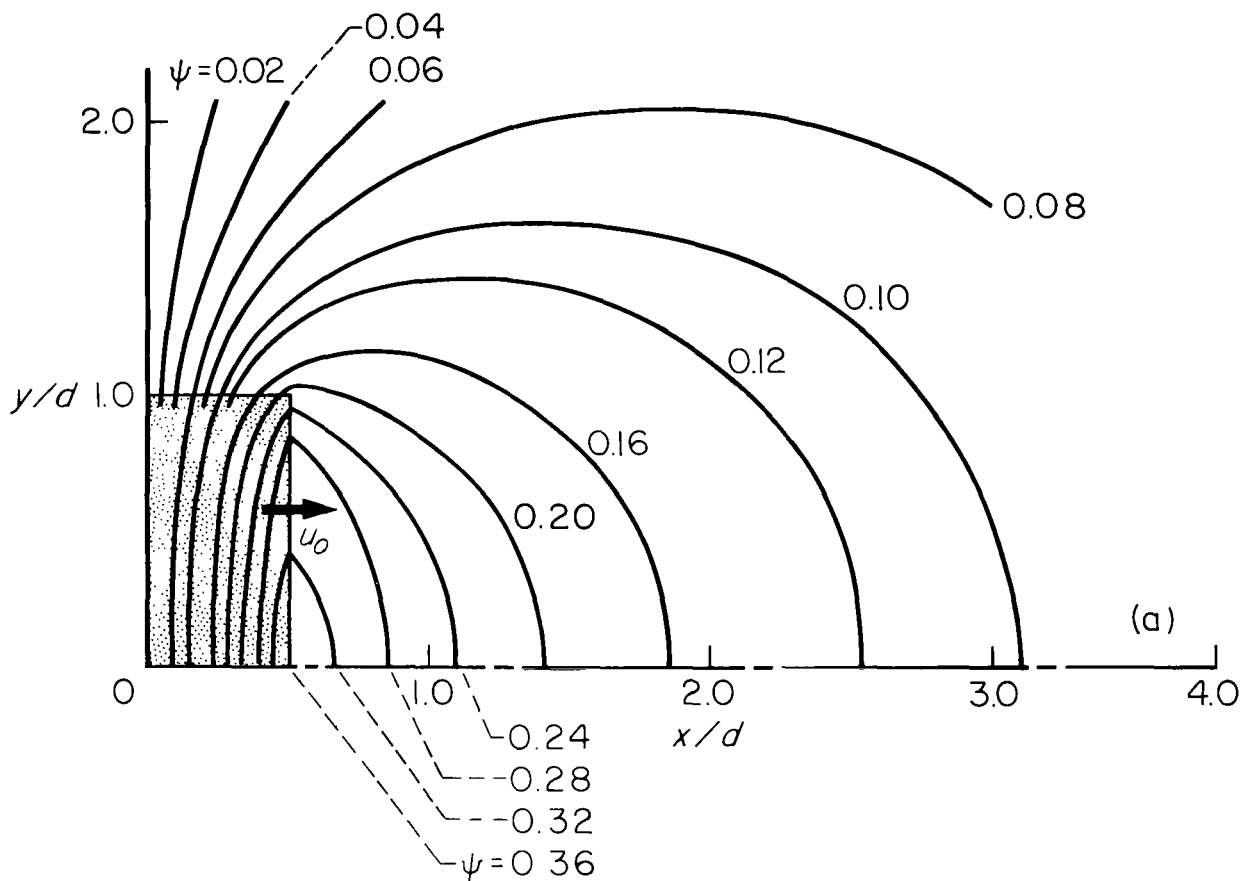
(a) L/D = 2.0

Figure 12.- Plan view of electric current paths for rectangular block of emf in an unbounded medium.
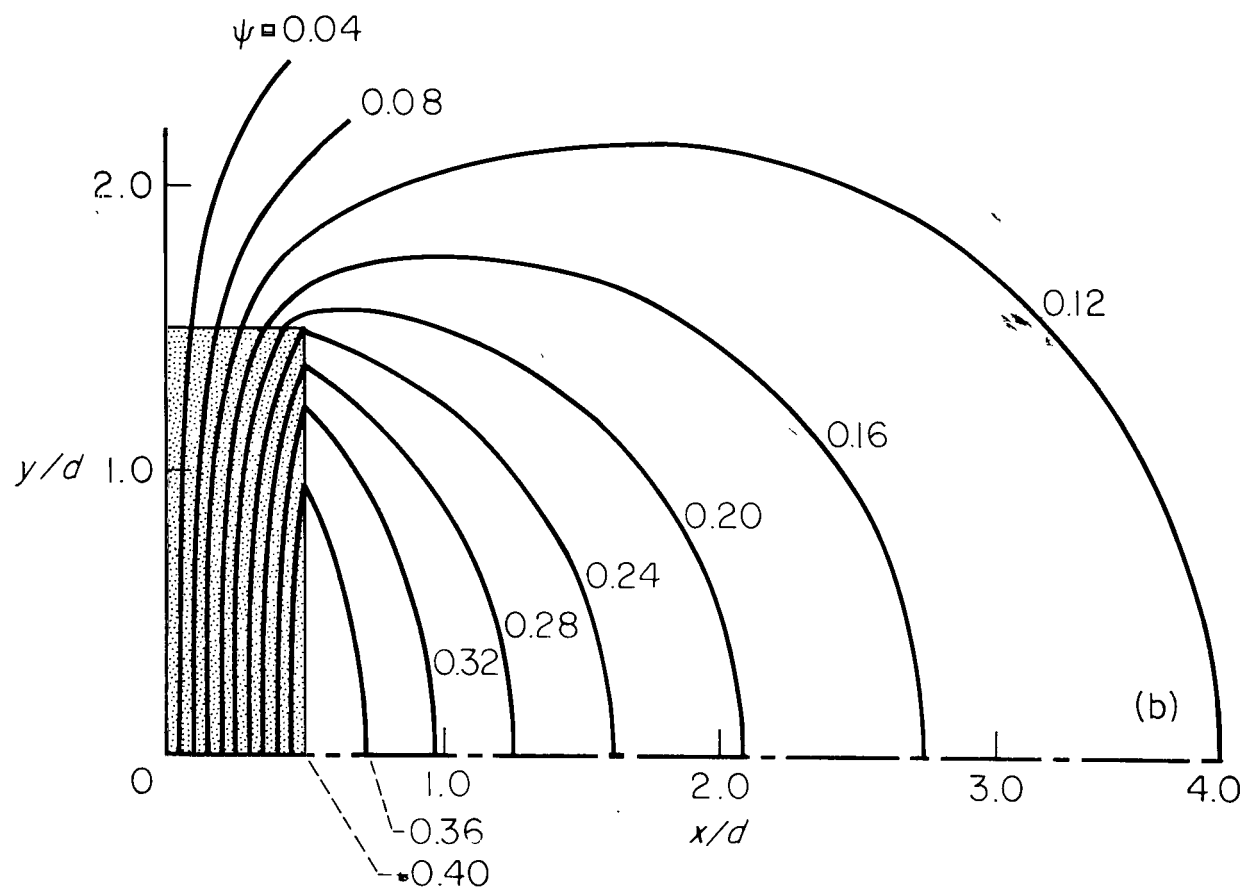
(b) L/D = 3.0

Figure 12.- Concluded.
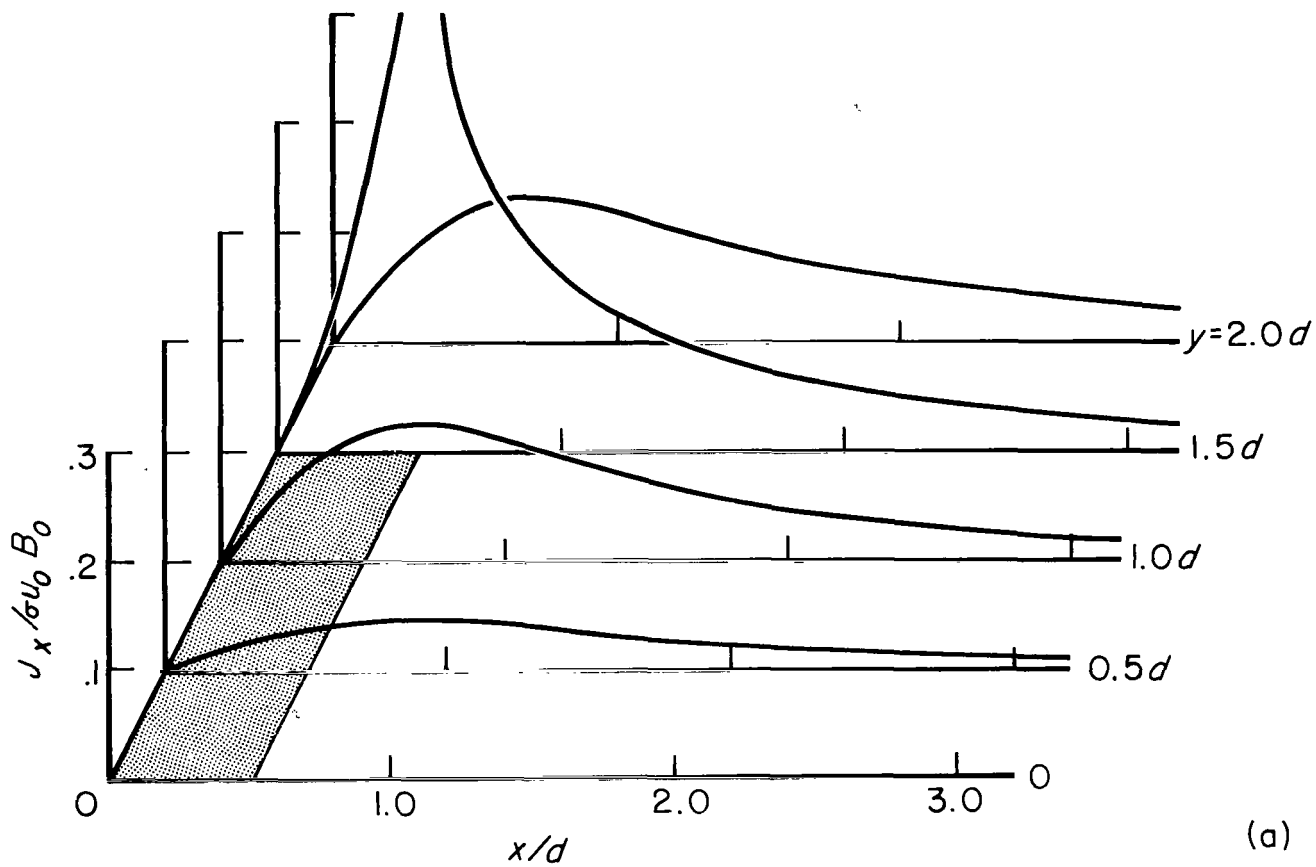
(a) Longitudinal component.

Figure 13.- Electric current density for magnet of rectangular plan form moving over unbounded medium; L/D = 3.0.
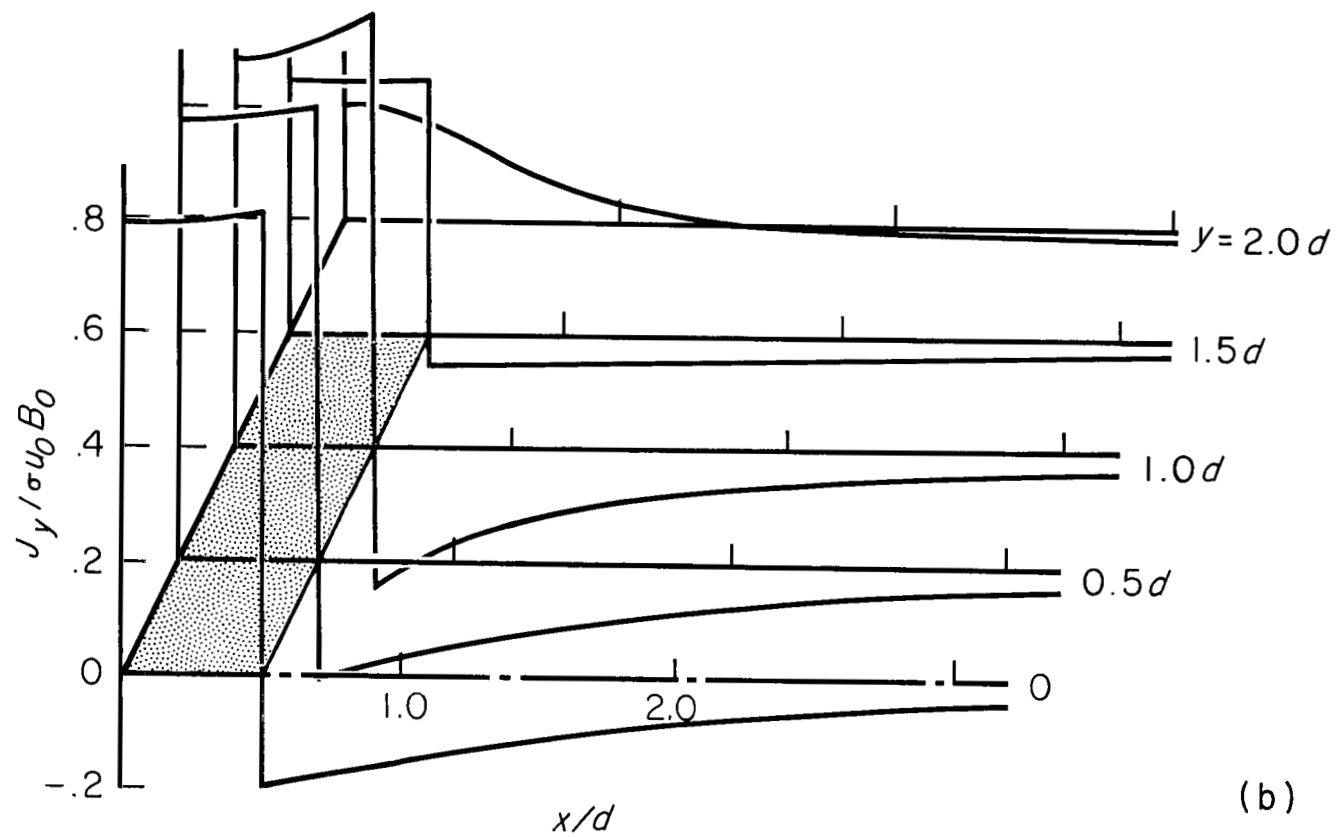
(b) Transverse component.

Figure 13.- Concluded.
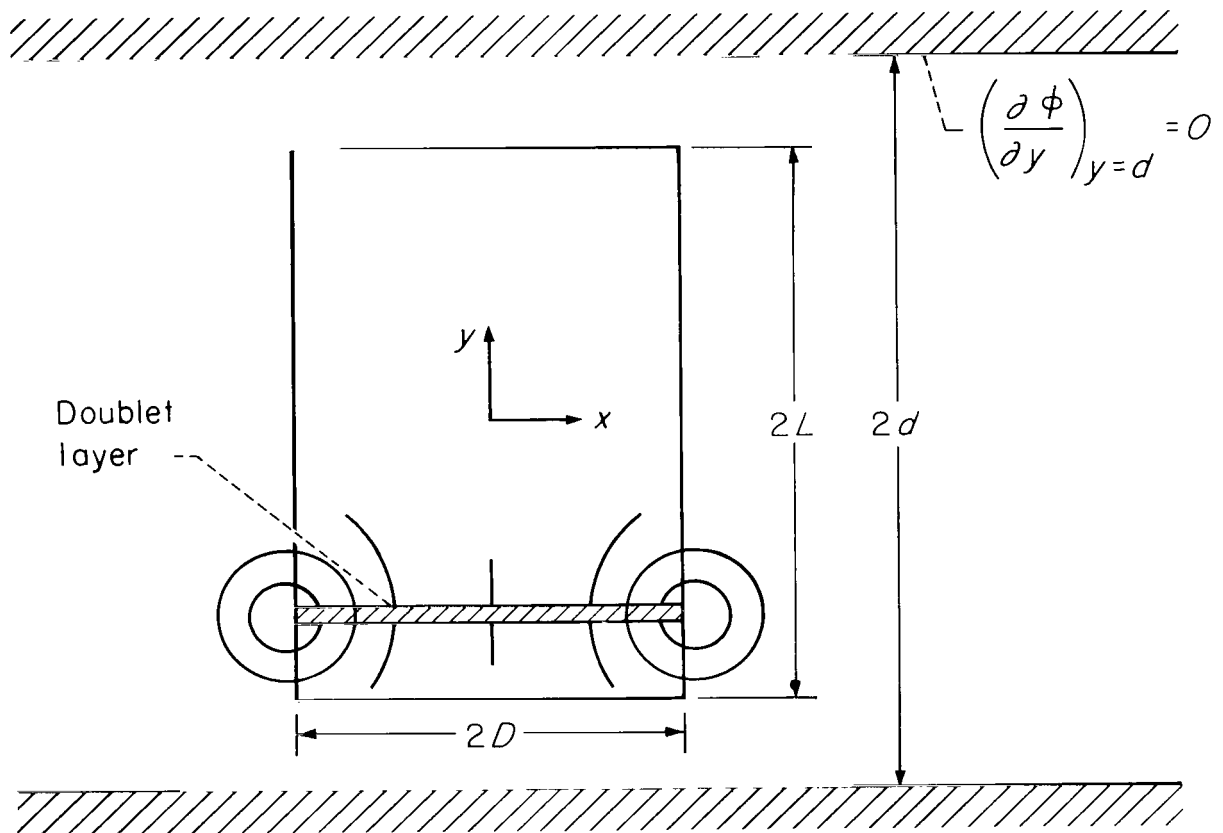
Figure 14.- Region of integration for rectangular block of emf between two nonconducting walls.

$\psi = 0$ Channel wall

y/d .5

Magnet area

.025

.05

.10

.20 .15

(a)

Channel

x/d
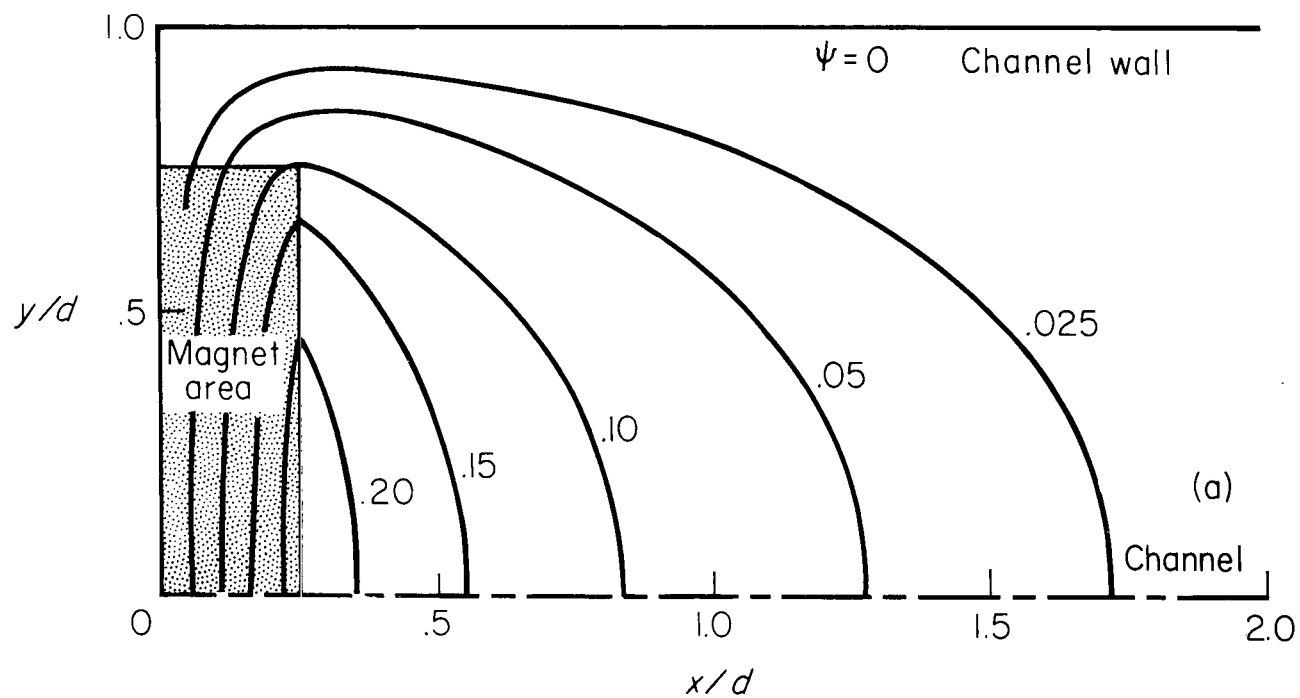
(a) L/D = 3.0; d/L = 1.333

Figure 15.- Plan view of electric current paths for rectangular magnet moving over fluid between two insulating walls.
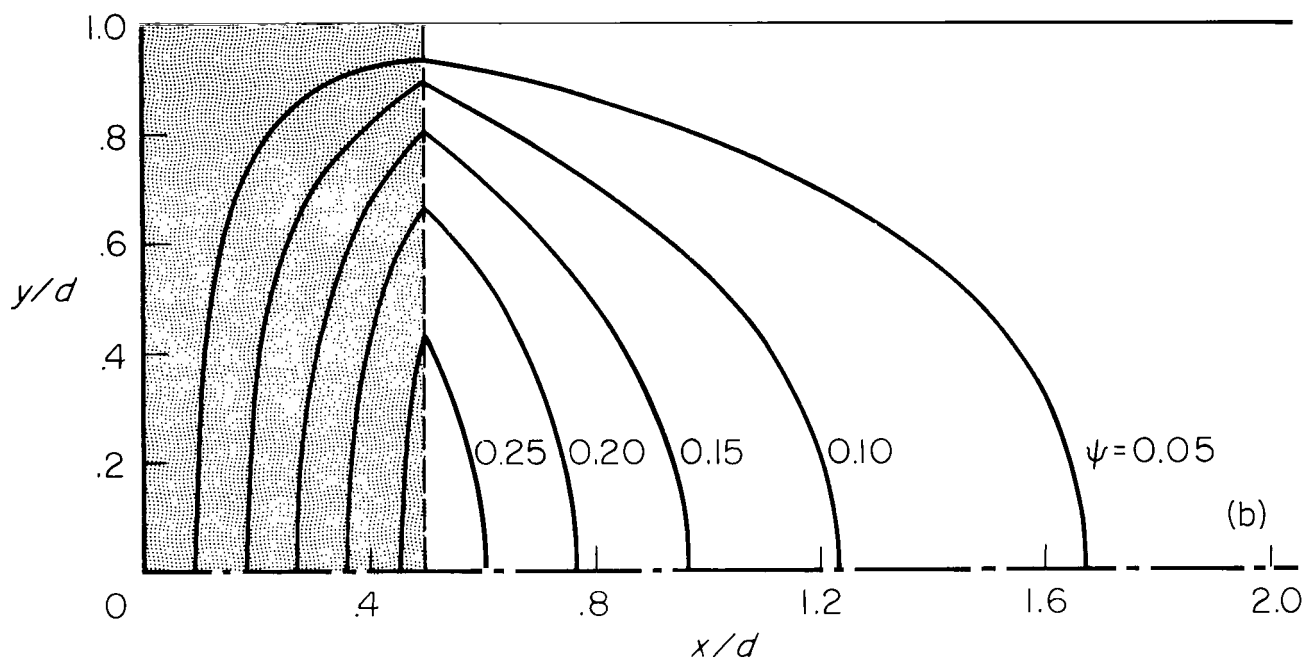
(b) L/D = 2.0; d/L = 1.0

Figure 15.- Continued.

(c) L/D = 1.0; d/L = 1.0
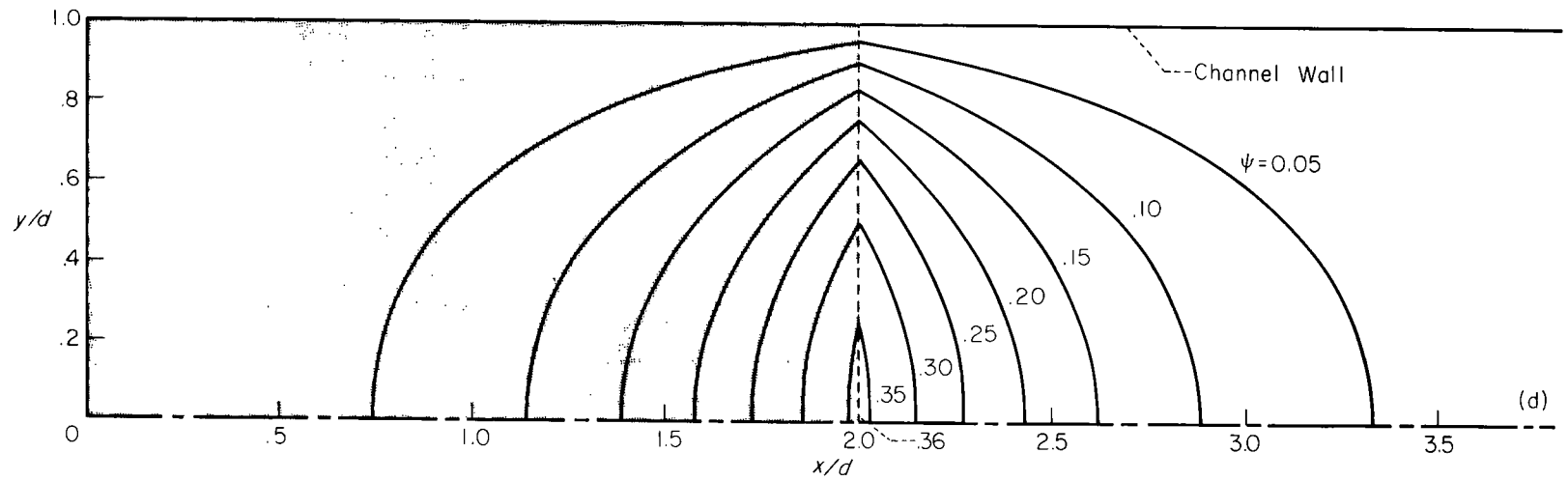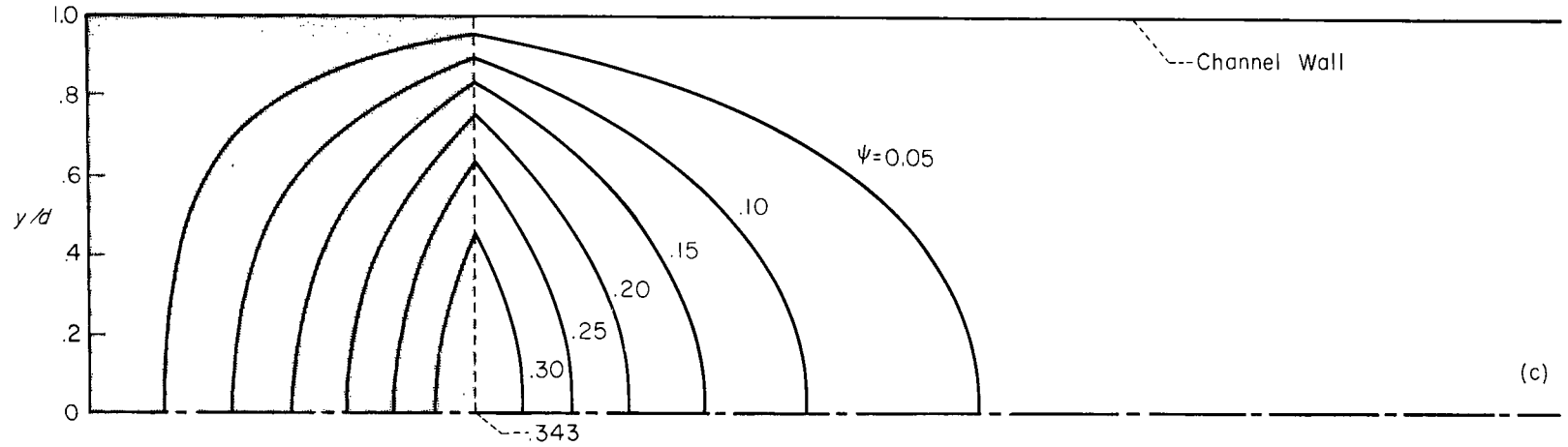
(d) L/D = 2.0; d/L = 1.0

Figure 15.- Concluded.
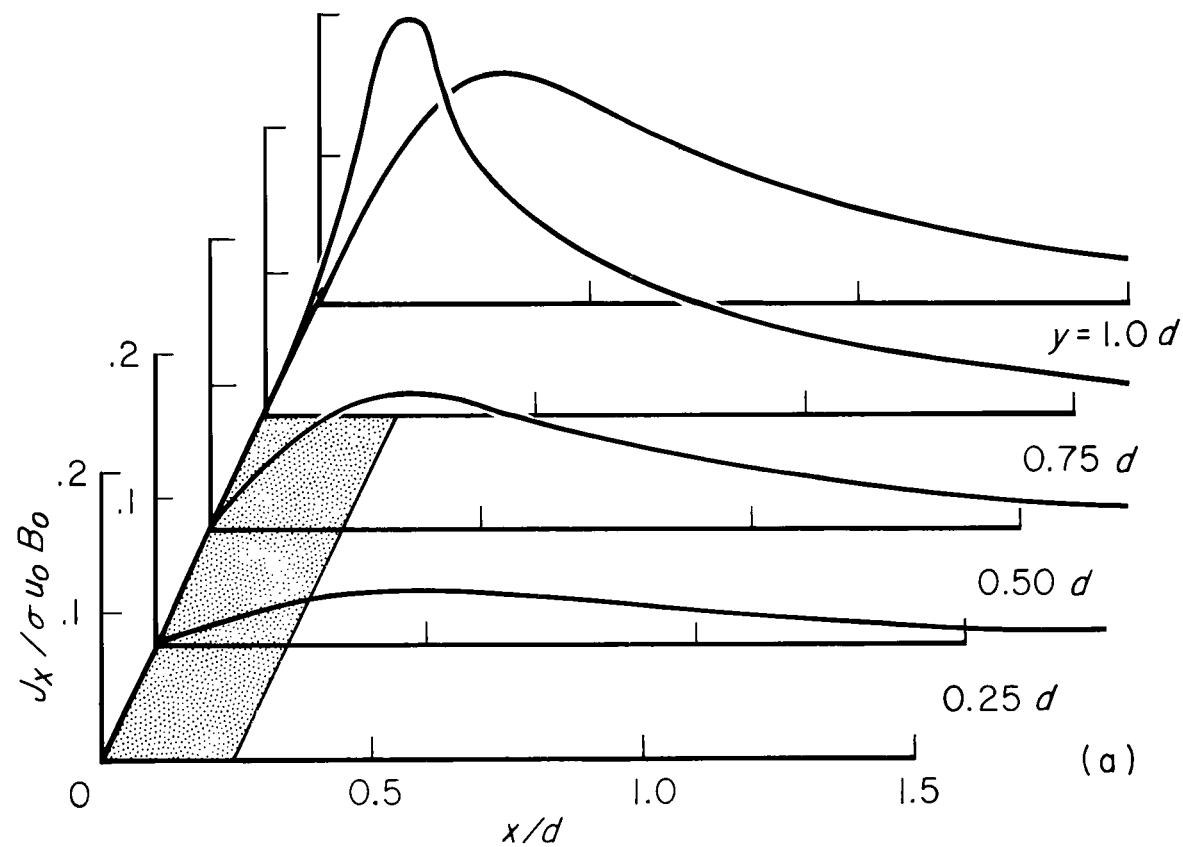
(a) Longitudinal component.

Figure 16.- Electric field intensity for rectangular magnet moving over fluid between two insulating walls; L/D = 3.0, d/L = 1.333.
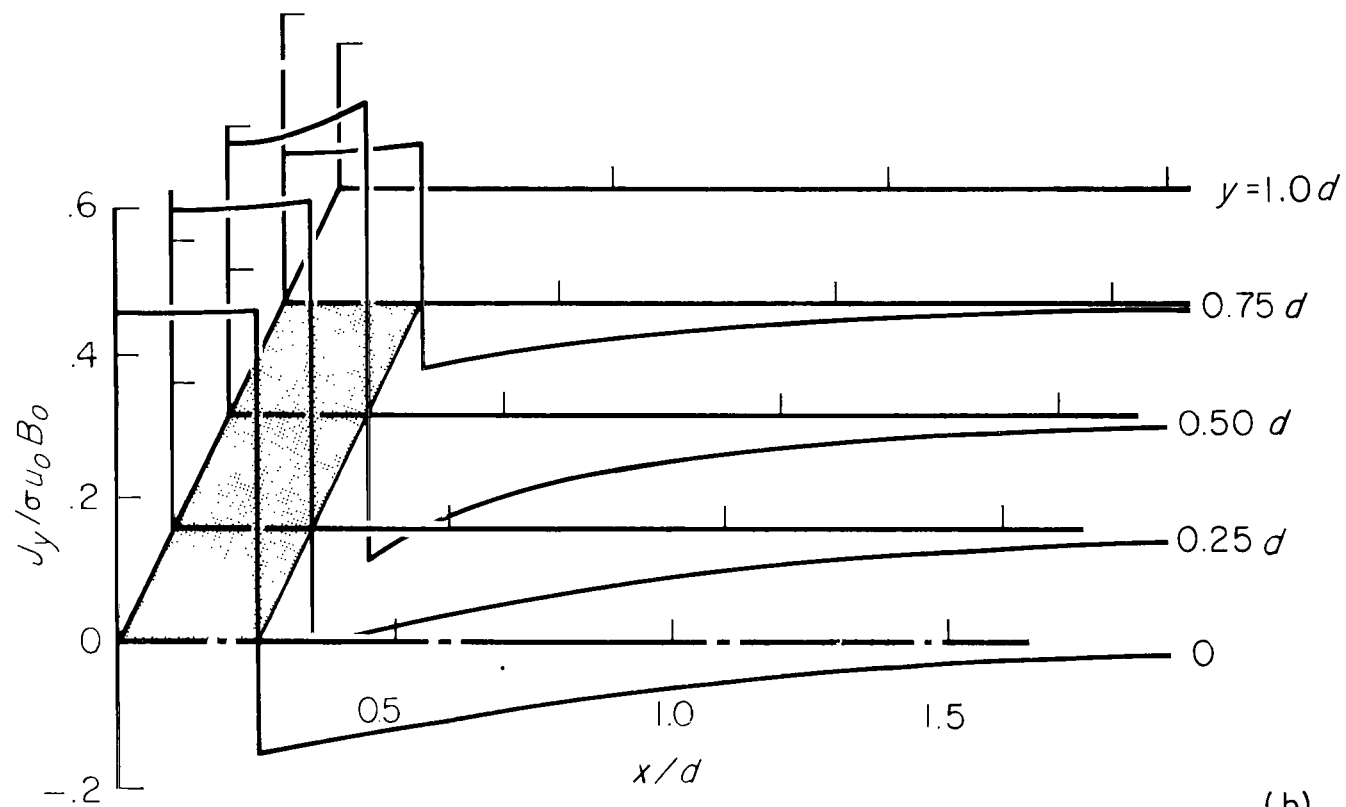
(b) Transverse component.

Figure 16.- Concluded.
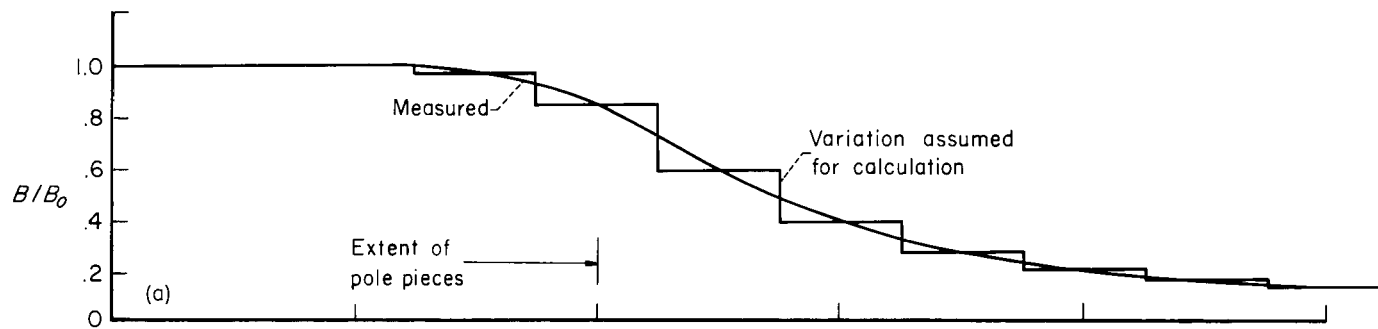
(a) Magnetic field strength as a function of distance along channel.
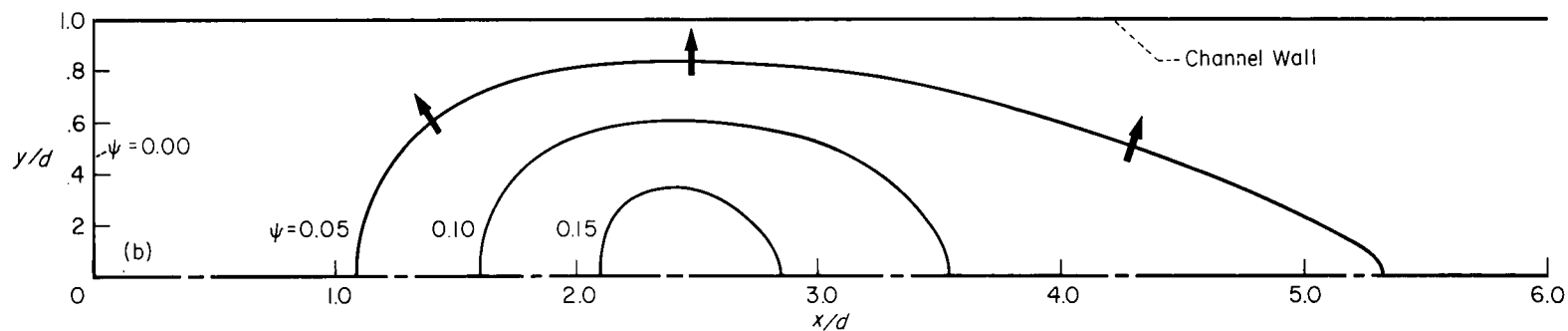
(b) Plan view of electric current lines.

Figure 17.- Electric field induced by 4- by 4-inch electromagnet as it moves over fluid confined between two insulating walls; d = 1 inch.
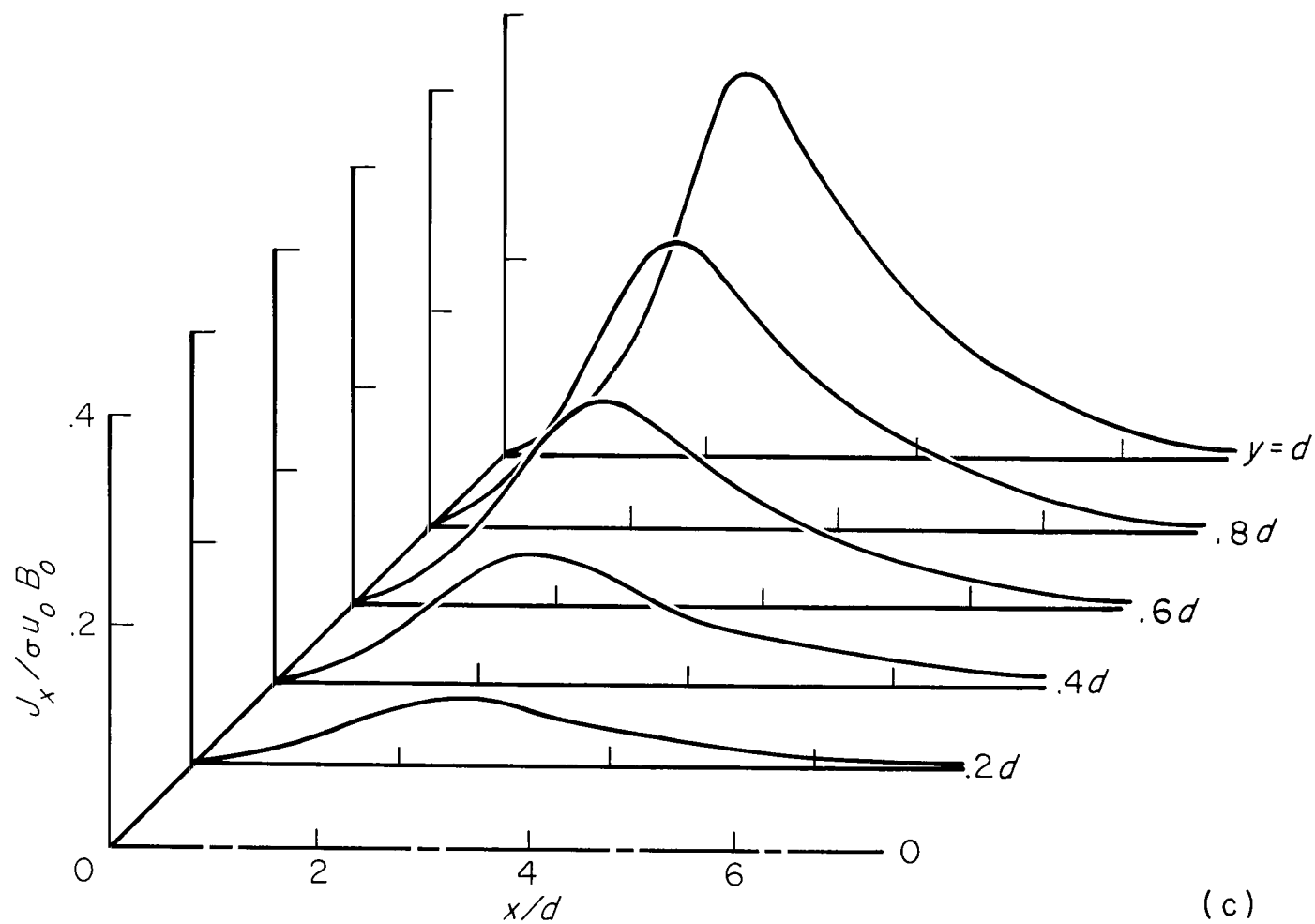
(c) Longitudinal electric field intensity.

Figure 17.- Continued.
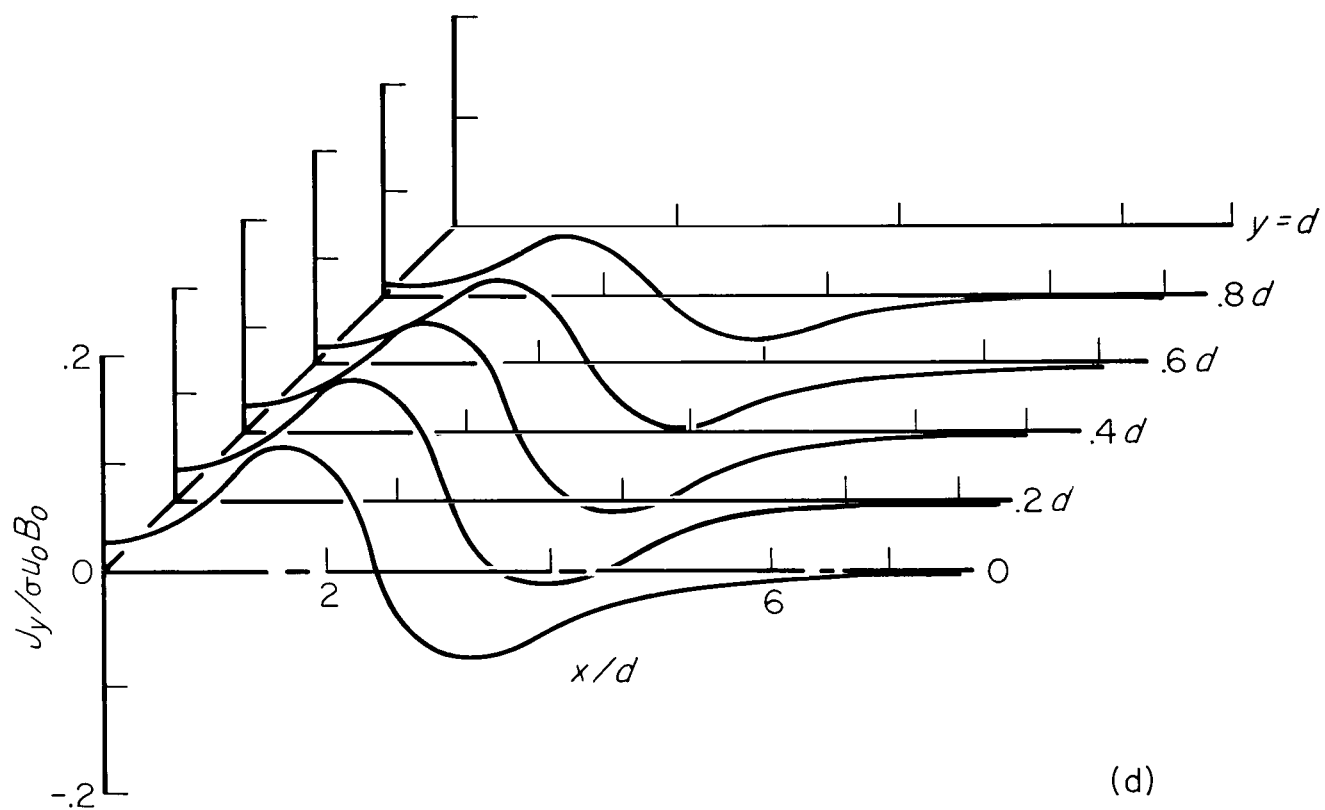
(d) Transverse electric field intensity.

Figure 17.- Concluded.
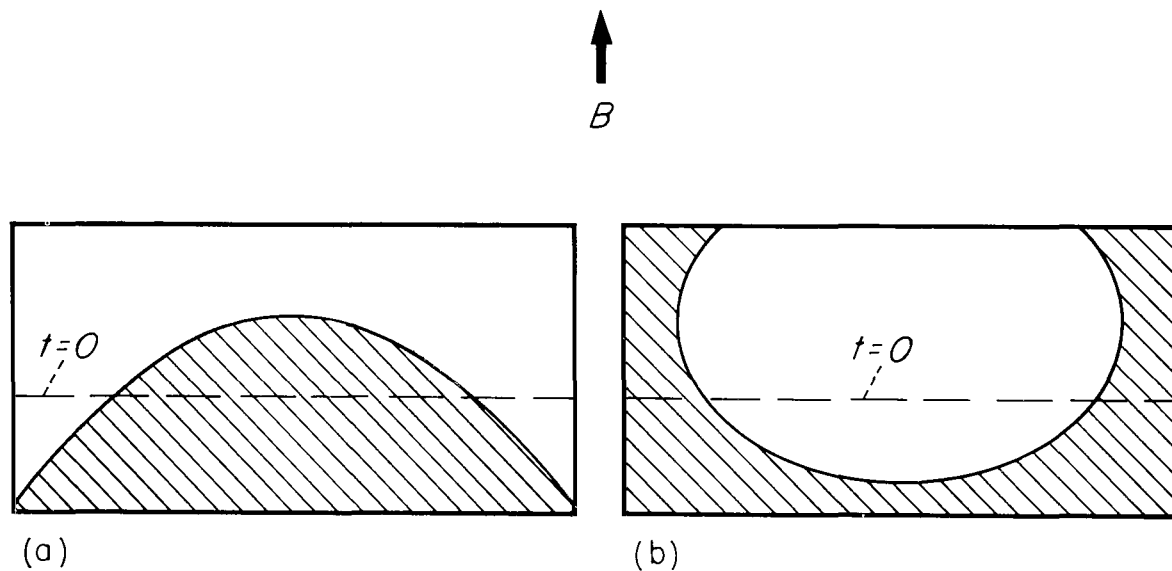
(a) Magnet on; B_Z is increasing.   (b) Magnet off; B_Z is decreasing.

Figure 18.- Cross-sectional view of surface shape of NaK as magnet is turned
on and off.
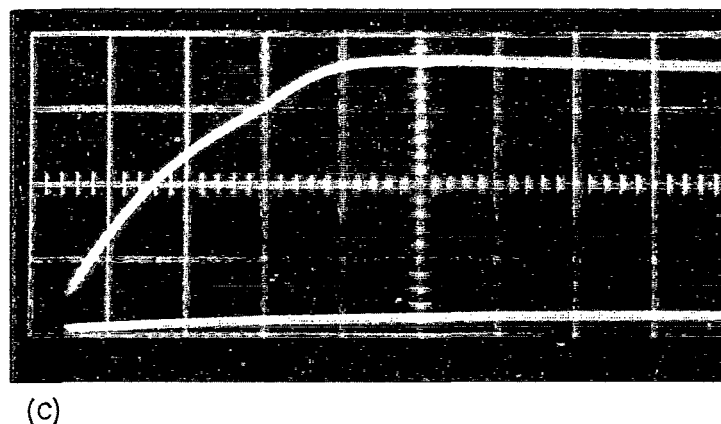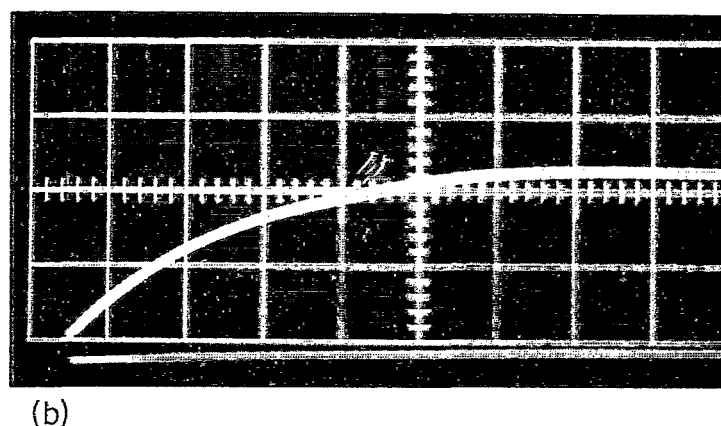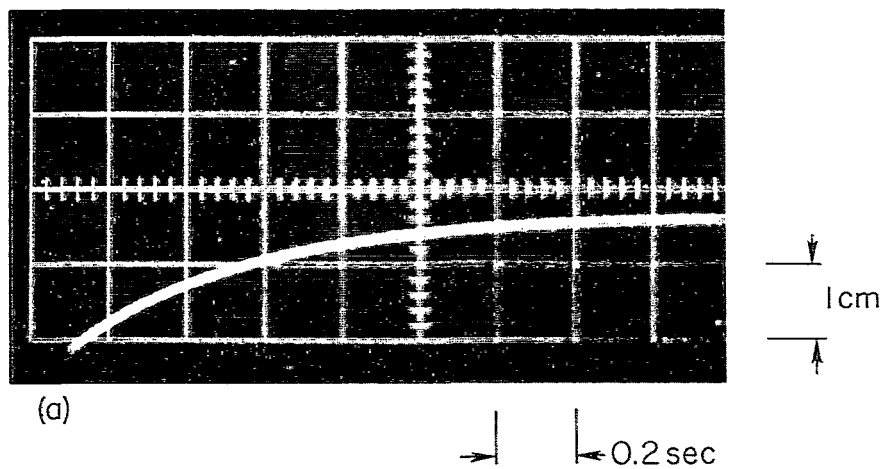
(a) I_{max} = 4.45 amperes.
(b) I_{max} = 10.5 amperes.
(c) I_{max} = 14.4 amperes.

Figure 19.- Electric current through windings of 4- by 4-inch magnet (1-1/2-inch air gap) as a function of time after switch is closed; sweep rate = 5.0 cm/sec.

69
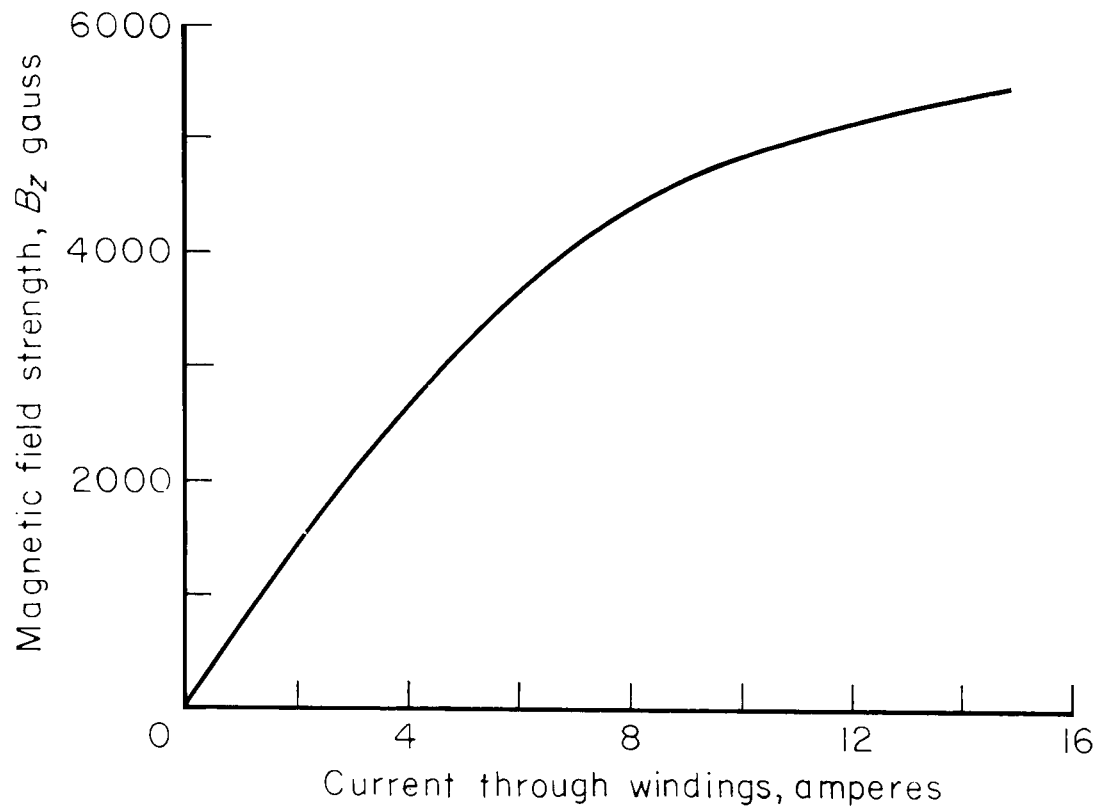
Figure 20.- Magnetic field strength at the center of the air gap for 4- by 4-inch solid core electromagnet used in experiments; 1-1/2-inch air gap.

(a) L/D = 1, d/L = 1
(b) L/D = 0.5, d/L = 1
(c) 4- by 4-inch magnet, 1-1/2-inch air gap, 2-inch channel width.
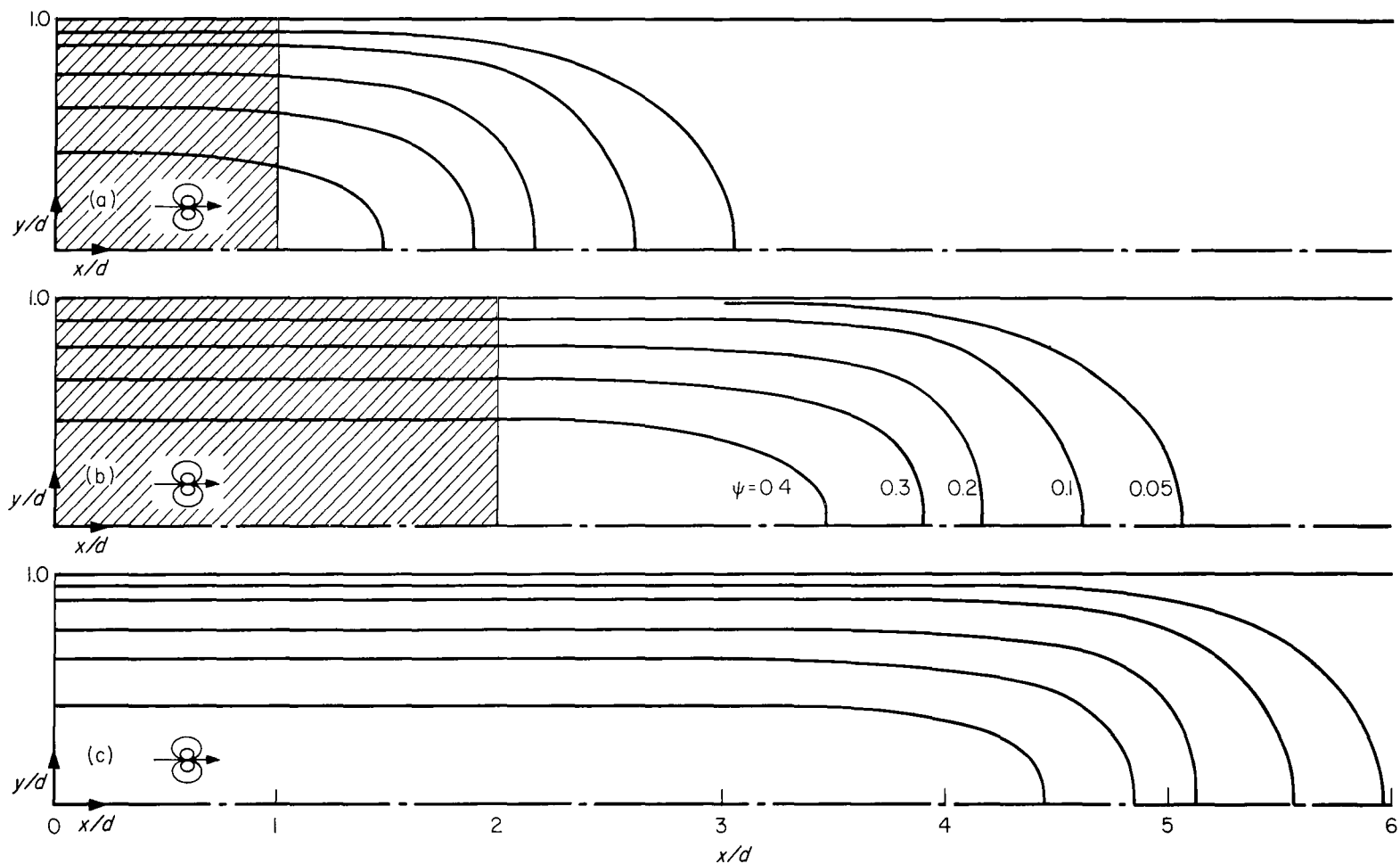
Figure 21.- Plan views of theoretical electric current paths as various magnet shapes are energized
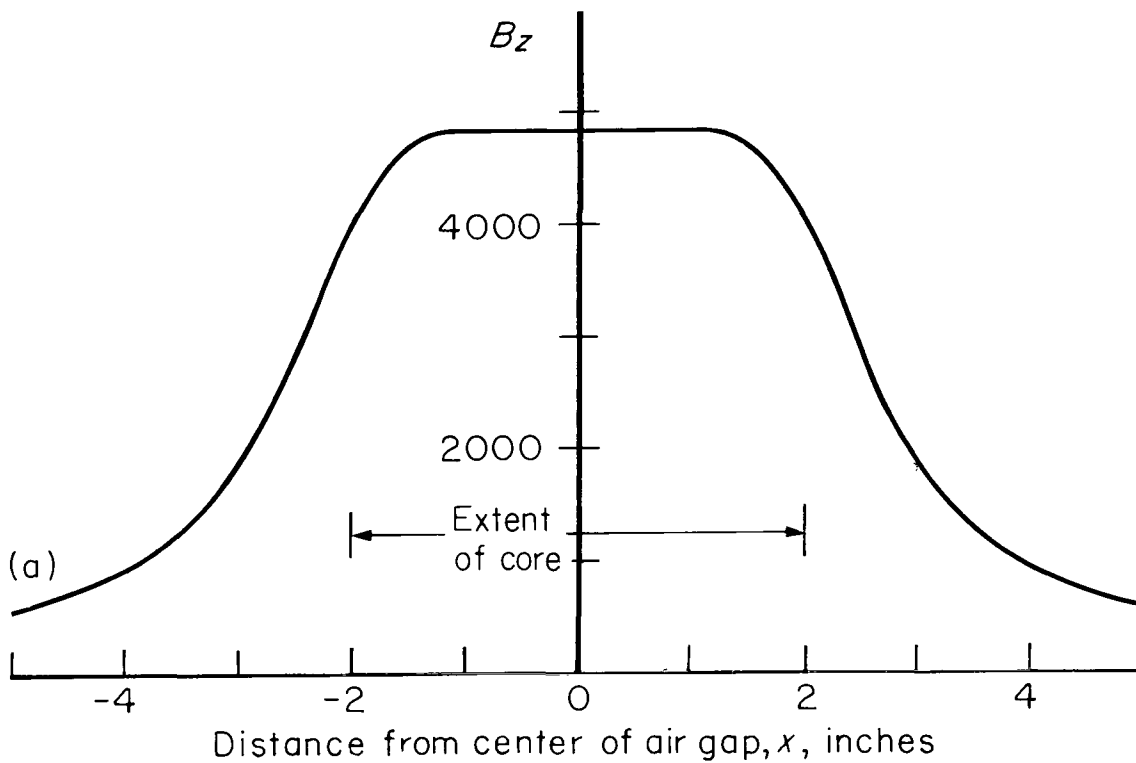
(a) Magnetic field strength along center line of magnet.

Figure 22.- Magnetic field strength distribution as measured for 4- by 4-inch solid iron core electromagnet with 1-1/2-inch air gap and 10 amperes current through windings.
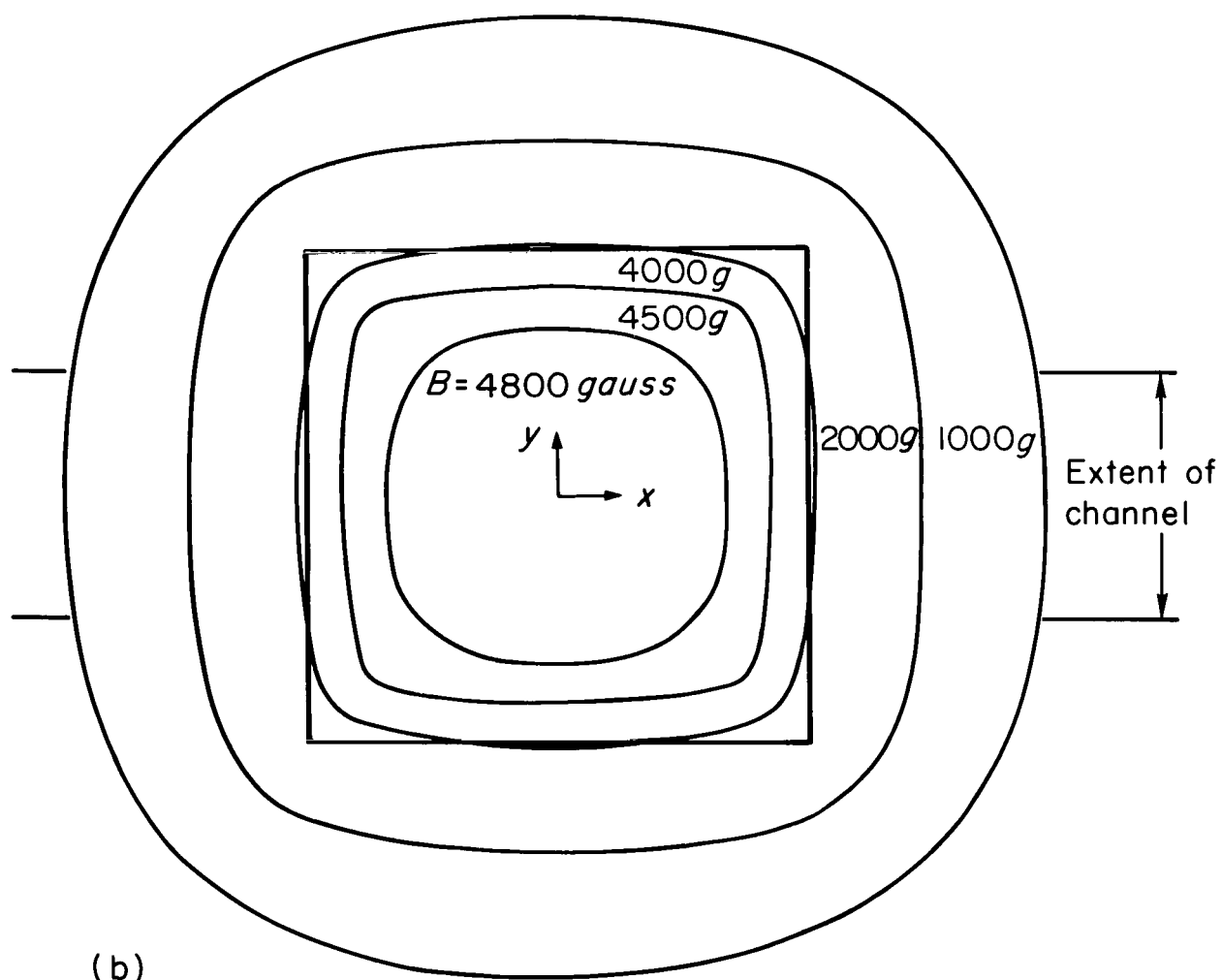
(b) Contours of equal magnetic induction.

Figure 22.- Concluded.
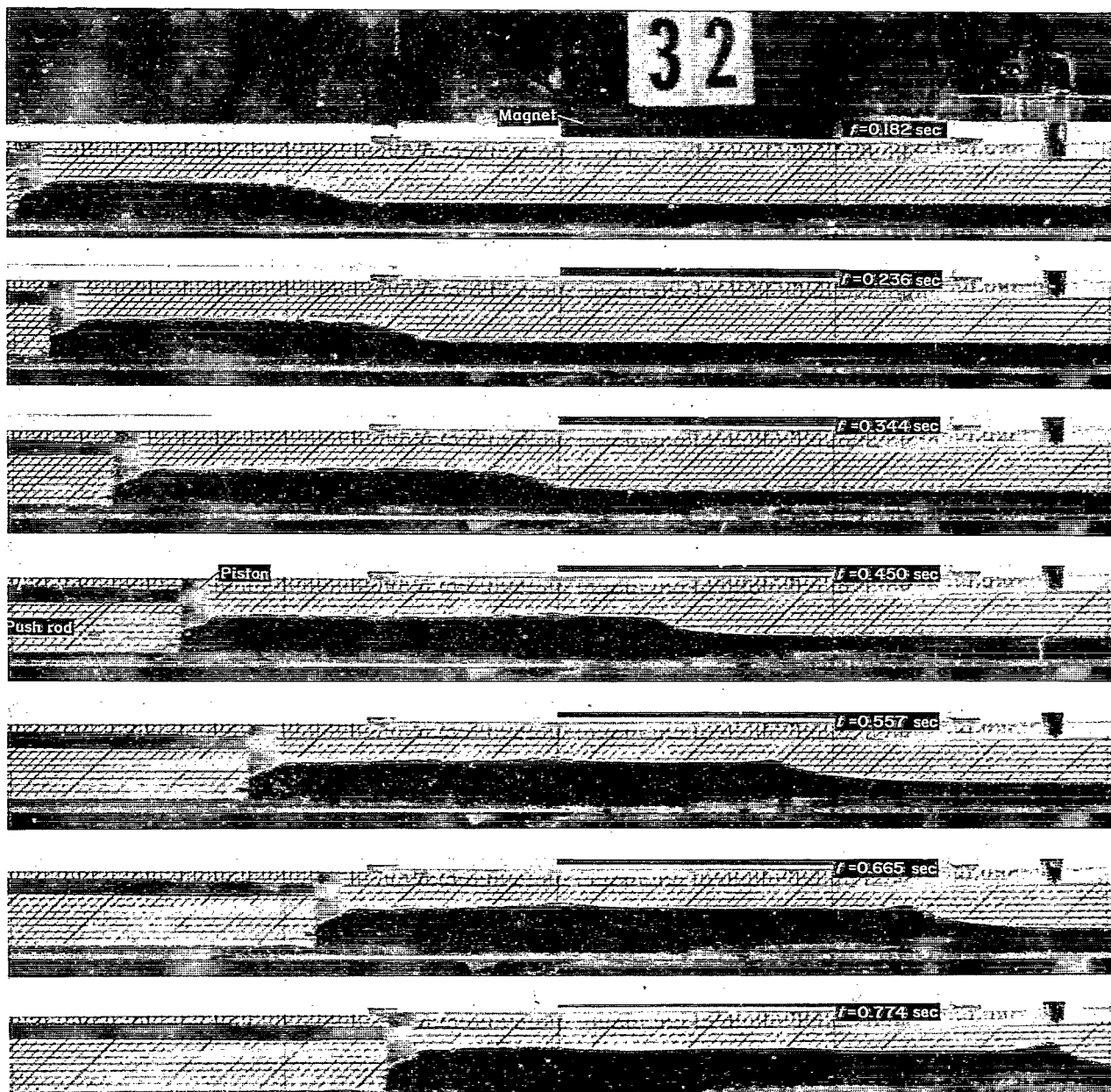
A-28829-2

Figure 23.- Compression wave in mercury impinging on magnetic field; insulating
walls and bottom, $U_p = 0.62$, $h_o = 0.37$ inch, $a_o = 1$ ft/sec, $P_{mo} = 1.48$, $C \approx 0$.

(a) Experimental surface profiles.

Figure 24.- Compression wave in mercury impinging on magnetic field; copper bottom in channel, U_p = 0.570, h_O = 0.35 inch, a_O = 0.97 ft/sec, P_{mO} = 1.523.

I $\tau = 1.245$

II 2.490

III 3.735

IV 4.980

V 6.225

VI (b)
7.470
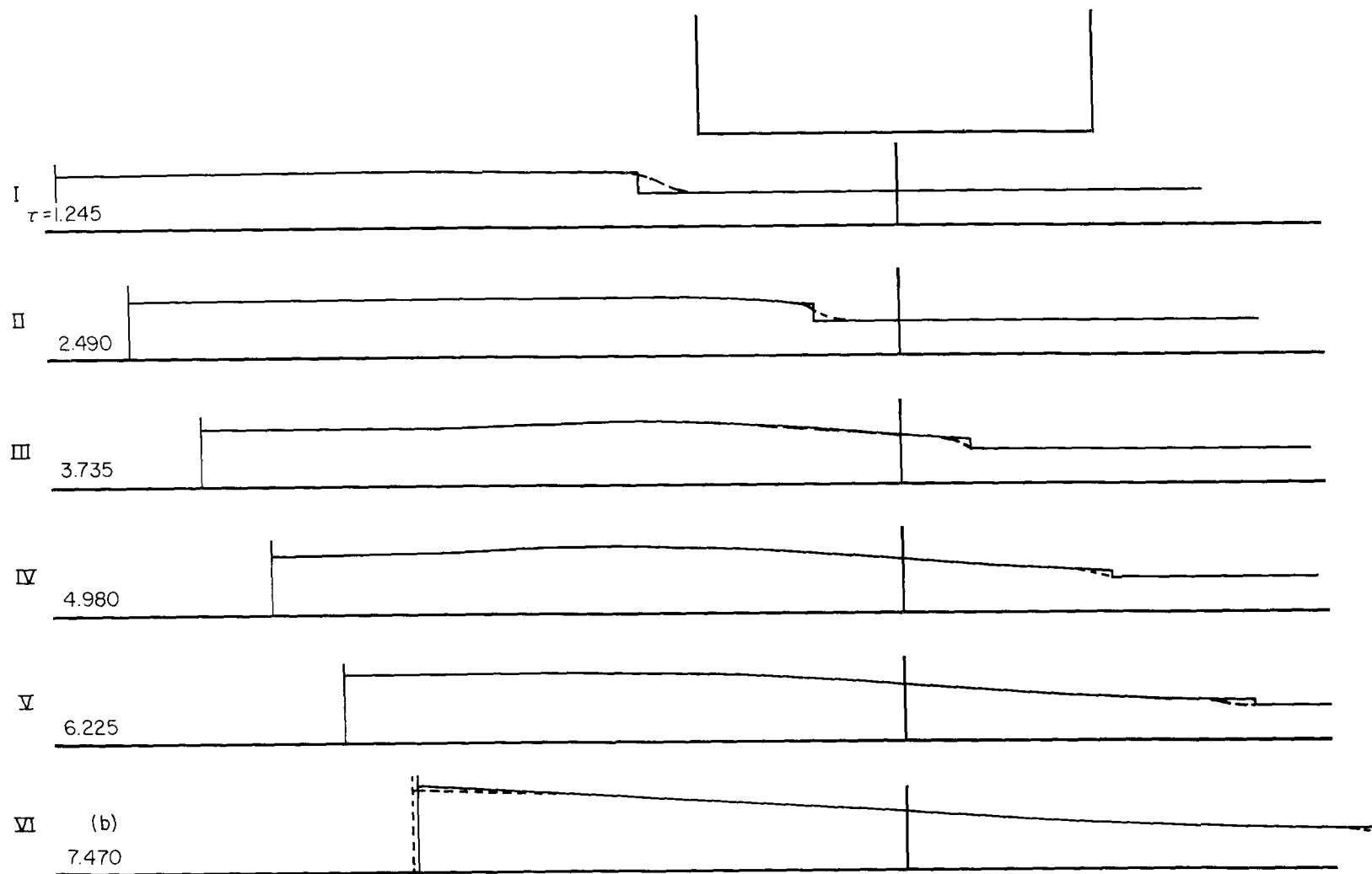
(b) Comparison of theory and experiment; C = 0.56.

Figure 24.- Concluded.
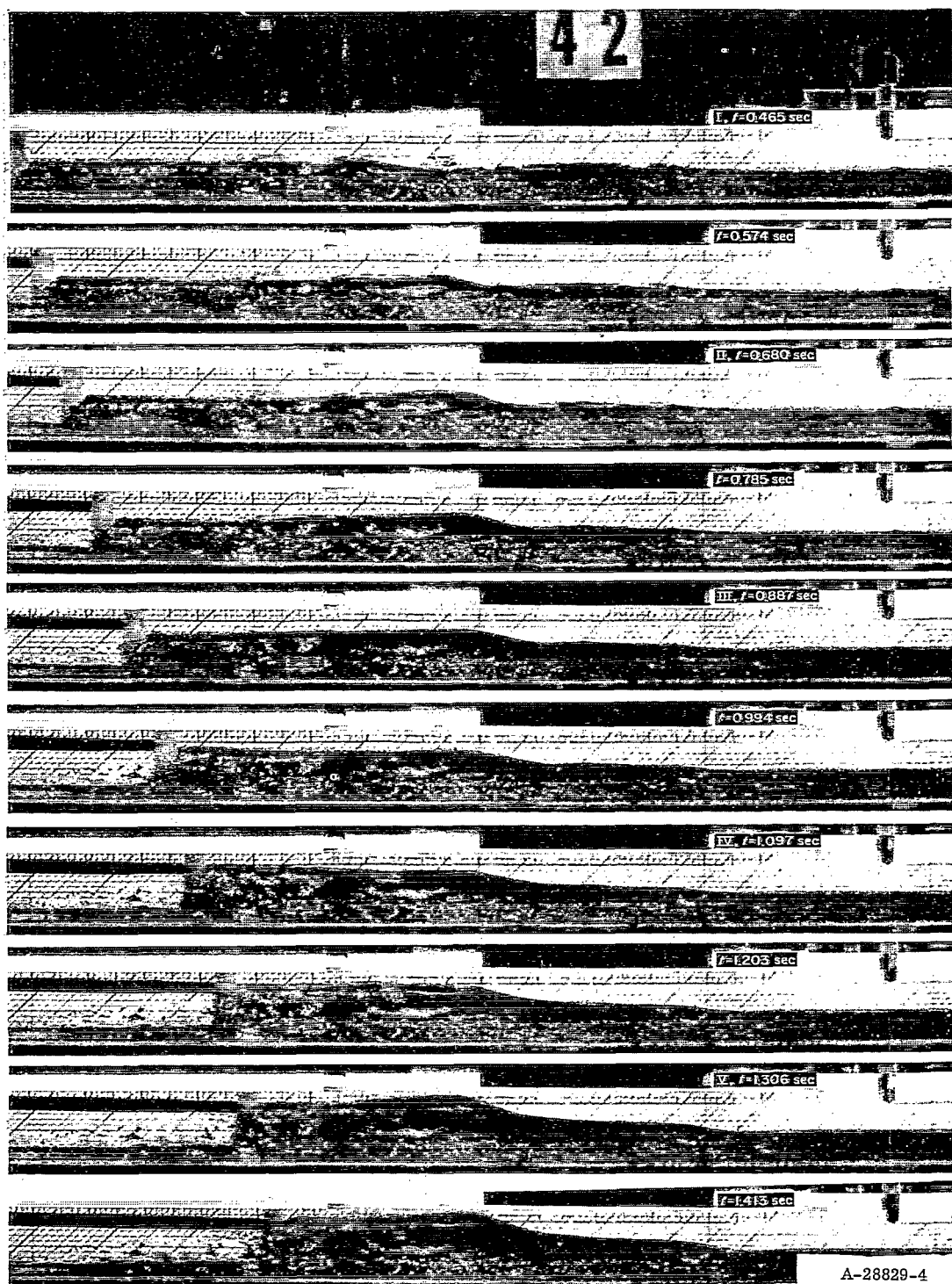
(a) Experimental surface profiles.

Figure 25.- Compression wave in NaK impinging on magnetic field; insulating walls and bottom, $U_p = 0.349$, $h_o = 0.52$ inch, $a_o = 1.18$ ft/sec, $P_{mo} = 54.5$.
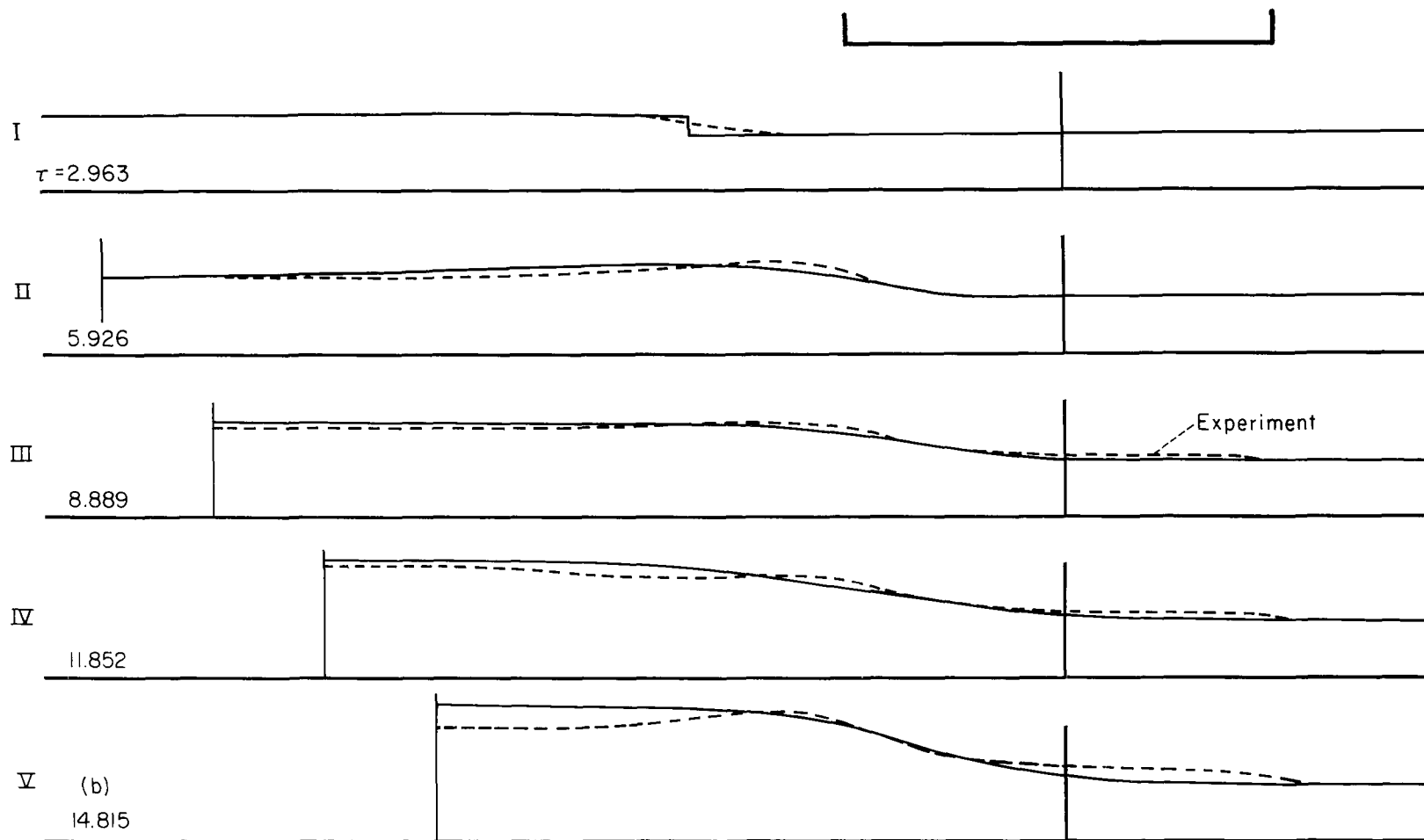
(b) Comparison of theory and experiment; C = 0.142.

Figure 25.- Concluded.

(a) Experimental surface profiles.

Figure 26.- Compression wave in NaK impinging on magnetic field; copper bottom in channel, U_p = 0.377, h_o = 0.42 inch, a_o = 1.06 ft/sec, P_{mo} = 60.4.
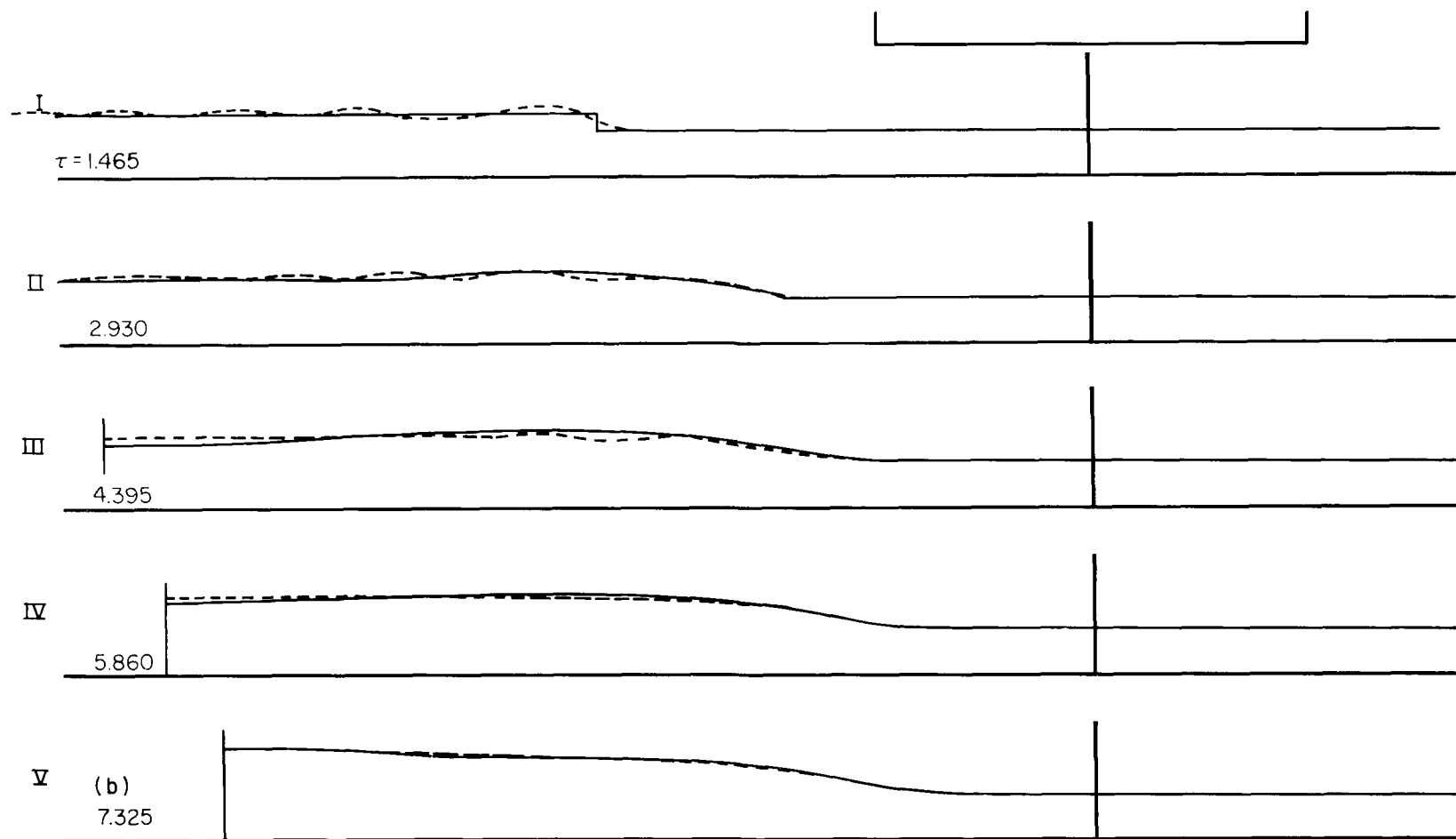
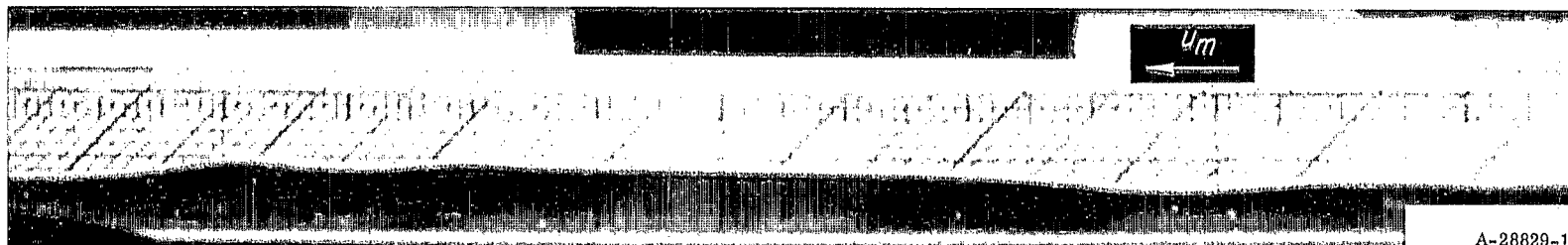(b) Comparison of theory and experiment; C = 0.64.

Figure 26.- Concluded.
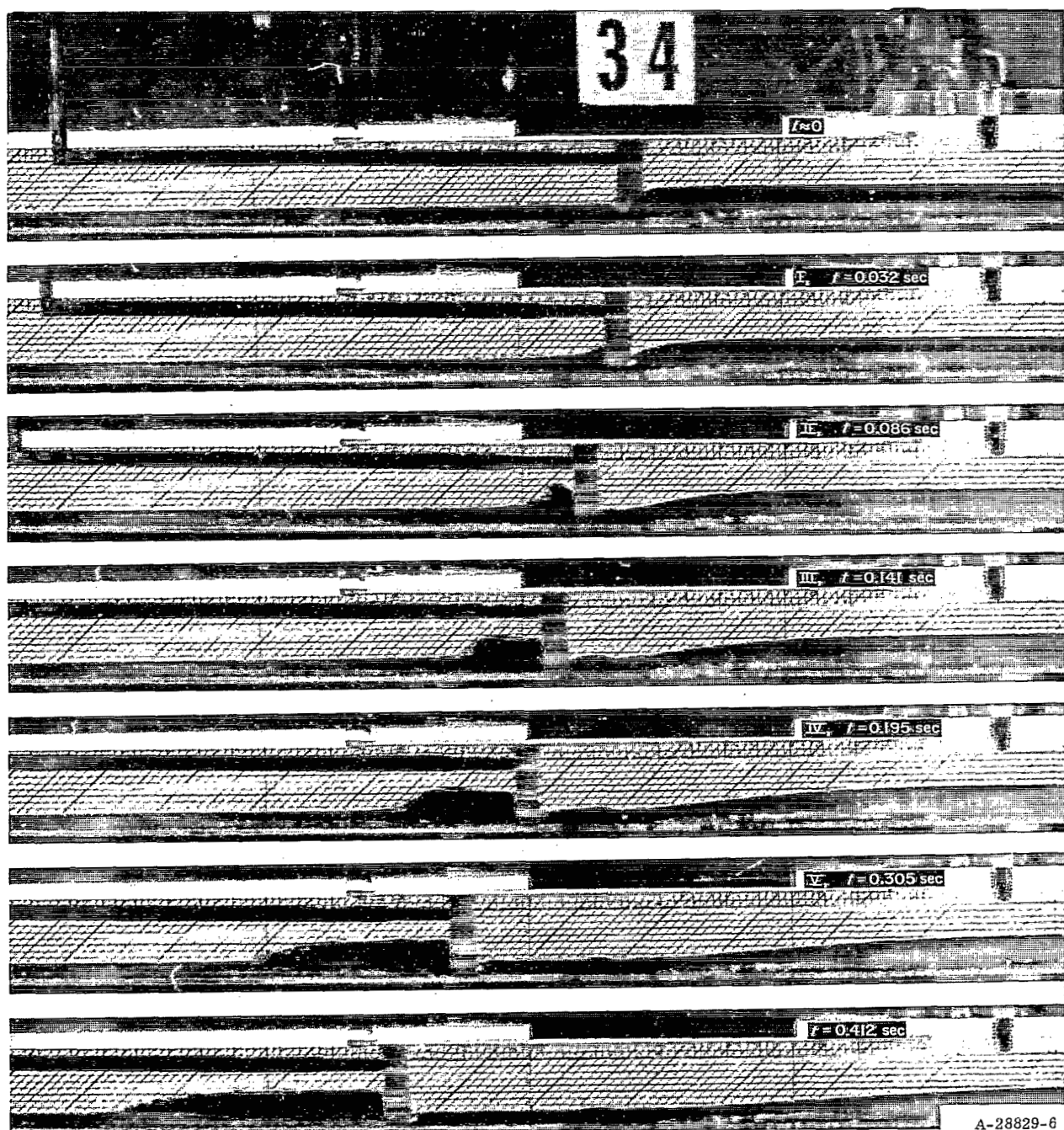
(a) Experimental surface profiles.

Figure 27.- Centered expansion in mercury; U_p = -0.63, h_O = 0.55 inch, a_O = 1.22 ft/sec, P_{mO} = 0.

(b) Comparison of theory and experiment.

Figure 27.- Concluded.

A-28829-7
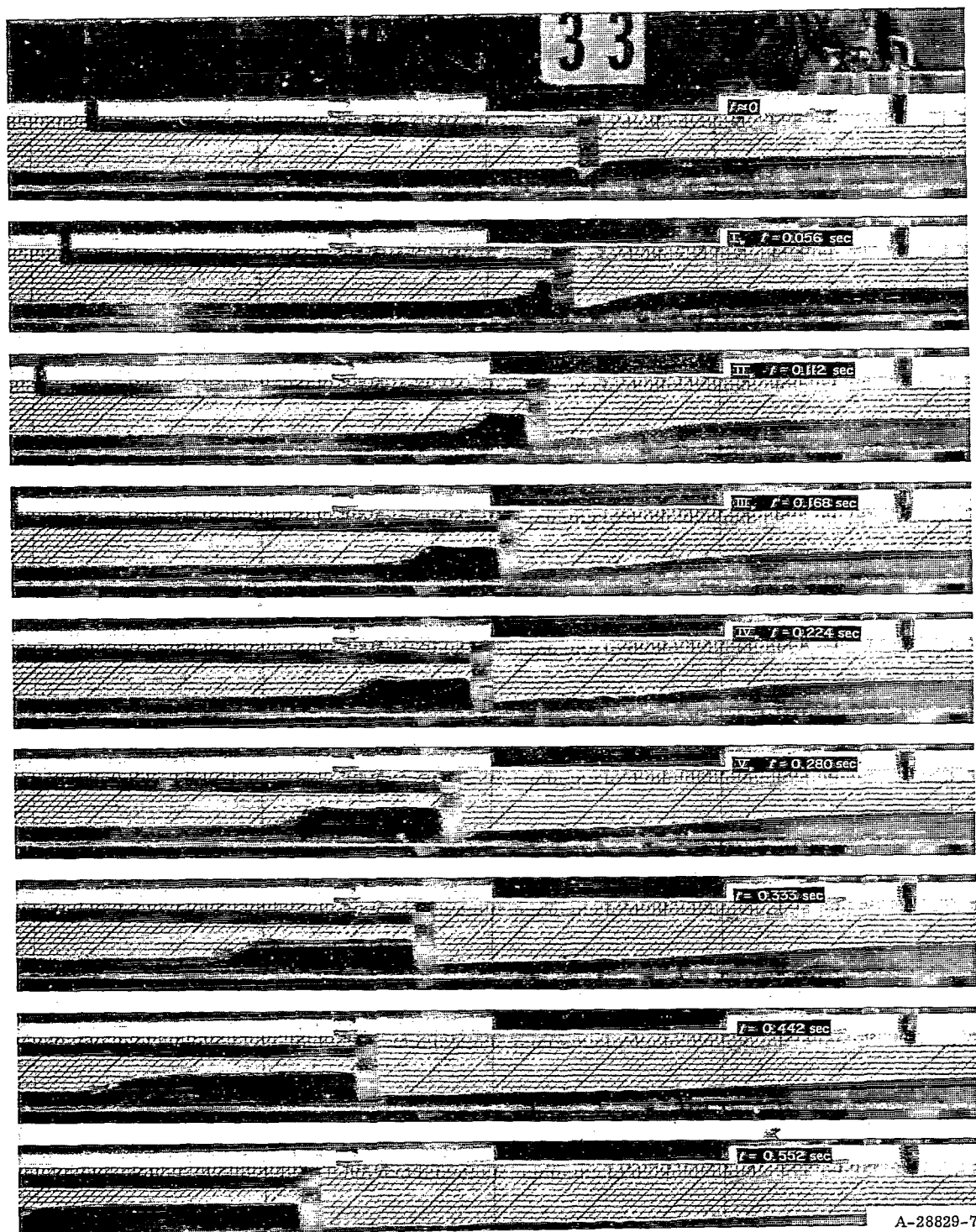
(a) Experimental surface profiles.

Figure 28.- Interaction of a transverse magnetic field with a centered expansion
in mercury; insulating walls and bottom, U_p = -0.63, h_o = 0.50 inch,
a_o = 1.16 ft/sec, P_{mo} = 1.28.
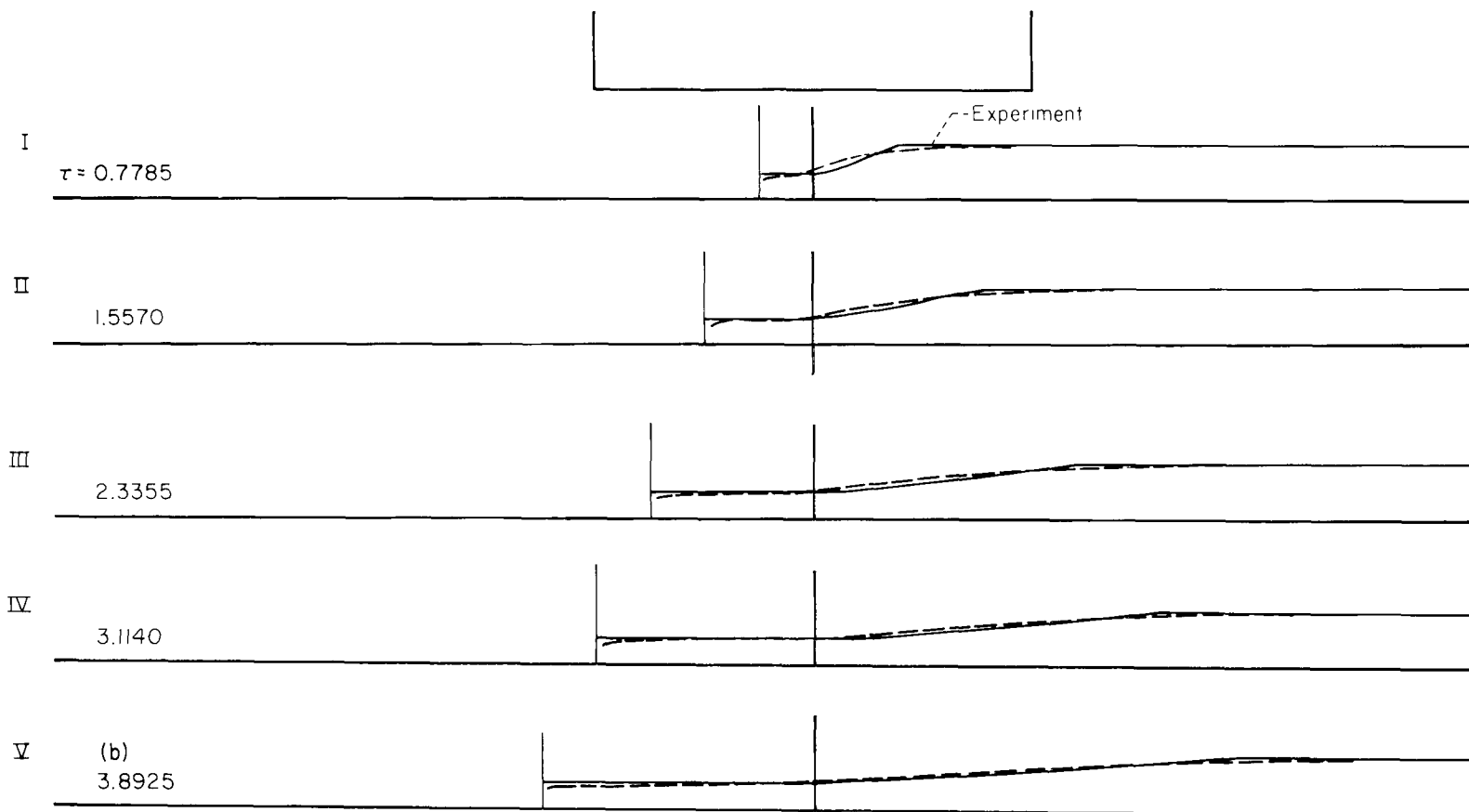
(b) Comparison of theory and experiment; C = 0.

Figure 28.- Concluded.
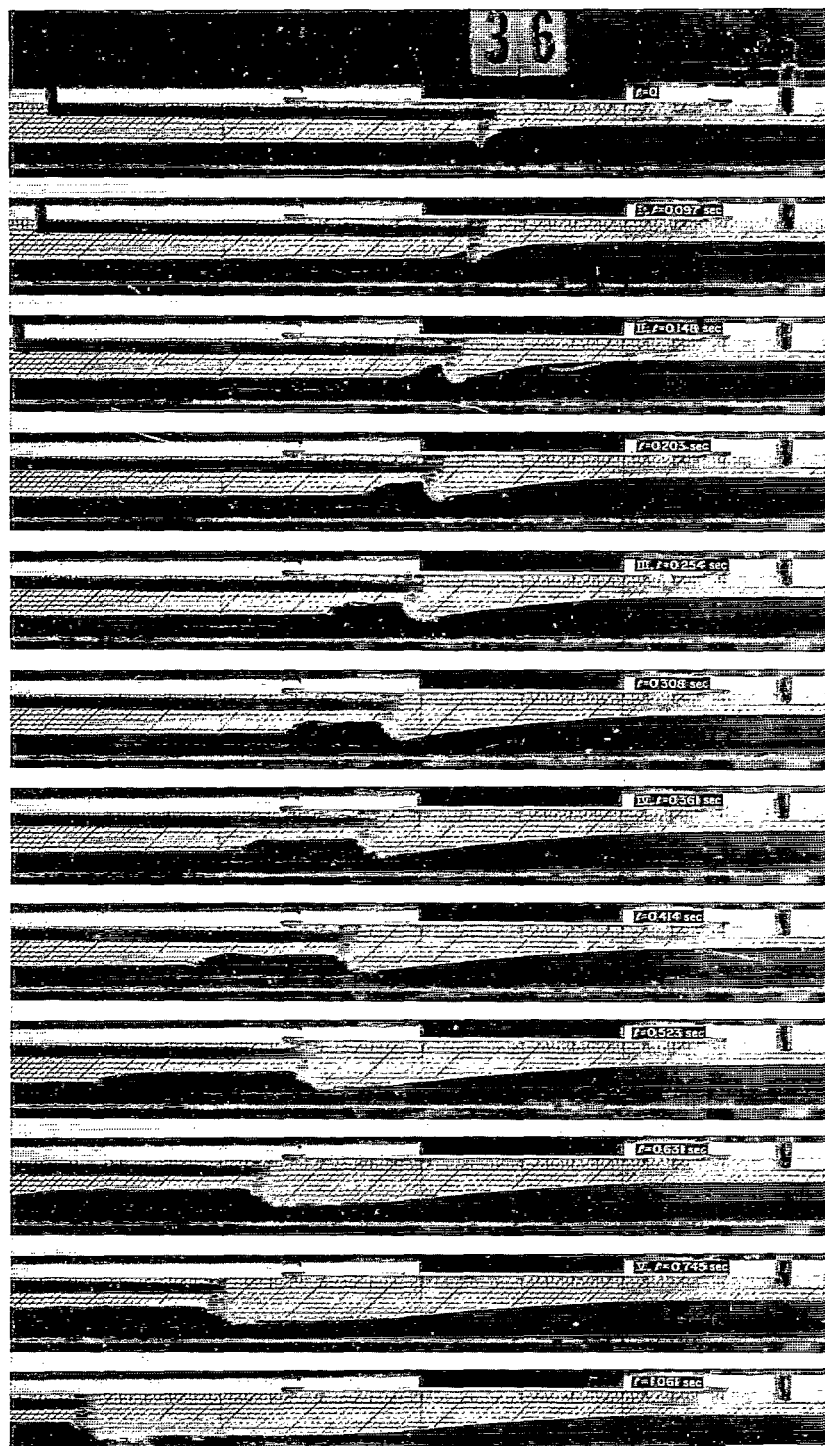
(a) Experimental surface profiles.

Figure 29.- Interaction of a transverse magnetic field with a centered expansion in mercury; copper bottom, $U_p = -0.51$, $h_O = 0.60$ inch, $a_O = 1.26$ ft/sec, $P_{mo} = 1.48$.

85
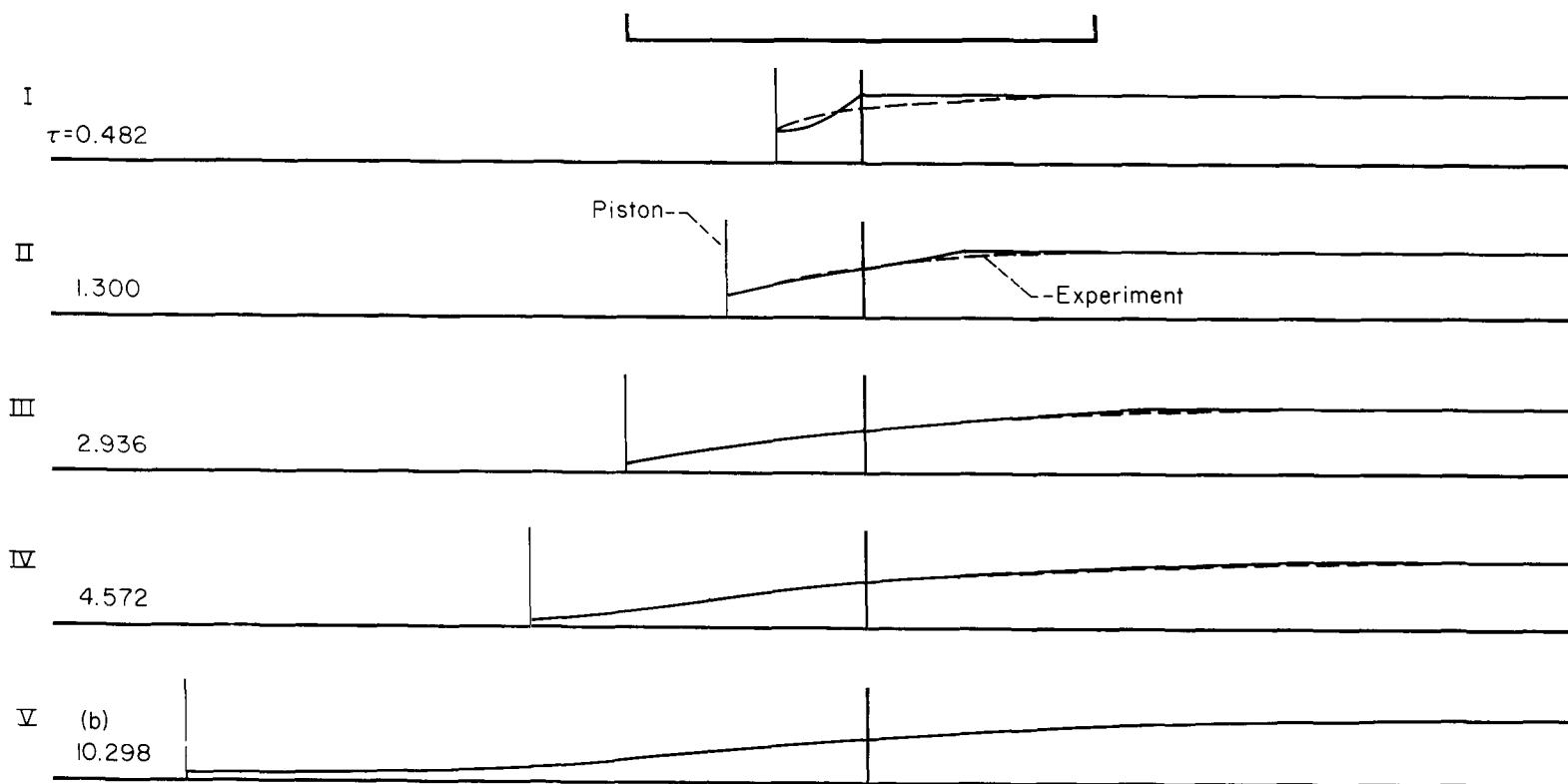
(b) Comparison of theory and experiment; C = 0.88.

Figure 29.- Concluded.
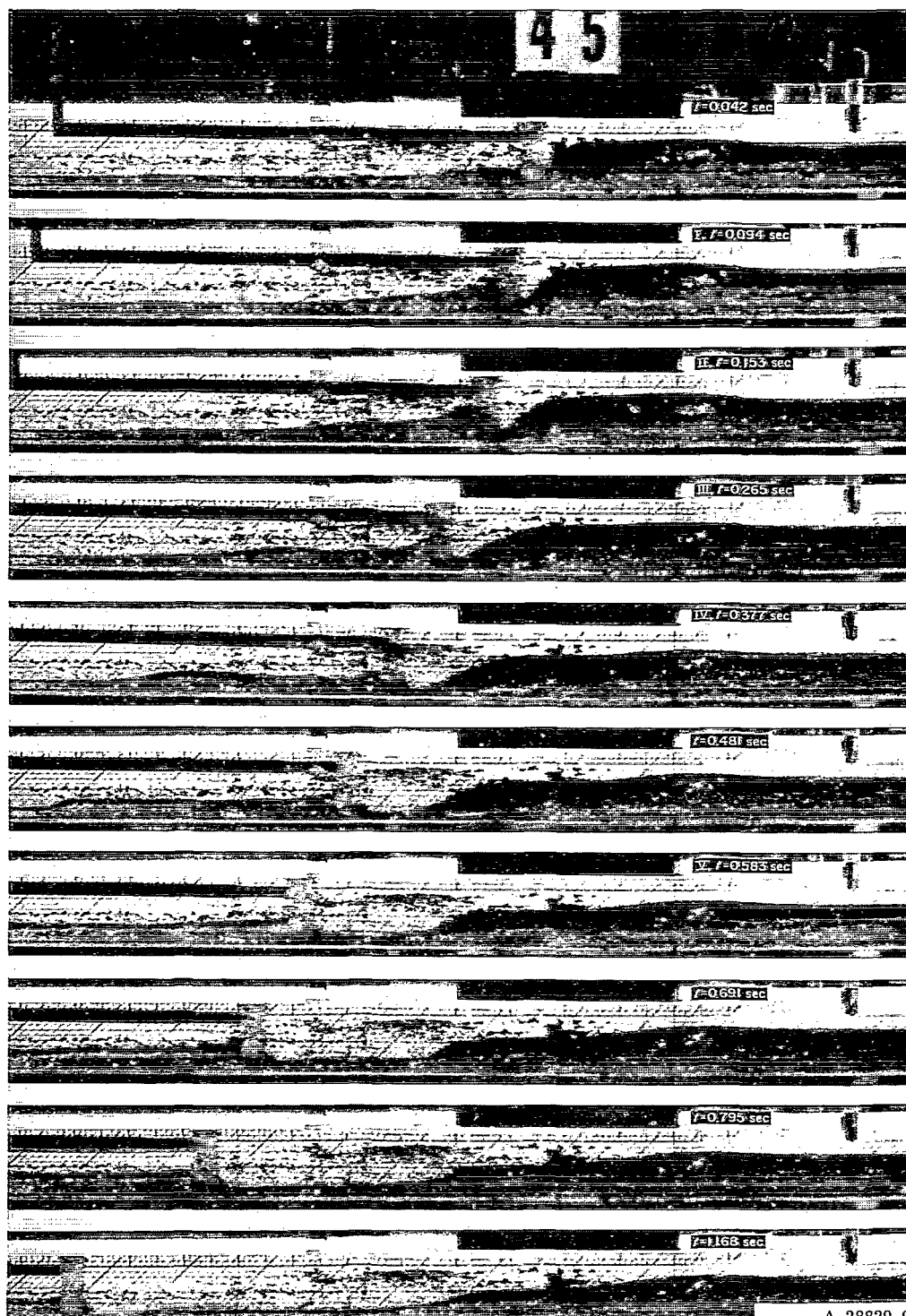
(a) Experimental surface profiles.

Figure 30.- Interaction of a transverse magnetic field with a centered expansion in NaK; insulating walls and bottom, $U_p = -0.43$, $h_O = 0.88$ inch, $a_O = 1.54$ ft/sec, $P_{mO} = 41.7$.

I $\tau = 0.70$

$C = 0.08$
0.19
0.37
Experiment

II 2.76

III 4.82

IV 6.88

V 8.94

(b)

(b) Comparison of theory and experiment.

Figure 30.- Concluded.
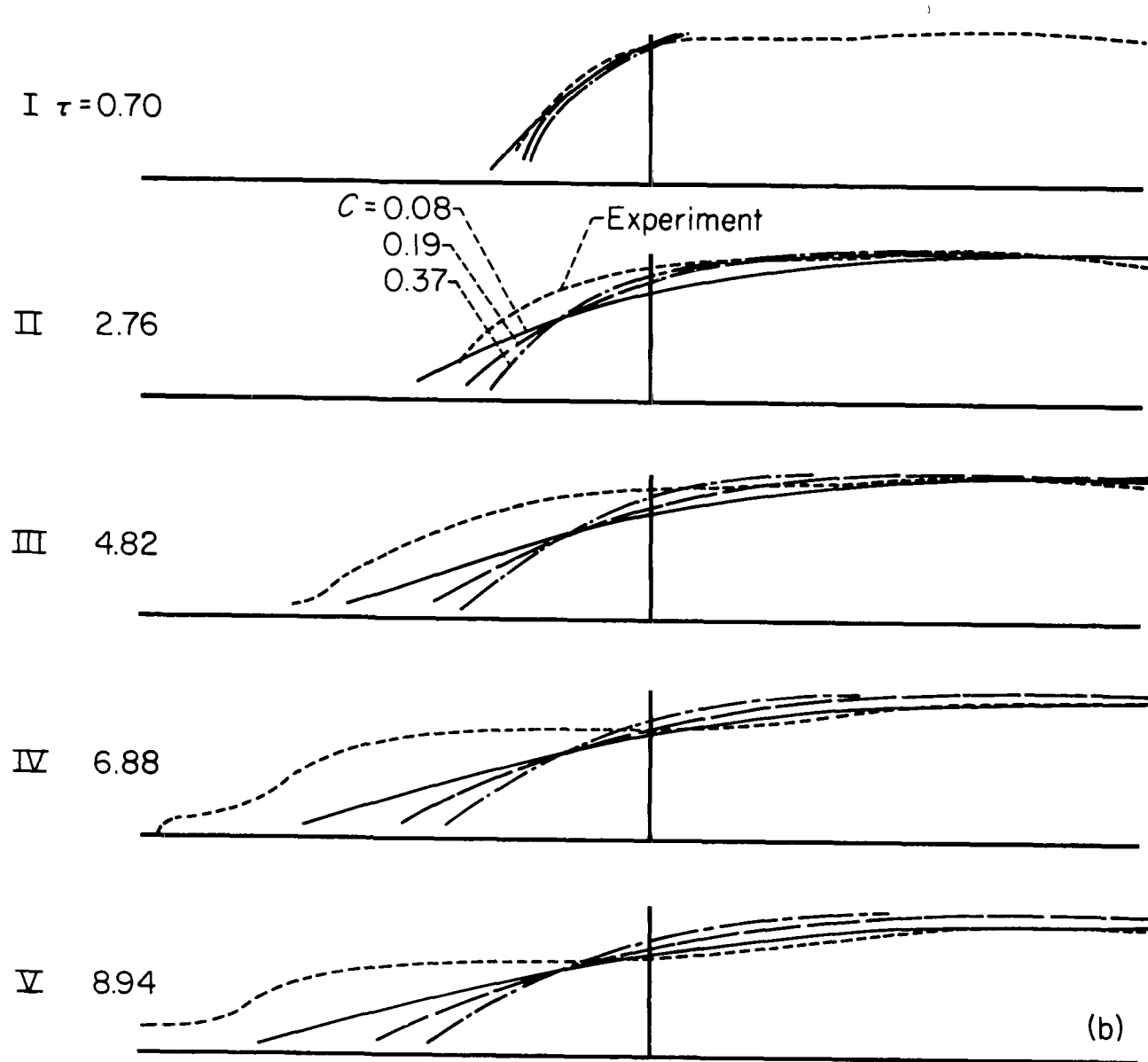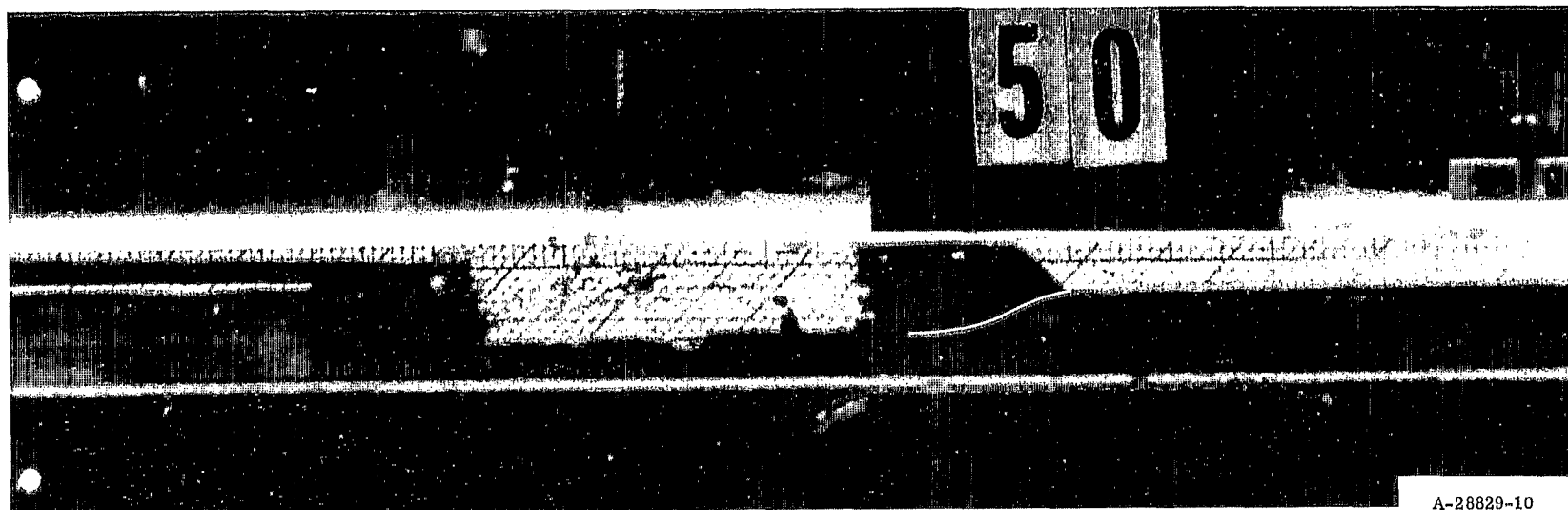
(a) Surface shape about 0.7 sec after piston is removed $(\tau \approx 10)$.

Figure 31.- Interaction of transverse magnetic field with centered expansion in NaK, copper bottom, $U_p = -0.54$, $h_0 = 0.55$ inch, $a_0 = 1.22$ ft/sec, $P_{mo} = 52.8$.

$\tau = 1.49$

3.21

4.93

6.65

10.95

(b)
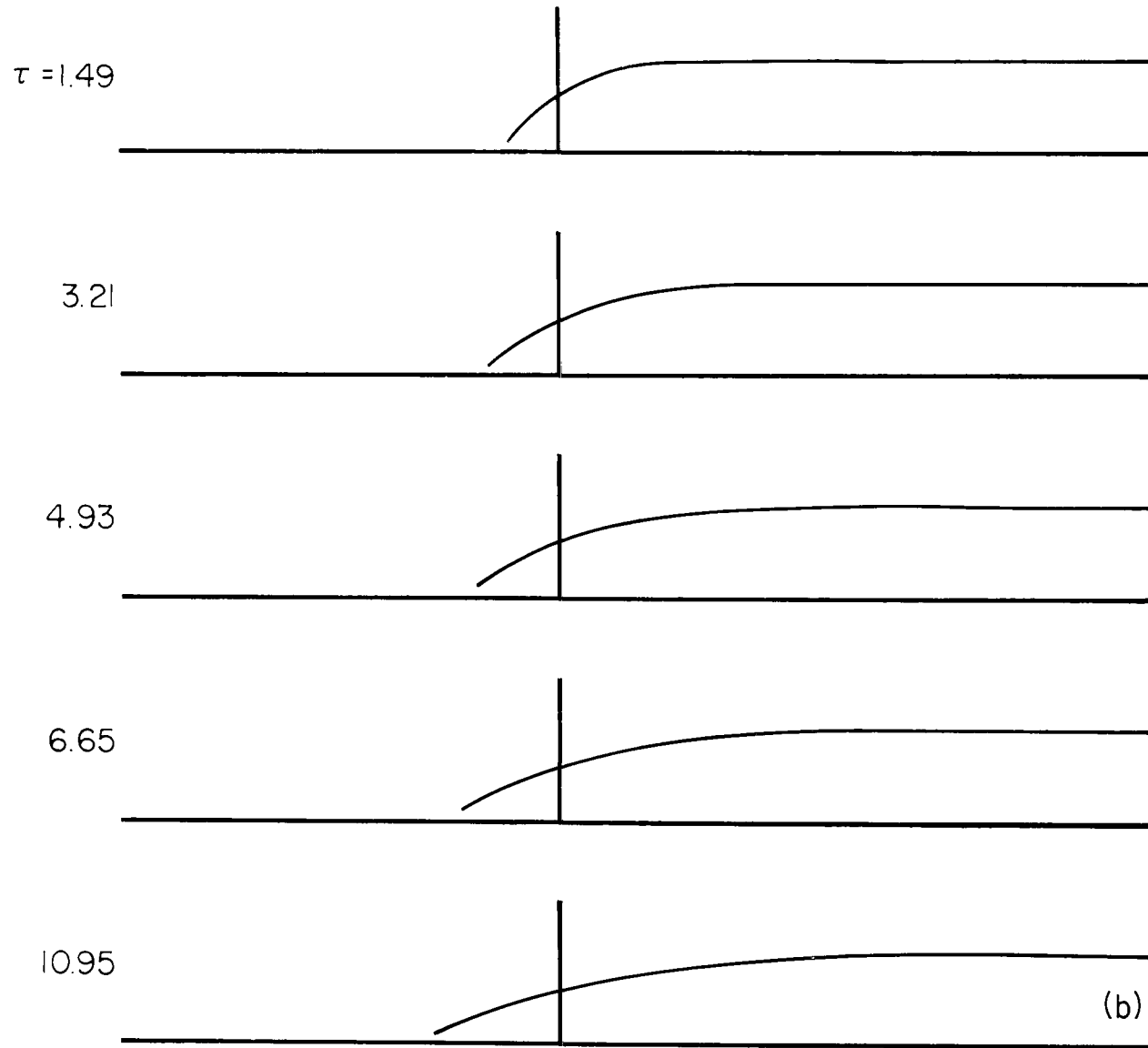
(b) Theoretical shape of surface for experiment of C = 0.44.

Figure 31.- Concluded.
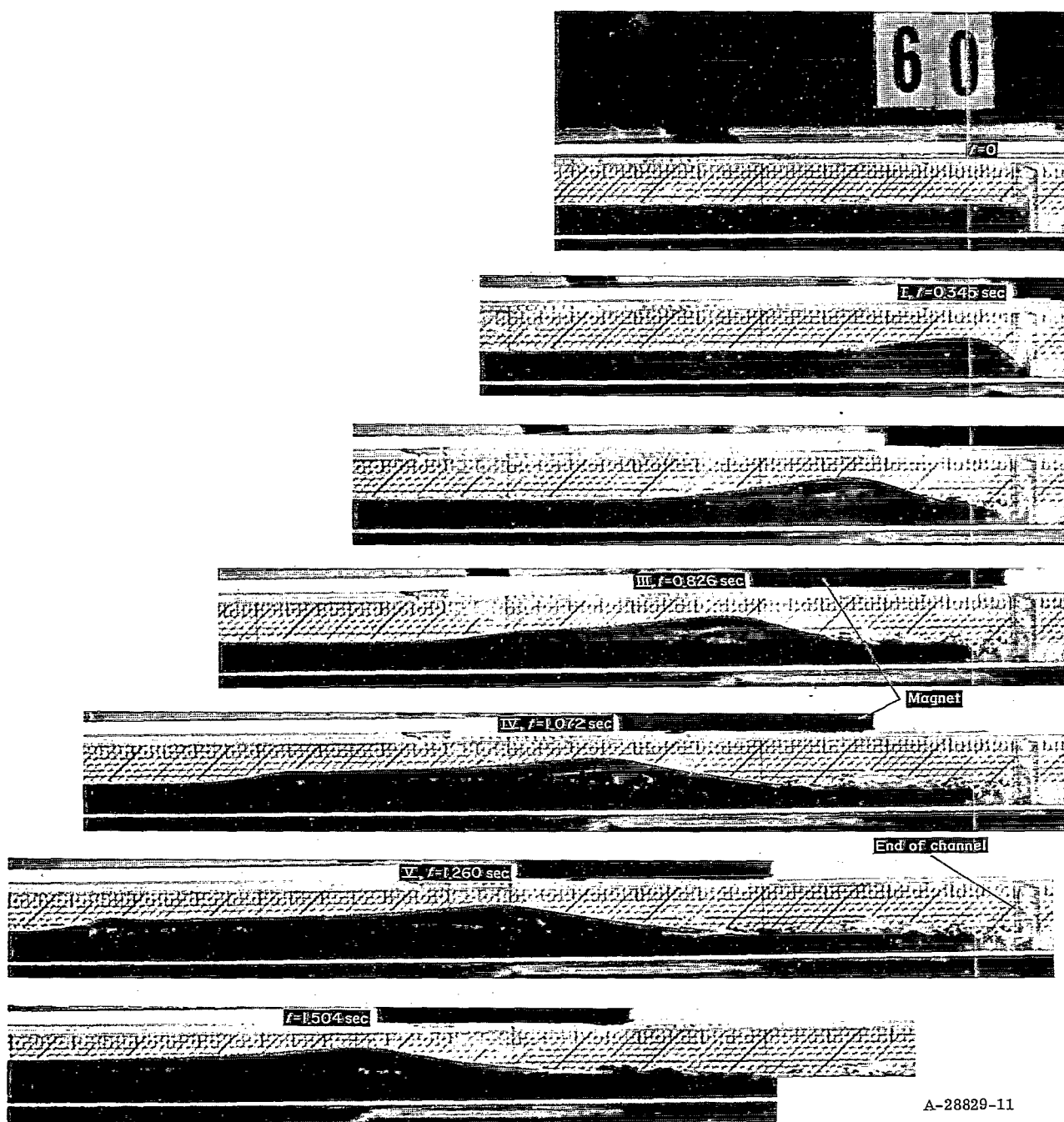
A-28829-11

(a) Experimental profiles of surface shape.

Figure 32.- Disturbance brought about in NaK by magnet moving past channel; insulating walls, U_m = -0.68, h_O = 0.42 inch, a_O = 1.06 ft/sec, P_{mo} = 60.4.

I

$\tau = 4.28$

II

7.40

III

10.52

IV

13.64

Experiment

V

(b)

16.00

NaK oxide on wall
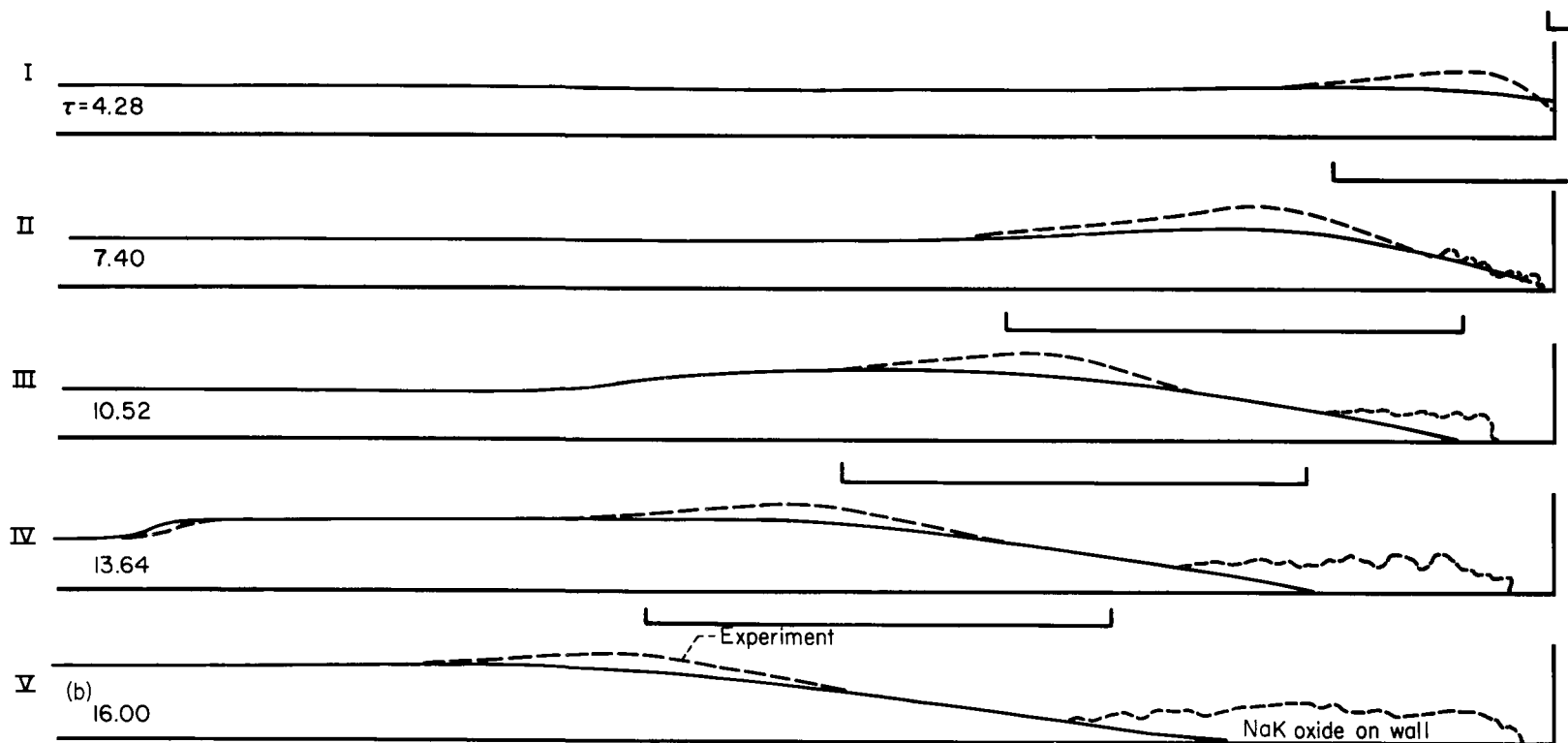
(b) Comparison of theory and experiment; C = 0.026.

Figure 32.- Concluded.
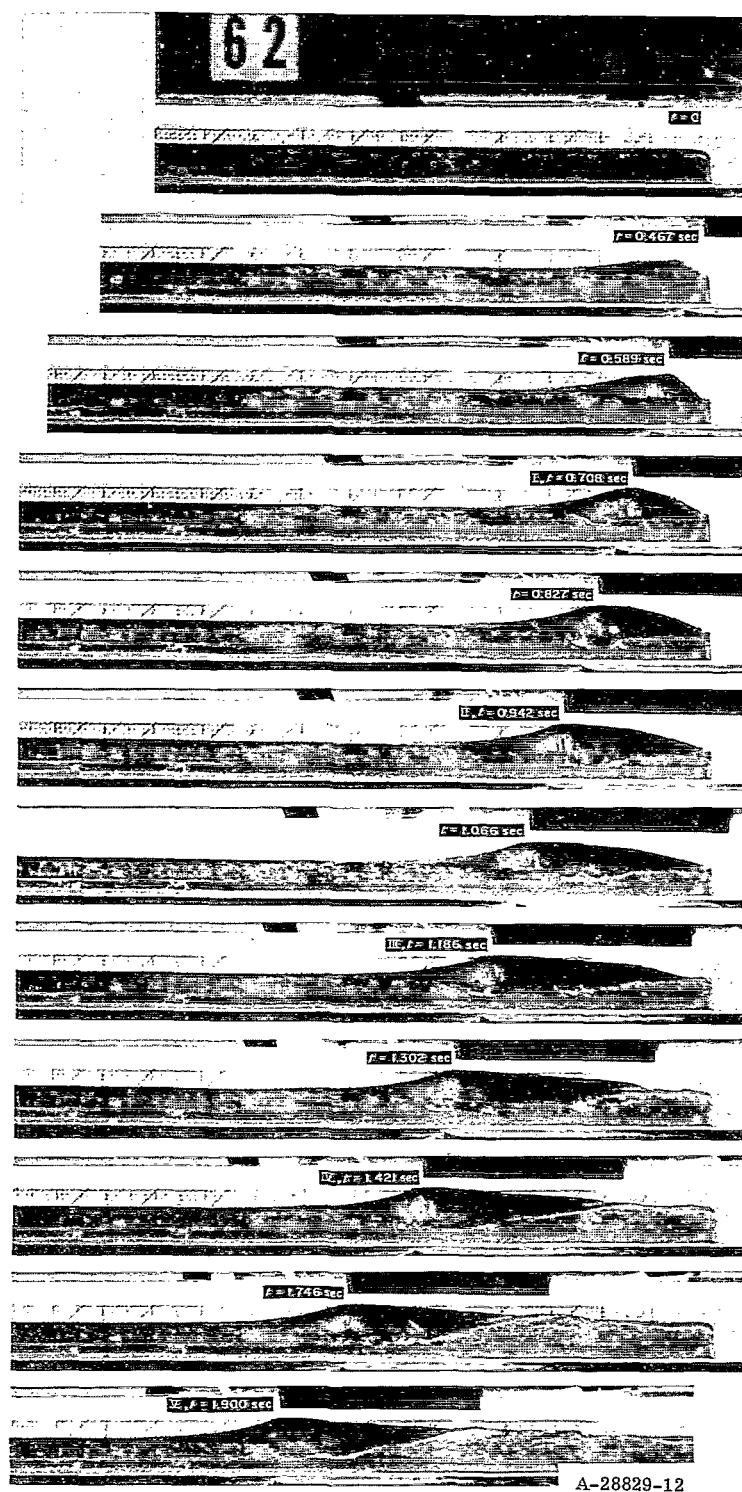
(a) Experimental profile of surface shape.

Figure 33.- Disturbance brought about in NaK by magnet moving past channel; copper bottom, $U_m = -0.51$, $h_o = 0.46$ inch, $a_o = 1.11$ ft/sec, $P_{mo} = 57.8$.

I

$\tau = 9.338$

II

12.571

III

15.754

IV

18.937

(b)

Fluid drawn to center

Fluid thrown outward against side walls

V

25.303
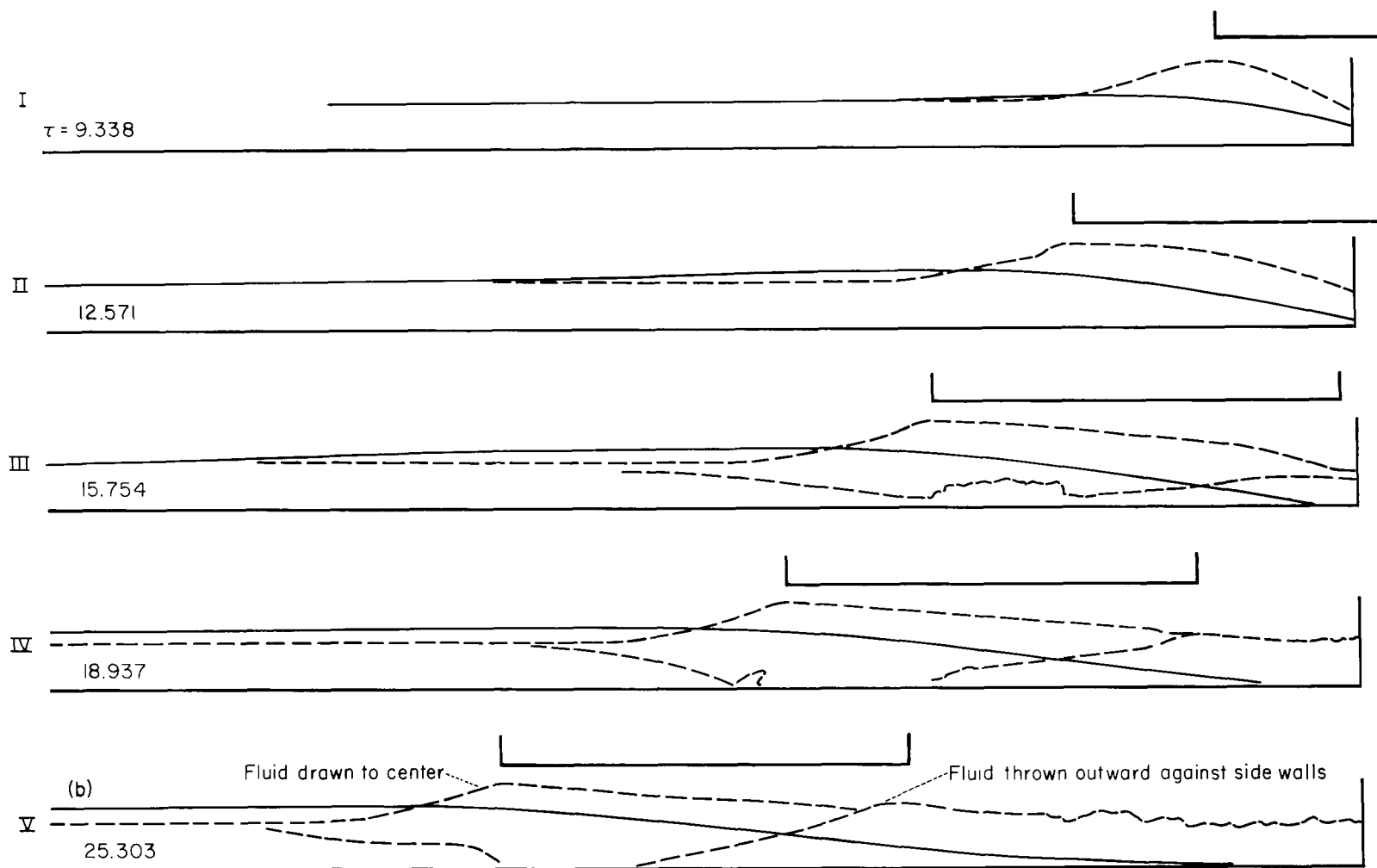
(b) Comparison of theory and experiment; C = 0.026.

Figure 33.- Concluded.

A-28829-14

(a) Insulating walls; $U_m = -0.84$, $h_0 = 0.37$ inch, $a_0 = 1$ ft/sec, $P_{mo} = 1.48$, $C \approx 0.02$.
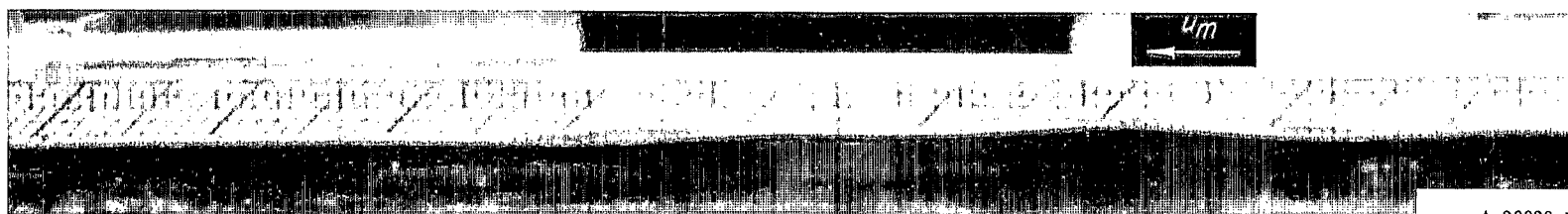
A-28829-15

(b) Copper bottom; $U_m = -1.76$, $h_0 = 0.33$ inch, $a_0 = 0.94$ ft/sec, $P_{mo} = 1.48$.

Figure 34.- Disturbances brought about in mercury by magnet moving past channel.

Figure 35.- Oblique view of surface wave patterns on mercury as magnet moves past channel at various speeds; h_o = 0.38 inch, a_o = 1.01 ft/sec, P_{mo} = 1.48.
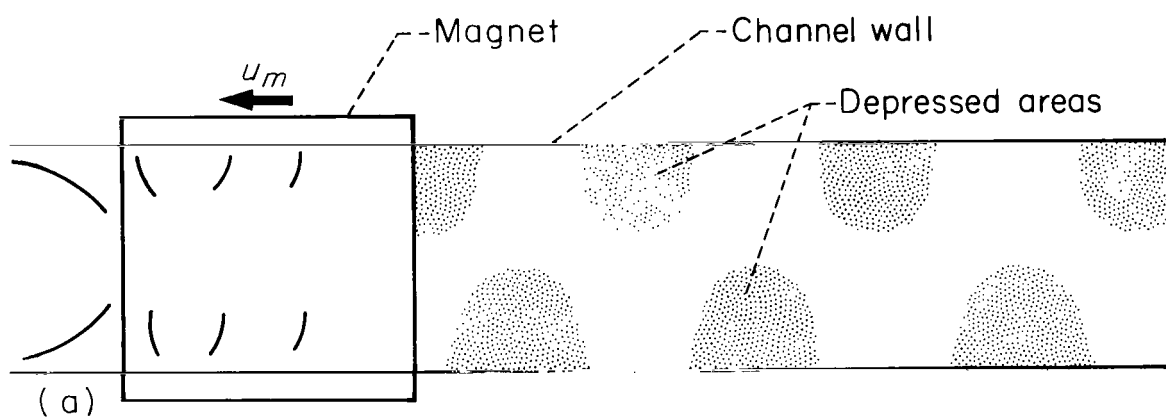
(a) Fr < 1
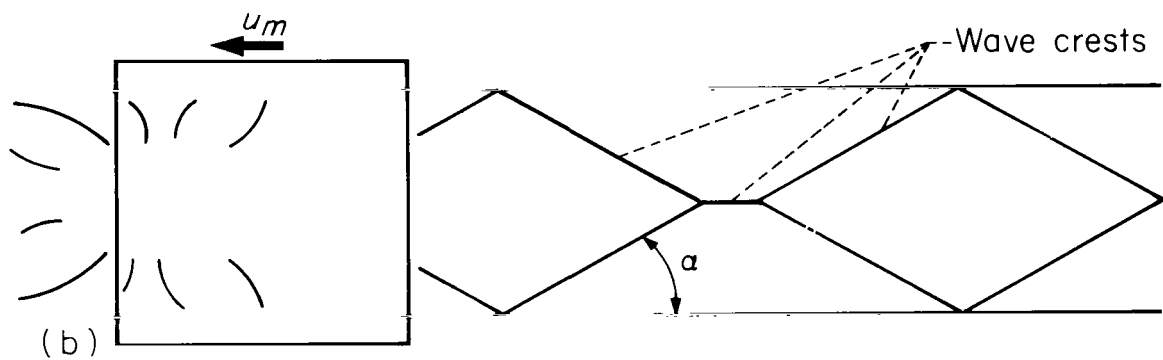
(b) Fr > 1

Figure 36.- Plan view of wave pattern for magnet moving over mercury.
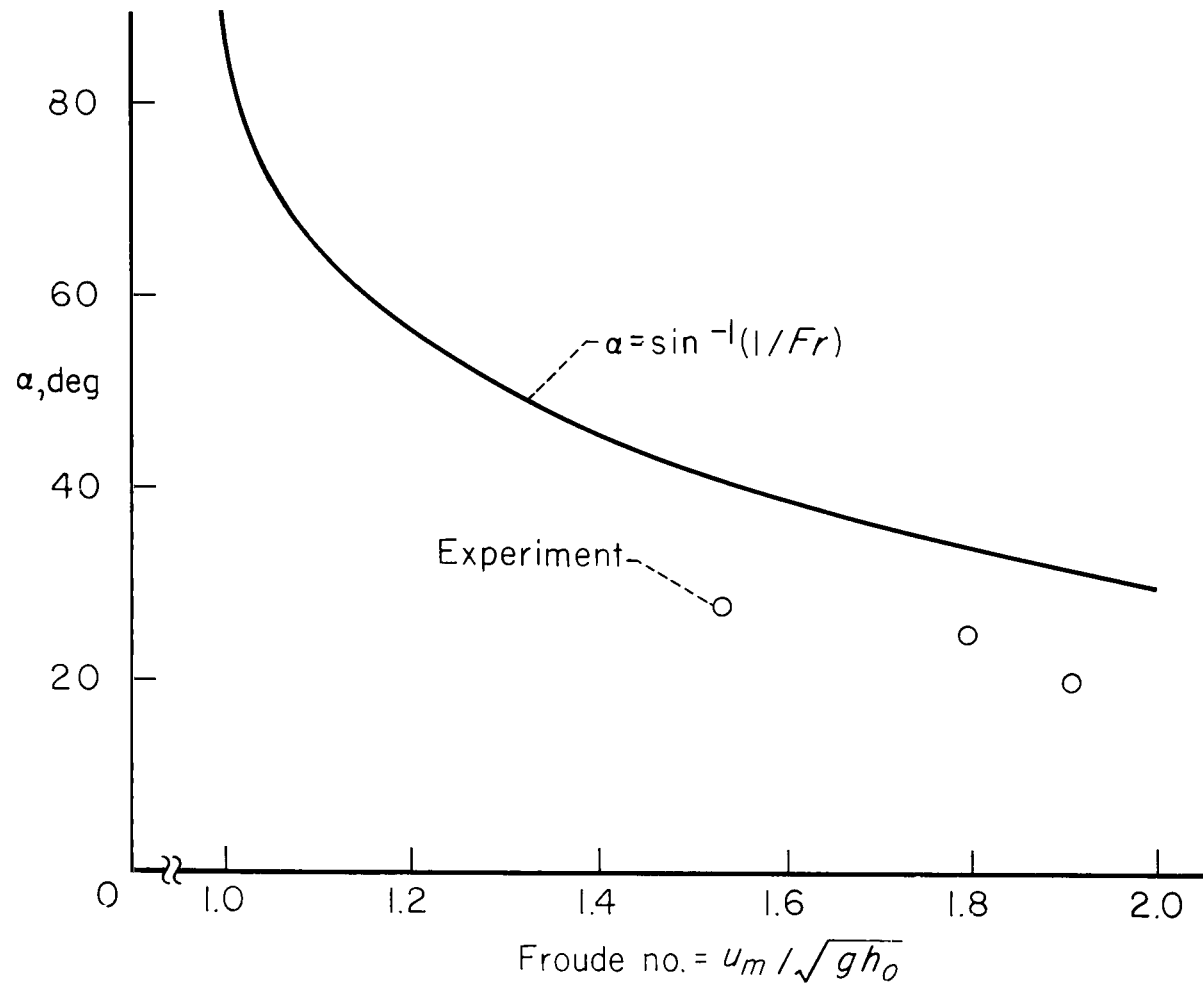
Figure 37.- Variation of wave angle on surface of mercury behind moving magnet as a function of Froude number.
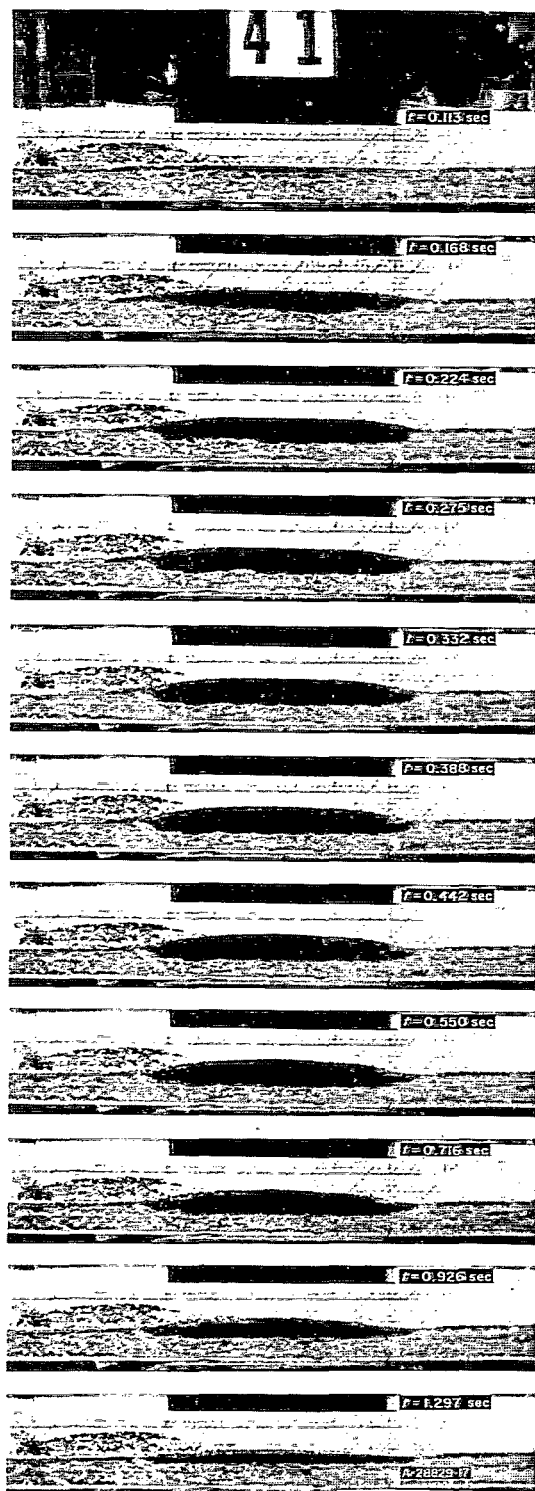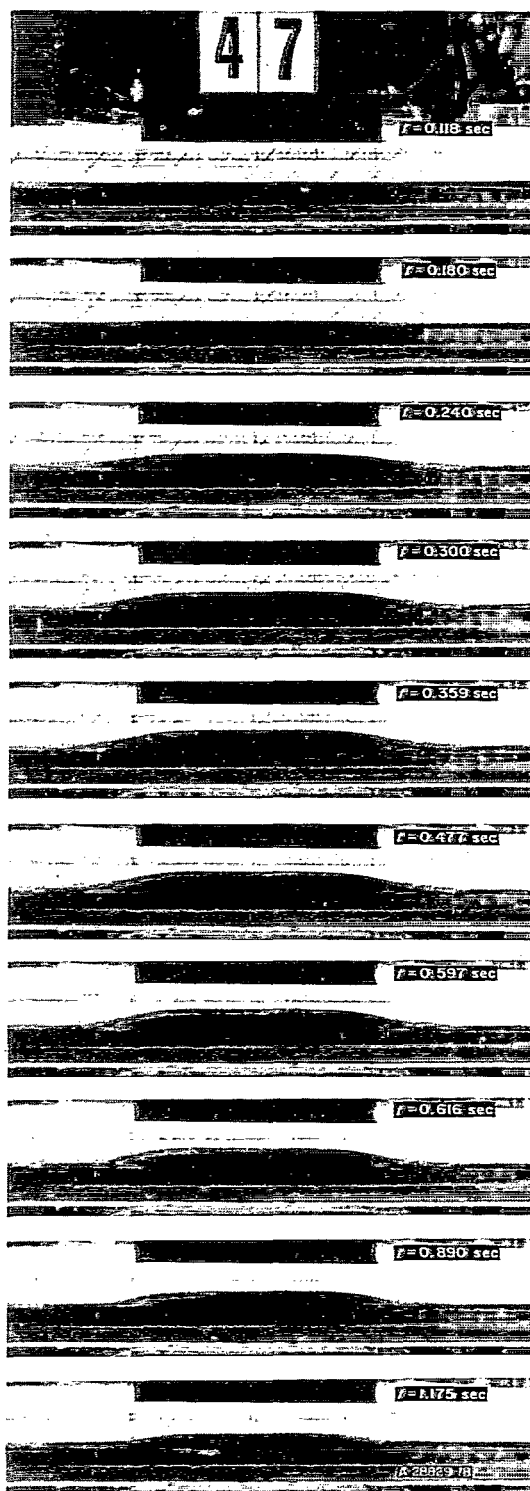
(a)   Insulating walls; $P_{mo} \approx 70$, h_o = 0.49 inch, a_o = 1.15 ft/sec.
(b)   Copper bottom; P_{mo} = 70.8, h_o = 0.42 inch, a_o = 1.06 ft/sec.

Figure 38.- Side view of surface shape of NaK as magnet is energized.
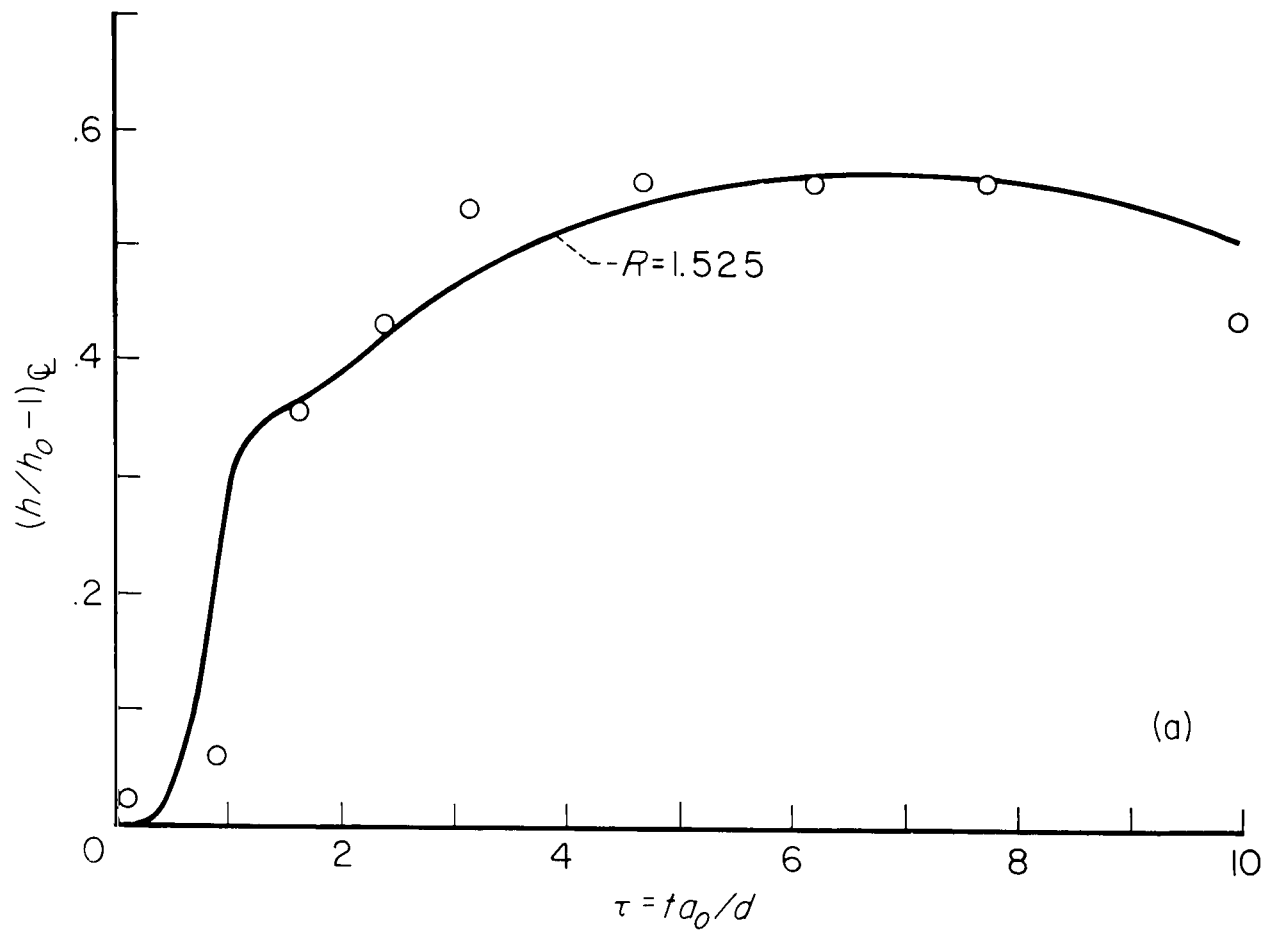
(a) Comparison of theoretical and experimental values for surface height at center of magnet as a function of time; C = 1.

Figure 39.- Two-dimensional theoretical values for data in figure 37(b); P_{mo} = 70.8, h_0 = 0.42 inch, a_0 = 1.06 ft/sec.

(b) Shape of surface at various instants of time.

Figure 39.- Concluded.
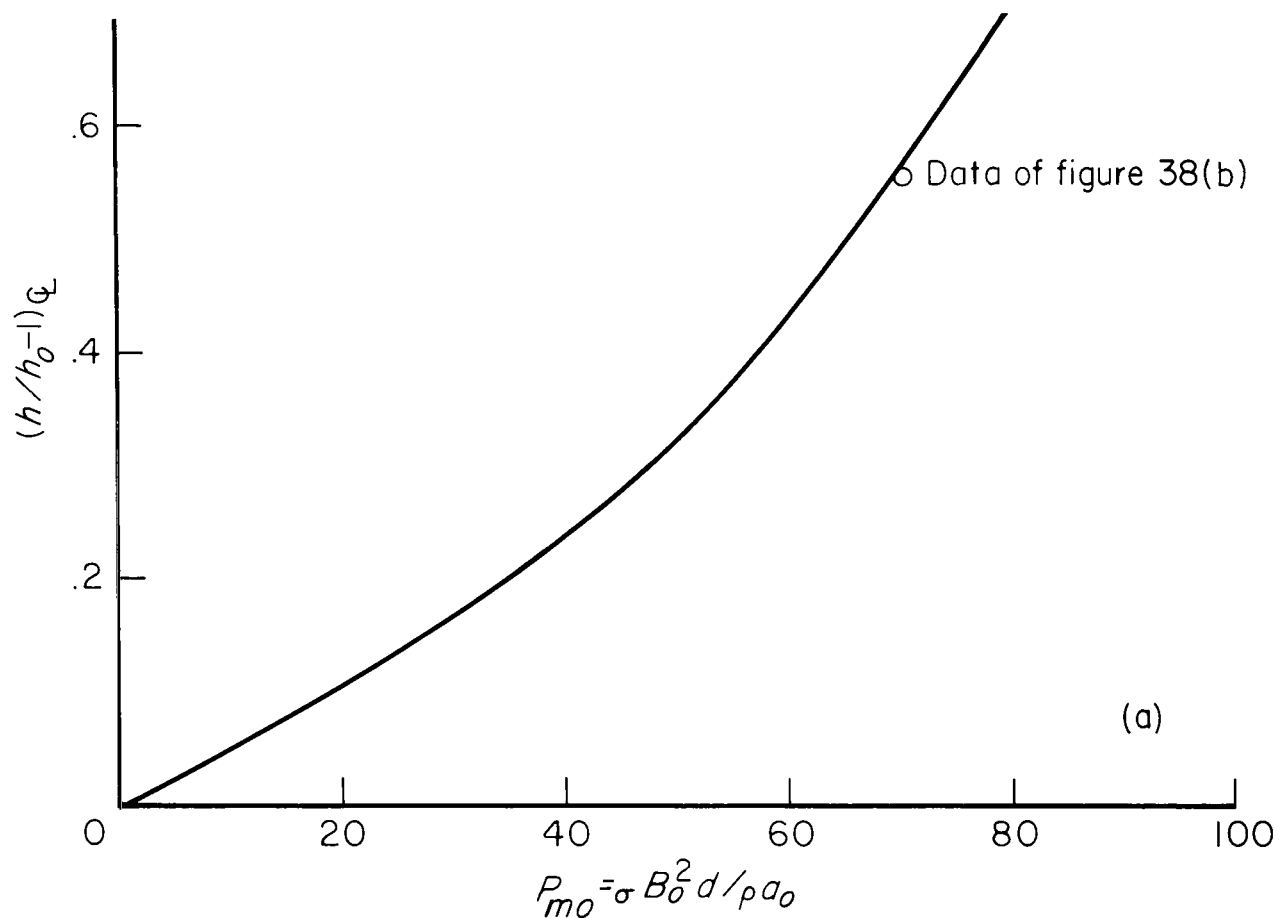
(a) With magnetic parameter, P_{mo}, for $R/L_o = 1.17$ (value for data in fig. 37(b)).

Figure 40.- Variation of maximum two-dimensional surface height.
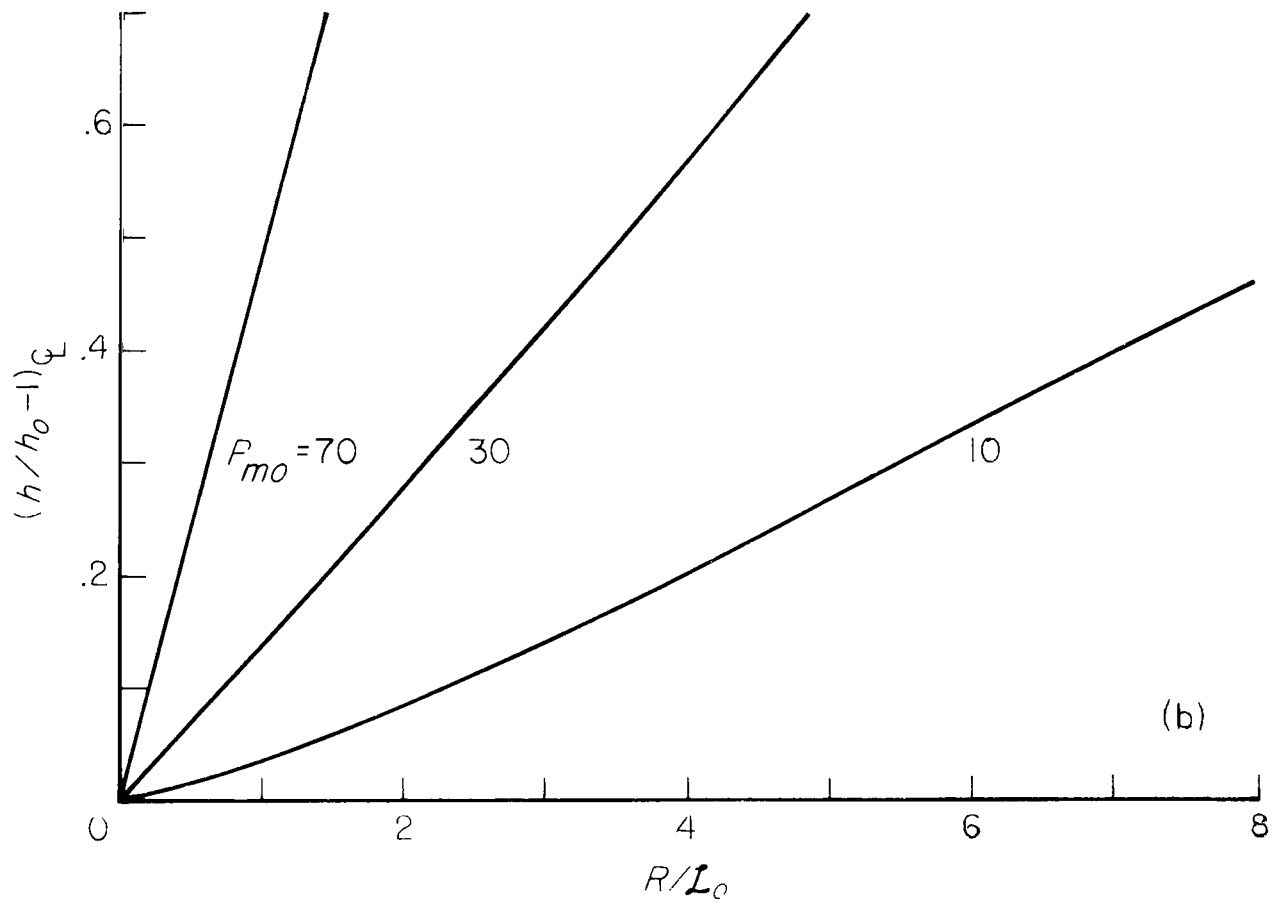
(b) With magnet time constant.

Figure 40.- Concluded.
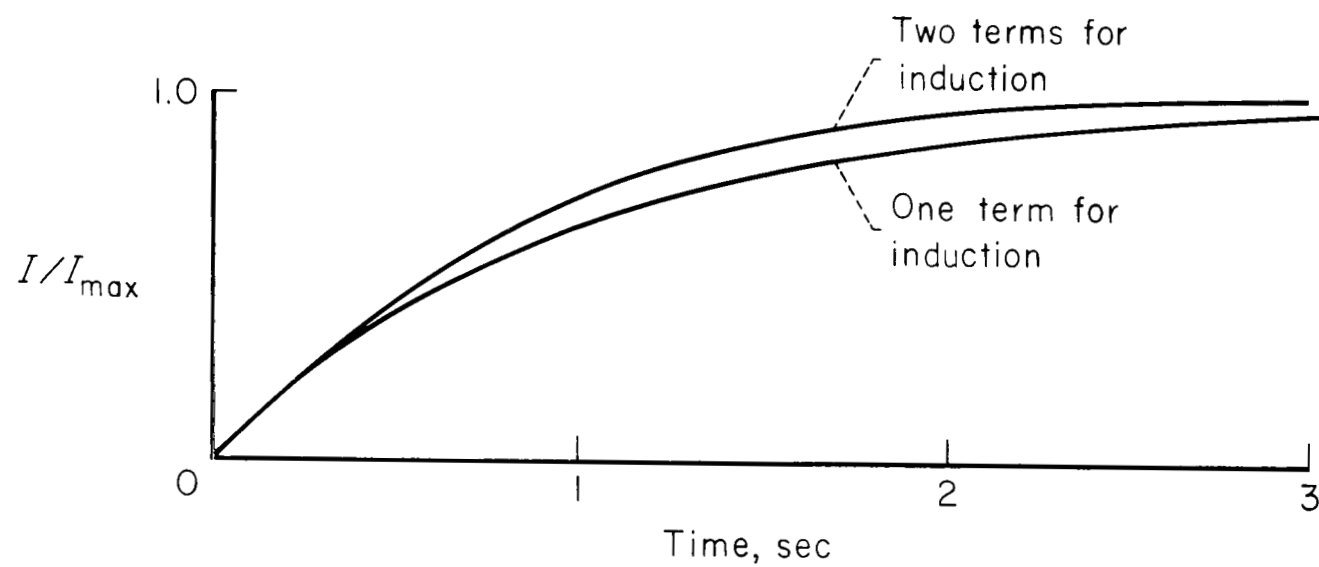
Figure 41.- Theoretical variation of current with time that was assumed for magnet.
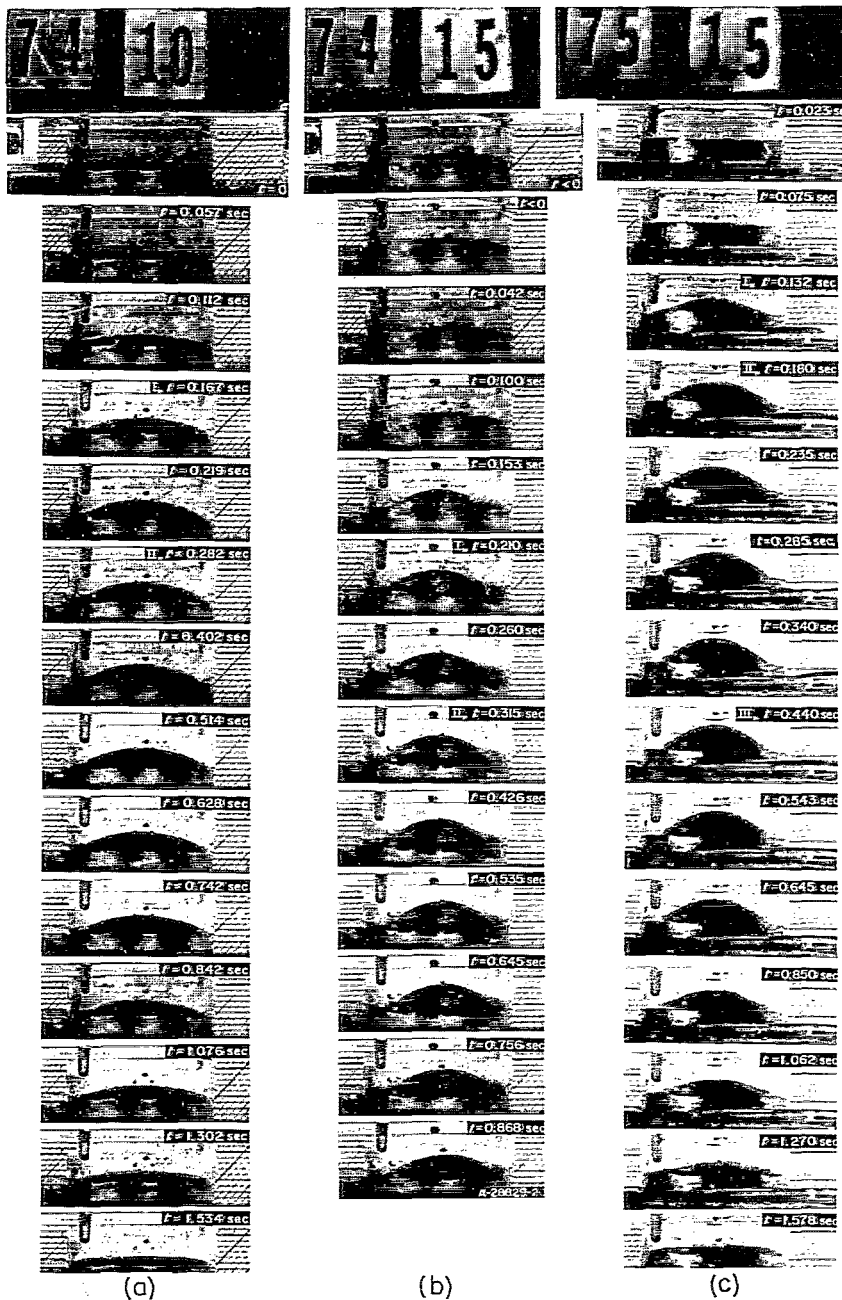
(a) Insulating walls and bottom; $P_{mo} = 60.7$, $h_o = 0.63$ inch,
$a_o = 1.30$ ft/sec.
(b) Insulating walls and bottom; $P_{mo} = 74.4$, $h_o = 0.63$ inch,
$a_o = 1.30$ ft/sec.
(c) Copper bottom; $P_{mo} = 90.2$, $h_o = 0.45$ inch, $a_o = 1.10$ ft/sec.

Figure 42.- Photographic sequences of surface shape of NaK within axially
symmetric container as magnet is energized.
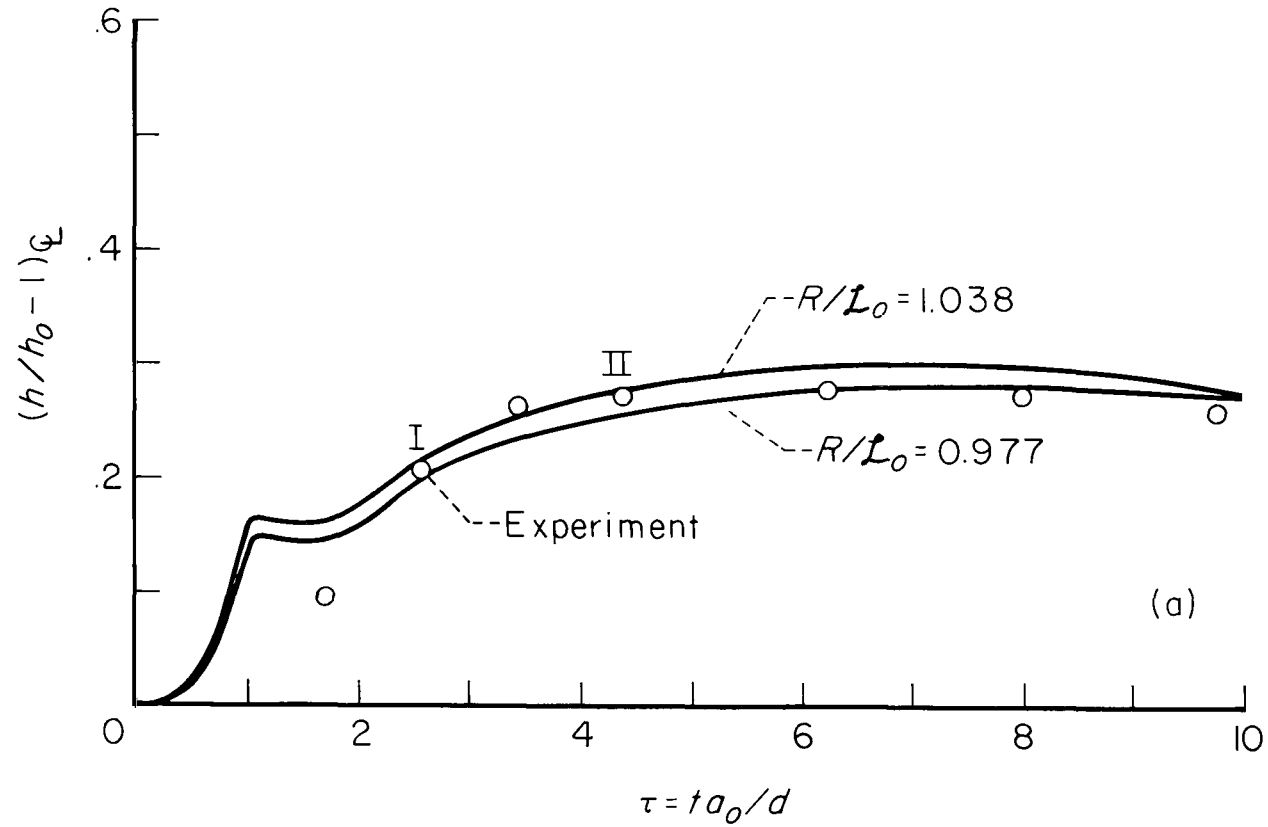
(a) Data in figure 42(a).

Figure 43.- Comparison of axially symmetric theory with experimental data for height of NaK at center of channel.
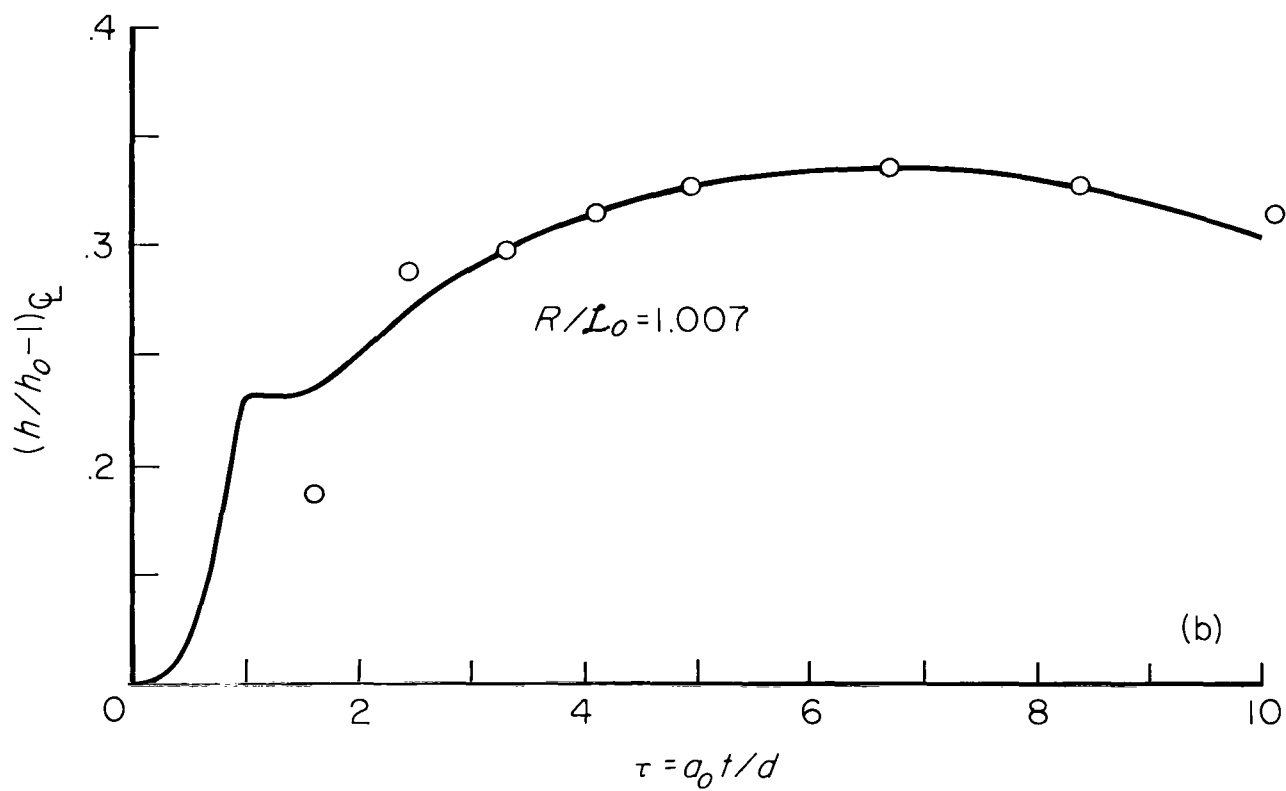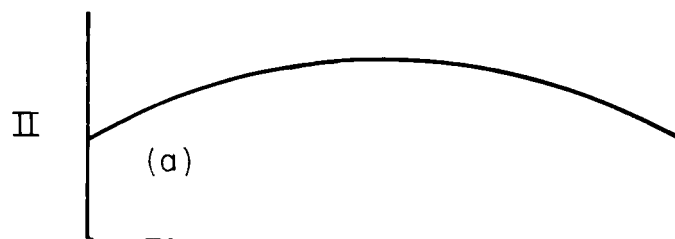
(b) Data in figure 42(b).
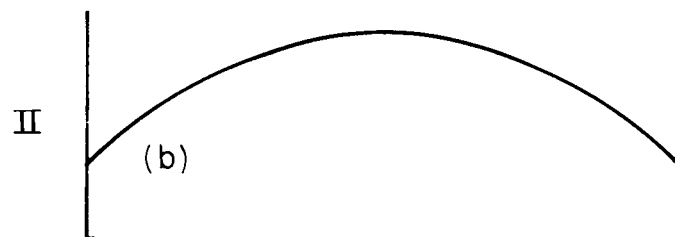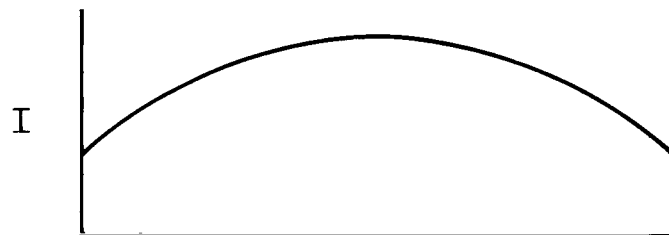
Figure 43.- Continued.
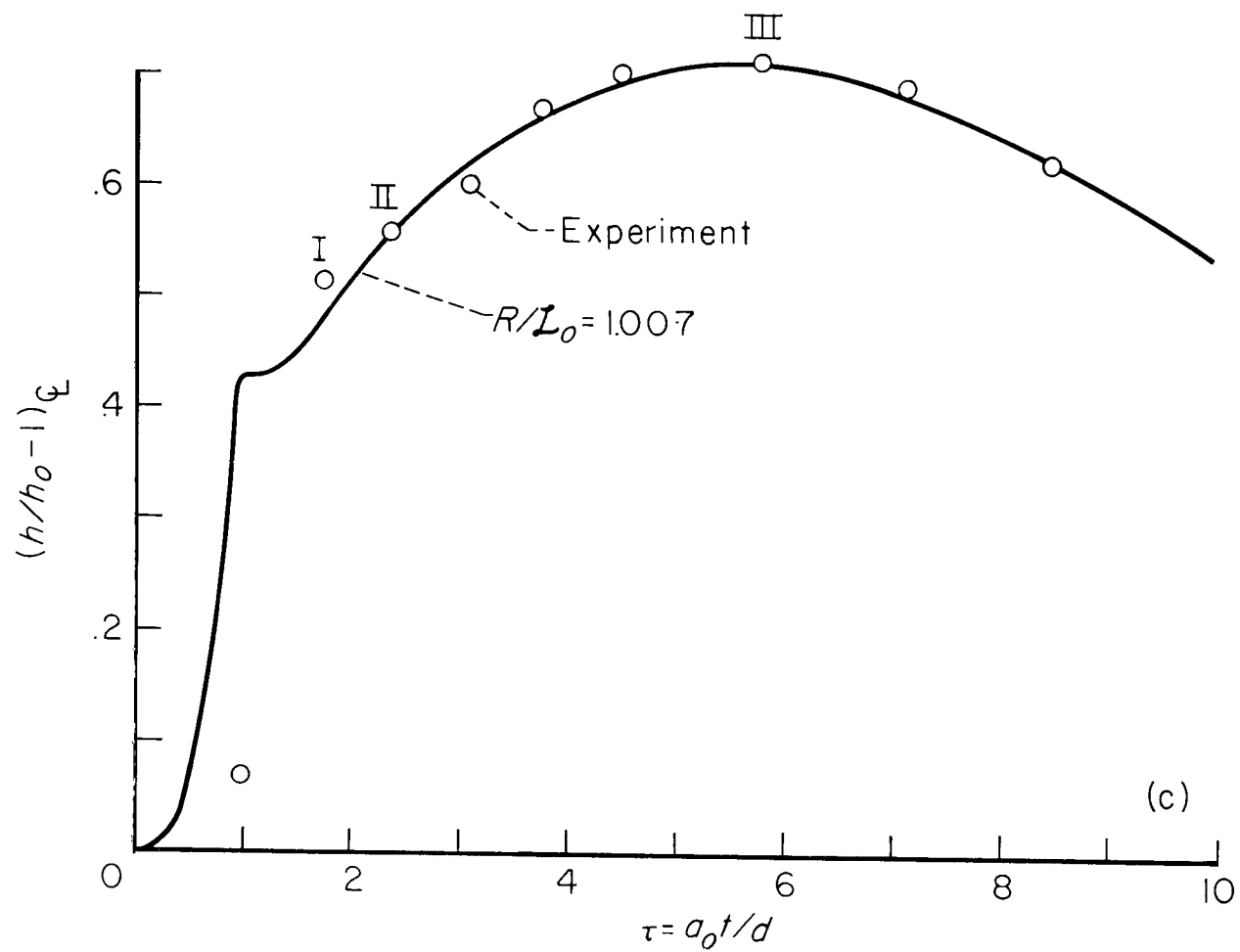
(c) Data in figure 42(c).
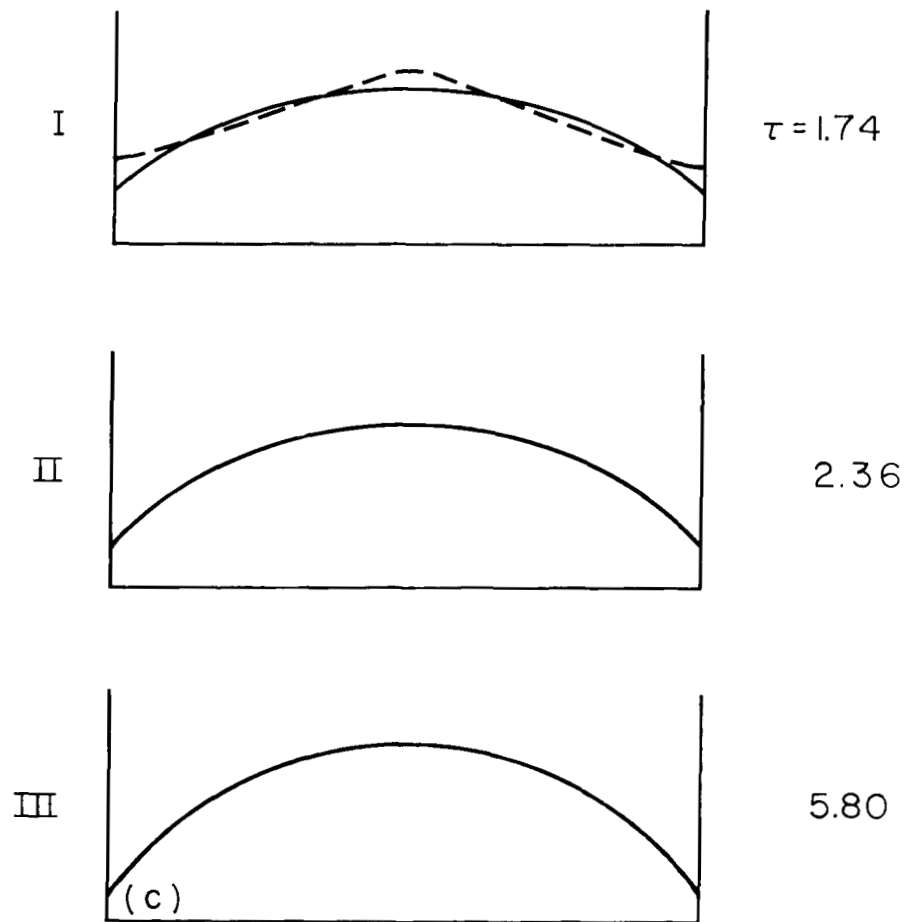
Figure 43.- Concluded.

(a) Data in figure 42(a).

(b) Data in figure 42(b).

Figure 44.- Surface shapes of NaK in axially symmetric container at various
instants of time when magnet is energized.

I $\tau = 1.74$

II   2.36

III   5.80

(c)

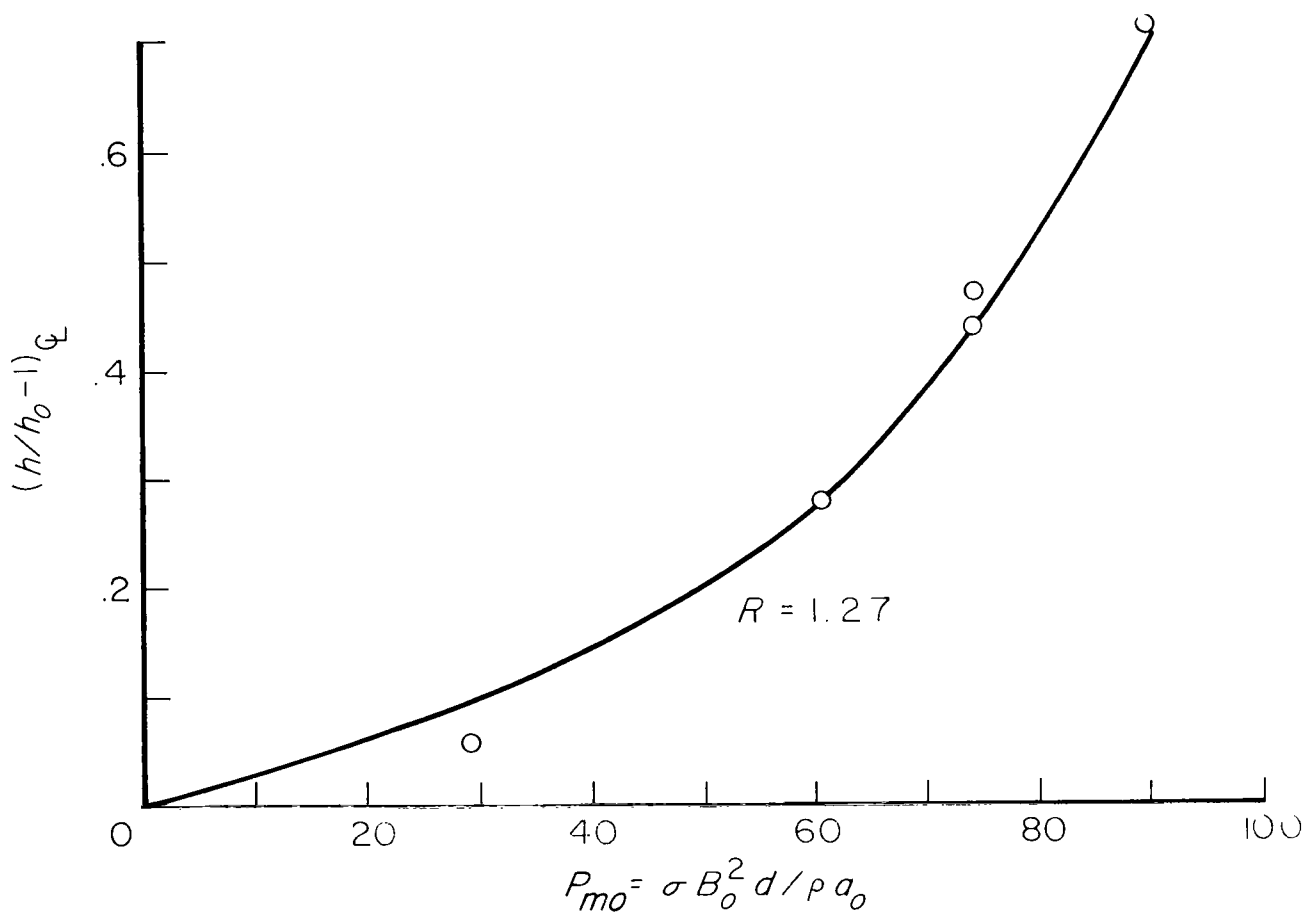(c) Data in figure 42(c).

Figure 44.- Concluded.

Figure 45.- Variation of maximum surface height of NaK in axially symmetric
container as magnet is energized.

"The aeronautical and space activities of the United States shall be conducted so as to contribute . . . to the expansion of human knowledge of phenomena in the atmosphere and space. The Administration shall provide for the widest practicable and appropriate dissemination of information concerning its activities and the results thereof."

—NATIONAL AERONAUTICS AND SPACE ACT OF 1958

NASA SCIENTIFIC AND TECHNICAL PUBLICATIONS

TECHNICAL REPORTS: Scientific and technical information considered important, complete, and a lasting contribution to existing knowledge.

TECHNICAL NOTES: Information less broad in scope but nevertheless of importance as a contribution to existing knowledge.

TECHNICAL MEMORANDUMS: Information receiving limited distribution because of preliminary data, security classification, or other reasons.

CONTRACTOR REPORTS: Technical information generated in connection with a NASA contract or grant and released under NASA auspices.

TECHNICAL TRANSLATIONS: Information published in a foreign language considered to merit NASA distribution in English.

TECHNICAL REPRINTS: Information derived from NASA activities and initially published in the form of journal articles.

SPECIAL PUBLICATIONS: Information derived from or of value to NASA activities but not necessarily reporting the results of individual NASA-programmed scientific efforts. Publications include conference proceedings, monographs, data compilations, handbooks, sourcebooks, and special bibliographies.

Details on the availability of these publications may be obtained from:

SCIENTIFIC AND TECHNICAL INFORMATION DIVISION

NATIONAL AERONAUTICS AND SPACE ADMINISTRATION

Washington, D.C. 20546